Dissertation

submitted to the
Combined Faculties for the Natural Sciences and for Mathematics
of the Ruperto-Carola University of Heidelberg, Germany
for the degree of
Doctor of Natural Sciences

presented by

Diplom-Physicist Elena Puga Antolín
born in: Santa Cruz de Tenerife, España

Oral examination: October 20th 2004

Early Stages of Massive Star Formation at High Spatial Resolution

No tengas miedo, no te sientas solo;
aquéllo que guía a las estrellas, te guía a tí también.

Anónimo

To Jacobo and my family

Zusammenfassung

Die Entstehung massereicher Sterne findet unter für die Beobachtung ungnstigen Bedingungen statt. In etwas fortgeschrittenem Alter erzeugen die bereits entstandenen Sterne ein ionisiertes Gebiet und diszipieren die umgebende Molekülwolke. Diese Phase, in der ultrakompakte HII-Gebiete (UKHG) ausgebildet werden, ist somit eine der frhsten um massereiche Sterne zu beobachten. Diese Arbeit untersucht die ionisierenden Sterne sowie die Kinematik von ultrakompakten HII-Gebieten mit hoher spektraler und räumlicher Auflösung. NIR-Polarisationskarten der diese Objekte generell umgebenden Reflektionsnebel werden genutzt, um sowohl die Existenz tief eingebetteter Begleiter auszuschließen (S106), als auch um die Multiplizität der Hauptbeleuchtungsquellen (welche auch Kandidaten für die Hauptionisationsquellen sind) in G77.96-0.01 zu identifizieren. Dieses letzgenannte Ergebnis kann auch die Beziehung zwischen einigen UKHG und deren ausgedehnten Halos erklären. Die umfassende Analyse eines komplexen UKHG (G61.48+0.09) zeigt das Problem der Vollstndigkeit der im NIR identifizierten enthaltenen Sterne. Dank der polarimetrischen K-Band-Karte konnte das Modell interner Ionisation für die kleinere der beiden Komponenten vorhergesagt werden. Diese Vorhersage bestätigte sich durch die Entdeckung eines stellaren Objektes in einer $3.5\,\mu$m-Aufnahme. Die spektrale Energieverteilung und das Vorhandensein von Brγ-Emission in den stellaren Spektren deutet auf die Existenz eines Überriesen als Teil der Population dieses UKHGs hin. Die Bestätigung des Vorhandenseins entwickelter Sterne in derartigen Objekten ist ein Beweis, da die Lebensdauern der UKHGs länger sind als bisher angenommen.

Letztendlich zeigt die Studie der kinematischen Struktur von G5.89-0.39, des Paradebeispiels für ein schalenförmiges UKHG und die Quelle der massereichsten Ausströmung in der Galaxis, daß die stoßangeregte Emission molekularen Wasserstoffs mit einer Nord-Süd-Orientierung der Ausströmung vereinbar ist. Dagegen zeigt das ionisierte Material anscheinend eine sekundäre Ausströmung und damit möglicherweise eine zweite stellare Quelle in G5.89-0.39. Das sehr kleine dynamische Alter, welches für dieses Objekt errechnet wurde ($< 10^3\,$a) bestätigt, daß sich auch die die Ausströmung antreibende(n) Quelle(n) in einem sehr frühen Entwicklungsstadium befinden müssen.

Abstract

Massive star formation takes place under harsh observational conditions; as time passes, the already formed stars produce an ionised region and dissipate the surrounding molecular cloud, becoming accessible in the NIR. For this reason one of the earliest phases to observationally study massive stars is the UCHII-region phase. This thesis investigates the ionising stars and kinematics of UCHII regions at high spatial and spectral resolution. NIR-polarimetric maps of the reflection nebula that are generally found around these objects are used to rule out the presence of deeply embedded companions of a Young Stellar Object (S106) and to identify multiplicity in the main illuminating sources (also candidates to be the ionising sources) inside G77.96-0.01. This last result could also explain the relationship between some UCHII and their detected extended halos. An extensive analysis of a complex UCHII (G61.48+0.09) shows the problem of completeness of the detected stellar content in the NIR, and thanks to a K-band polarimetric map, the internal ionisation model for the smaller component is predicted and the corresponding stellar counterpart is detected at $3.5\,\mu$m. The spectral energy distribution and the presence of Brγ emission in the stellar spectra translates into the possible presence of a supergiant as part of the population inside this UCHII. The confirmation of the existence of evolved stars in these objects is an evidence of longer lifetimes than expected by the simple expansion of the Strömgren sphere. Finally the study of the kinematical structure of G5.89-0.39, the paradigm of shell-type UCHII and most massive outflow of the Galaxy, reveals that the confirmed shocked molecular hydrogen emission is compatible with a north-south orientation of the outflow, whereas the ionised material seems to trace a secondary outflow structure and therefore a possible secondary star inside G5.89-0.39. The short dynamical age derived for this object ($< 10^3\,$yr) confirms that the source/sources driving this outflow must also be in an early evolutionary stage.

Contents

Chapter 1

Introduction to Massive Star Formation

1.1 Massive Stars in the Context of Star Formation

Massive stars (M$>$10 M$\odot$) have a very strong impact in the Universe for several reasons. They are the principal sources of UV radiation in the galaxies, generating large Hɪɪ regions. They inject momentum and mechanical energy into the interstellar medium through stellar winds, massive outflows and supernovae explosions. Massive stars also heat and disrupt the molecular cloud where they are born, and enrich the interstellar medium with heavy elements when exploding as supernovae.

Although the formation mechanism proposed for low-mass stars (Shu et al., 1987, 1993), has been proven to reproduce the observations (Lada, 1991), this scheme does not seem to be scaled-up for massive stars. The Kelvin-Helmholz timescale for massive stars ($\leq 10^4$ yr for an O star) is significantly shorter than the evolutionary timescales, namely they start burning hydrogen and reach the main sequence before they stop accreting material from their protostellar envelope. For this same reason, they are difficult to observe, since they spend most of their life deeply buried inside the molecular cloud ($A_V > 10$ magnitudes). They are statistically less frequent than the low-mass stars, resulting in fewer examples of high-mass stars in an early evolutionary stage within a given volume. The resulting greater distance makes it difficult to isolate individual events of massive star formation.

The standard model of star formation through accretion presents also difficulties since stars as massive as 100 M$_\odot$ seem to exist (Kudritzki et al., 1992), but the radiation pressure from the rapidly evolving stellar core should stop accretion before these masses can be built (Wolfire and Cassinelli, 1987). Detection and frequency of discs and or bipolar molecular outflows around massive stars could help to establish a parallelism with the paradigm of low-mass star formation. The so far competing mechanism of coalescence has been proven to only work in very dense stellar environments.

Massive star formation starts with the contraction and fragmentation of giant molecular clouds into clumps. Dense cores are substructures of these clumps (Blitz, 1993), but the relationship between the mass spectrum of the cores and the initial mass function (IMF) of the massive stars is still unknown. The question of what is the *initial unit* of formation of a massive star remains not answered. Larson (1982) addressed that the mass of the most massive stars is correlated with the mass of the associated molecular cloud. The prestellar core phase is
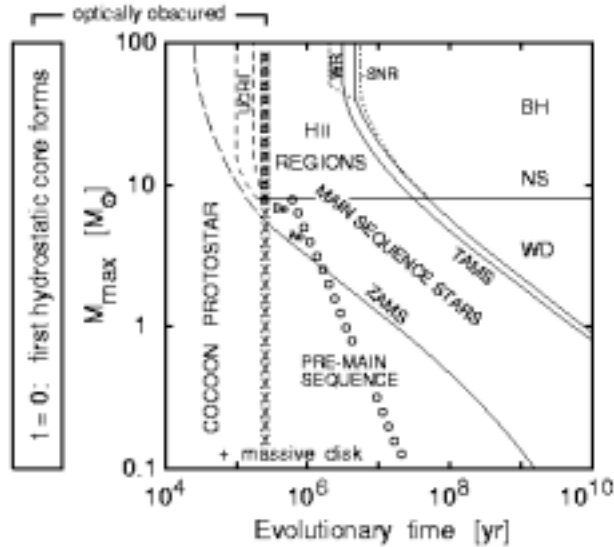
Figure 1.1: Sketch of the relevant stellar timescales by Yorke (2003). Circles represent the dissipation of gaseous discs according to the author, crosses represent the end of the accretion phase. ZAMS and TAMS indicate the beginning and the end of the hydrogen burning phase, respectively. The rest of the acronyms refer to Ae and Be stars, white dwarfs (WD), neutron stars (NS), black holes (BH), supernovae remnants (SR) and Wolf-Rayet stars (WR).

thought to consist of such cores, undergoing a quasistatic gravitational contraction, being one of the most difficult evolutionary stages to identify observationally. This period is followed by the Hot Core phase (also called the Precursors to UCHII region). This very general term is normally applied to the phase in which the protostar, once it is formed, goes through a period of rapid accretion (assuming an accretion scenario for massive stars). Because of the absorption by infalling matter, and despite the protostar emits a large amount of UV photons, no HII region is detectable. By the time the central protostar has accreted approximately $10\,M_\odot$ it has already evolved into a core hydrogen burning phase. This resultant zero-age main sequence star continues to accrete material, photoevaporates the circumstellar disc and ionises the surrounding material, creating an HII region around the star (Yorke, 2003) (see Fig. 1.1). The objects, in which the final destruction of the disc and ionisation of the environment is taking place, which typically takes $\leq 10^5$ yr, are known as UCHIIs.

Massive stars seem to form exclusively in clustered mode (Evans, 1999). Examples of this affirmation are the studies conducted in W3, Mon R2, NGC 2024 and the nearest region of massive star formation: Orion-Trapezium. This gregarious nature implies an inherent observational difficulty to isolate single objects, making high resolution techniques mandatory.

1.2   The Ultra-compact HII Region-Phase

O and B stars emit the bulk of their radiation at wavelengths shorter than the Lyman continuum limit ($\lambda >$912 Angstrom) that ionises the interstellar gas, forming HII regions. This HII region evolves, along with the main sequence lifetime of the central star, from a deeply

Radio and Near-Infrared Composite of W49A

Figure 1.2: Three colour composite of the massive star forming region W49A. The red features of the image represent regions of ionised gas. In the centre of the image, a detected chain of UCHIIs illustrates the gregarious nature of massive star formation.

embedded hypercompact state ($\sim 0.003\,\text{pc}$) to a classical nebula ($\sim 10\,\text{pc}$). Considering the different sizes of the HII regions as a signature of age, the UCHII region observational definition attends to the diameter ($\leq 0.1\,\text{pc}$), the density ($\geq 10^4\,\text{cm}^{-3}$) and the brightness (EM$\geq 10^7\,\text{pc}\,\text{cm}^{-}6$). Their SED peaks at around $100\,\mu\text{m}$, making them the most luminous objects of the Galaxy at this wavelength, due to the presence of surrounding dust that reprocesses most of the stellar luminosity into far infrared radiation. For this reason, when studying the massive stars within these objects, the SEDs are so dominated by this dust that the star can mimic into a much younger object, making indirect observations extremely important.

Because of the very early development of high spatial resolution radio Astronomy, UCHII regions were first discovered and characterised at radio wavelengths, where the free-free emission is optically thin, through the dust cocoon that surrounds the ionised region. The candidates to search for UCHII were extracted from the IRAS Point Source Catalogue, attending to a selection criteria based on the infrared colours (e.g. Selection criteria Kurtz et al. (1994): $\log(\text{F}_{60}/\text{F}_{12}) \geq 1.30$, $\log(\text{F}_{25}/\text{F}_{12}) \geq 0.57$ and $\text{F}_{100} \geq 1000$ Jy). Major surveys of UCHIIs (Wood and Churchwell, 1989; Zoonematkermani et al., 1990; Garay et al., 1993; Miralles et al., 1994; Kurtz et al., 1999) have mostly concentrated on the very compact emission.

UCHIIs present different morphologies that reflect their age, dynamics and interaction with the parental molecular cloud. They were first classified attending to their morphologies by Wood and Churchwell (1989) into cometary, core-halo, shell and irregular or multiply peaked structures. Later on, the bipolar type was also included in this scheme with a very few objects (e.g. NGC7538IRS1, G45.48+0.13, W49A-A, K3-50A). A full understanding of the

nature of these morphologies is directly related to the lifetime problem of the Hii region. The theoretical models that try to explain the morphologies and lifetimes of Hii regions assume that the ambient medium is homogeneous in temperature and density. When the star begins to emit UV photons the ionisation front moves rapidly outwards until the number of photoionisations and recombinations are in equilibrium. At this point, the Hii region fills a certain volume, whose radius is called the Stromgren radius. This process is extremely fast, lasting typically a few years for hot stars. After this initial rapid expansion, the heated ionised gas expands because of the difference in pressure between the ionised gas and the surrounding neutral gas, creating a shock front. This expansion stops when the hot, and lower density, ionised gas reaches equilibrium in pressure with the surrounding cool ambient medium. UCHiis are too numerous if one considers that the compact state can last up to $\sim 10^5$ yr. To solve this problem, numerous hypothesis on the dynamical nature of UCHiis have been proposed: champagne flow or blister models, infall models, photo-evaporating disks, stellar wind-supported bow shock, etc. These different hypothesis are likely valid in different stages of the ultra compact phase.

Since the free-free emission is generated by the accelerated electrons, released in the process of photoionisation by the stellar emission, the optically thin emission allows to derive the Lyman continuum photon rate needed to be produced by a single massive star. The relationships between physical parameters obtained from the UCHiis and their probable ionising sources derived by Garay and Lizano (1999) revealed that the most compact regions seem to be excited by less luminous stars than the classical compact Hii regions. A possible implication of this effect is that some of the most compact UCHiis could be externally ionised objects that belong to larger, complex and inhomogeneous Hii regions. On the other hand, Garay et al. (1993) found that many compact regions of ionised gas can indeed be resolved in complex structures in the radio continuum, suggesting that these complex morphologies are produced by multiple sources, and therefore, unveiling clusters of OB stars. This is consistent with the general idea that massive stars tend to form in groups. In this area, NIR photometry is crucial to detect the counterparts of these clusters.

The initial surveys of UCHiis suffered from a clear observational bias: they were insensitive to scales larger than $20''$. Recent studies (Koo et al., 1996; Kim and Koo, 1996; Kurtz et al., 1999) addressed this problem for several UCHiis in which there exist a very extended radio emission, underlying the previously detected compact emission (see Fig. 1.3). This would imply that for the cases in which the extended emission is actually associated to the compact one, former studies had underestimated for some cases the spectral types of the exciting stars, and may had missclasified the morphology (Franco et al., 2000; Kurtz and Franco, 2002). However, the question on which mechanism could explain localised pockets of high density, ionised gas whithin a much larger and lower density ionised region, remains.

1.2.1   Ionising sources

The definition of the unit of massive star formation is still highly debated. UCHii regions are assumed to be produced at least by one massive star, but whether they actually harbour the star or what is their actual IMF remain unclear. The first methods used to determine the temperature of the stars responsible of the ionised regions were the analysis of the spectral energy distribution (SED) especially at IR wavelengths, and the inference of the rate of Lyman continuum photons necessary to produce the detected radio continuum emission. The first technique suffered from poor spatial resolution, while the latter does from the strong
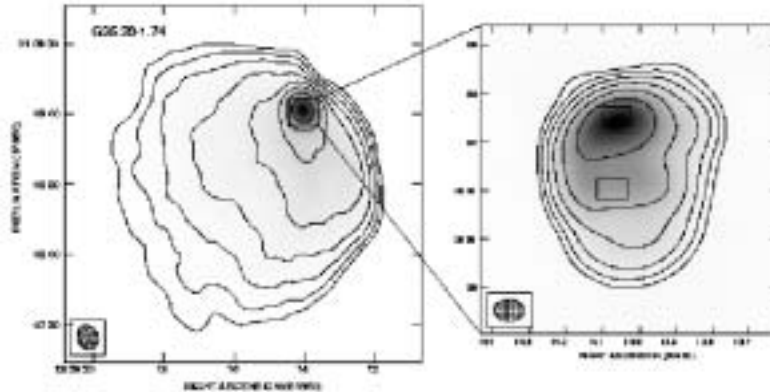
Figure 1.3: VLA maps of the G35.20-1.74 Ultra-compact HII region, as shown in Kurtz and Franco (2002). Left: Low resolution VLA map (9″) and sensitivity to arcminute scales. Right: High-resolution VLA map as shown in Kurtz et al. (1994) (0.″9) and sensitivity in the arcsecond scale.

assumptions used (e.g. single ionising star, distance determination).

Only recently, the development of NIR detectors and high-resolution instruments (such as Adaptive Opticys sytems) have allowed the direct study of the stellar populations of UCHIIs, with the spatial resolution that these compact objects require in order to disentangle stellar sources from close companions and extended emission (resolving distances <600 AU at 2 kpc distance). Moreover, at NIR wavelengths, the visual extinctions towards some of the embedded objects can *just* be overcome, profiting from the gain in sensitivity and contrast that AO systems provide.

The identification of the massive stars responsible of the regions of ionised gas through direct photometric observations of these stars is not straightforward. Classification through broadband brightnesses and colours is a widely used technique (Feldt et al., 1999, 1998, 2003; Henning et al., 2002; Stecklum et al., 1998; Pratap et al., 1999; Alvarez et al., 2004; Bik et al., 2002), that depends strongly on the estimated distance to the UCHII, normally determined dynamically by measurements of molecular lines. With this method, the stars that present excesses are even more difficult to classify, while the cross-checking with radio information yields differences between the different estimates (Alvarez et al., 2004). Spectra in the the 2-8 μm regime have been used to analyse the spectral type of the ionising sources of UCHIIs (Hanson et al., 2002a; Martín-Hernández et al., 2002; Bik et al., 2002; Kaper et al., 2002b; Okamoto et al., 2001, 2003b; Takahashi et al., 2000). The combination of the information from photospheric lines, the independent estimate of the extinction towards the star and the modelling of nebular emission lines, yields a more accurate estimate of the stellar parameters.

1.2.2 Kinematics

Massive stars have a very strong dynamical impact in their surroundings. The cause may be the density structure of the ambient medium, stellar winds or the motion of the stars with respect to the molecular cloud, or the combination of all these factors.

One of the most common features of star formation in the low-mass regime is the ubiquous

presence of outflows as a mechanism to shed angular momentum, allowing the matter in the disc to migrate to the central star. This very clear signature of the accretion scenario for star formation is also present in massive stars (Table 3 of Garay and Lizano (1999)) (Kumar et al., 2003). However, 3D-hydrodynamical models show that radiation pressure halts accretion before forming stars more massive than 40 $M_\odot$ (Yorke, 2003).

Unlike in the low-mass regime, massive outflows appear to be not well collimated (see Fig. 1.4), but this effect has been proposed to be a result of poor angular resolution when disentangling numerous outflows (Beuther et al., 2002).
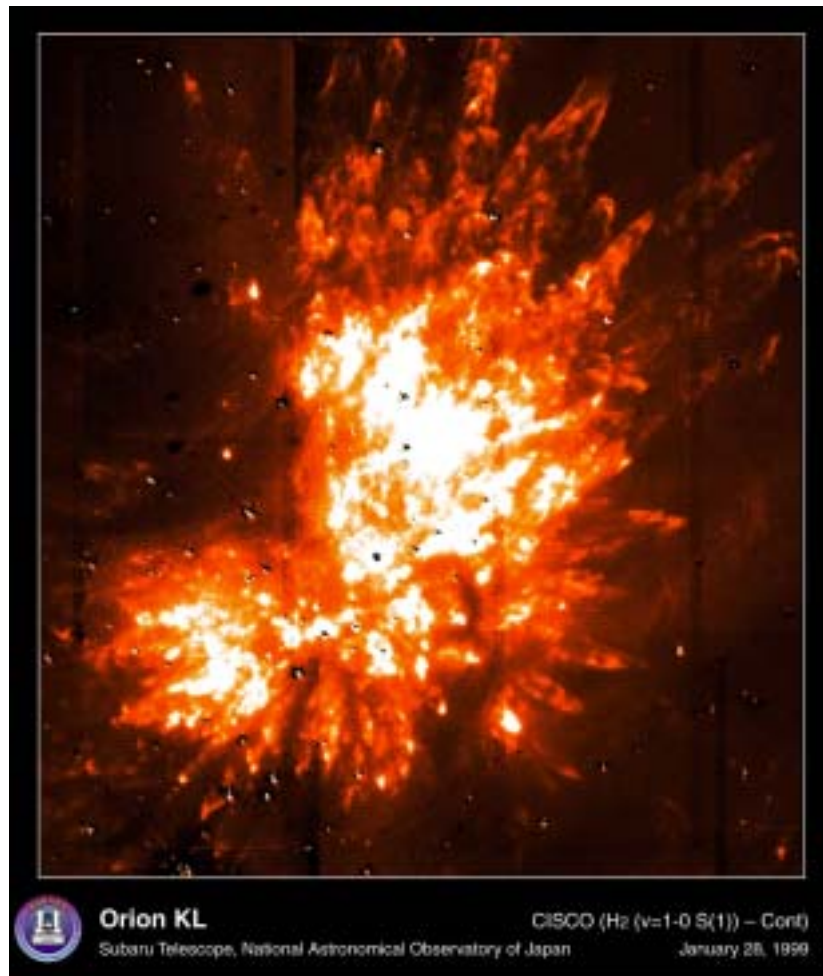
Figure 1.4: 2.12 μm image of Orion KL nebula, obtained in 1999 with the Subaru Telescope. The central star (not visible in this image) that produces this outflow is IRc2 and the terminal velocities of the emanated material are above 100 km s^{-1}.

The study of radio recombination lines reveals that the line width in UCHiis is considerably broader than in diffuse Hii regions (Garay and Lizano, 1999). This broadening is more pronounced in the non-thermal component of those lines. Champagne flows, stellar winds, expansion of substructures into less dense material inside the UCHii and magnetic turbulence are the possible responsibles for this effect. Each of these phenomena produce different

kinematics.

1.3   Outline of This Thesis

To fully understand the formation of massive stars and their influence back on the molecular cloud, a detailed knowledge of the the physical conditions of the environment prior to and after the formation of the star is needed. In this thesis, I will concentrate on the second point, analysing some examples of YSO and UCHiis at high spatial resolution (with the help of Adaptive Optics systems) in order to identify the ionising sources, understand the interaction of these stars with their surroundings and explain their morphology.

Chapter 2 is an introduction to the use of polarimetric maps, through the so-called Weintraub's method, in order to determine the dominant illuminating source(s) and to uncover the presence of very embedded objects that are not detected with NIR photometry. The application of this method on the observations of the regions S106 and G77.96-0.01 will be shown and discussed. Chapter 3 shows the use of this same technique to predict the presence of an illuminating source in one of the components of the UCHii G61.48+0.09, that is finally confirmed with high spatial resolution observations at a longer wavelength. The combination of broad band information with the emission in the Brγ nebular line and the visual extinction allow a classification of the spectral energy distribution of two possible ionising stars. The non detection of emission of shocked molecular hydrogen provides a limit on the kinematics of the region. Chapter 4 is devoted to the spectroscopic analysis of the stars within this same UCHii region and the nebular emission of the surroundings. Finally, Chapter 5 constitutes the study of the kinematics of one of the most debated UCHii: G5.89-0.39, focusing on two different tracers: the emission of shocked molecular hydrogen on the larger scale and the ionised gas close to the only detected star up to date. The summary and prospects for the future work in the field are addressed in Chapter 6.

Chapter 2

Seeking for Hidden Stars: S106 and G77.96-0.01

2.1   Introduction

The dusty nature of the regions where massive star formation is taking place, mentioned in Chapter 1, imposes a very strong observational limitation. At NIR-wavelengths, many of these young stars just start to be visible, while many others remain undetected. These stars, the most embedded ones, are supposed to be closer to the youngest formation phases, and therefore the puzzle of the UCHɪɪs and of massive star formation itself is not complete without their characterisation. In these cases, indirect methods are very valuable, if not the only way to unveil them.

Reflection nebulae are commonly found, at optical- and NIR-wavelengths, surrounding YSO. Intrinsic polarisation in the nebula is due to scattering of stellar light by dusty material in the cases where there exist enough dust grains in the circumstellar material, the size of the dust particles is the same or smaller than the observed wavelength, and the environment between the emitter and the scattering dust is optically thin.

Linear polarimetric maps have been used in YSOs to study several issues of star formation

- The composition and properties of dust in the circumstellar region. (Pendleton et al., 1990; Kim et al., 1994)

- The geometry and the structure of outflow cavities opened by the YSO. (Hodapp, 1984; Yamashita et al., 1987; Lacasse et al., 1981; Aspin et al., 1990, 1989; Weintraub et al., 1993)

- Detection of circumstellar discs and, through their orientation, derivation of the outflow direction (Bastien and Menard, 1990; Tamura et al., 1991; Brandner and Potter, 2002)

This technique is also used to differentiate scattering peaks of nebular knots (i.e. false stars) from self-illuminated objects (i.e. real stars). This is possible thanks to the characteristic centrosymmetric pattern that is expected to be centred around the illuminating source(s) (see Sect. 2.2). Monte-Carlo radiative transfer codes model most of these properties and become a necessary tool to interpret the polarimetric information (Bastien and Menard, 1988; Whitney and Hartmann, 1992; Fischer et al., 1994, 1996; Lucas and Roche, 1997).

In massive star-forming regions, the linear polarisation maps have been used to unveil the embedded sources (Lacasse et al., 1981; Yao et al., 2000; Stecklum et al., 1998; Henning et al., 2002) in the way to determine the illuminating, and possibly ionising source responsible of the HII region.

In the following sections, the method to seek for hidden stars will be discussed and two applications will be presented.

2.2   Polarisation by dust in Reflection Nebulae

Dust is present in many astronomical environments, playing a very important role (e.g. molecular clouds with star formation, evolved giant stars and ejecta of supernovae). This presence is most evident at infrared wavelengths. In the visible and NIR, dust absorbs and scatters light, giving rise to extinction.

The dust is quite satisfactorily modelled as spherical particles, with a range of sizes and mainly composed of dielectric substances. In an analogous way to the atomic Lorentz's theory of the harmonic oscillator, the grain of dust is considered as a spherical system of harmonic oscillators because it describes successfully some phenomena that occur both in the atomic and in the macroscopic level. When light propagates through these dust particles, the electric field of the light wave induces oscillating electric dipoles in the atoms and molecules of the medium. These induced dipoles are responsible for the optical characteristics of the different materials, namely absorption and refraction. In addition to this, the dipoles scatter the light in various directions. Scattering (as described in Mie's theory) has a dependence on the ratio between the size of the particle and the frequency of the incident light, but there is also a polarisation effect.

When the electromagnetic field is considered as a harmonic wave in the **z**-direction, and it reaches a dipole (i.e. at the origin of the coordinate system), some light is scattered into a certain direction given by the unit vector **e**. The plane defined by the incident and scattered directions is called the *scattering plane*.

The amplitude of the impinging electric field $\mathbf{E}_i$ can be split into two components: one parallel and the other perpendicular to the scattering plane, with modulus $E_{i\parallel}$ and $E_{i\perp}$, respectively. The scattered electric field ($\mathbf{E}_i$) can be decomposed in the same way into $E_{s\parallel}$ and $E_{s\perp}$. The relation between these components, at large distance from the particle is described by

$$\begin{pmatrix} E_{s\parallel} \\ E_{s\perp} \end{pmatrix} = \frac{e^{i\mathbf{k}(r-z)}}{-i\mathbf{k}r} \begin{pmatrix} S_2 & S_3 \\ S_4 & S_1 \end{pmatrix} \begin{pmatrix} E_{i\parallel} \\ E_{i\perp} \end{pmatrix} \tag{2.1}$$

where the amplitude scattering matrix consists of four elements S_j that depend on the scattering direction, specified by the unit vector **e** or by two angles θ and ϕ.

The scattering matrix for a small grain of unit volume, whose dipole, produced by the incident wave, if its polarisability α is isotropic is $\mathbf{p} = \alpha \mathbf{E}_i$ and scattered electric field is $\mathbf{E}_s = \frac{\omega^2 \alpha}{c^2 r}(\mathbf{e} \times \mathbf{E}_i) \times \mathbf{e}$, follows

$$\begin{pmatrix} S_2 & S_3 \\ S_4 & S_1 \end{pmatrix} = -i\mathbf{k}\alpha \begin{pmatrix} cos\theta & 0 \\ 0 & 1 \end{pmatrix} \tag{2.2}$$

From Fig. 2.1 is evident that $E_{s\parallel} = cos\theta E_{i\parallel}$ and $E_{s\perp} = E_{i\perp}$, thus the scattered electric field will be maximum in the perpendicular directions to the dipole axis, and no radiation is scattered along the direction of the axis.
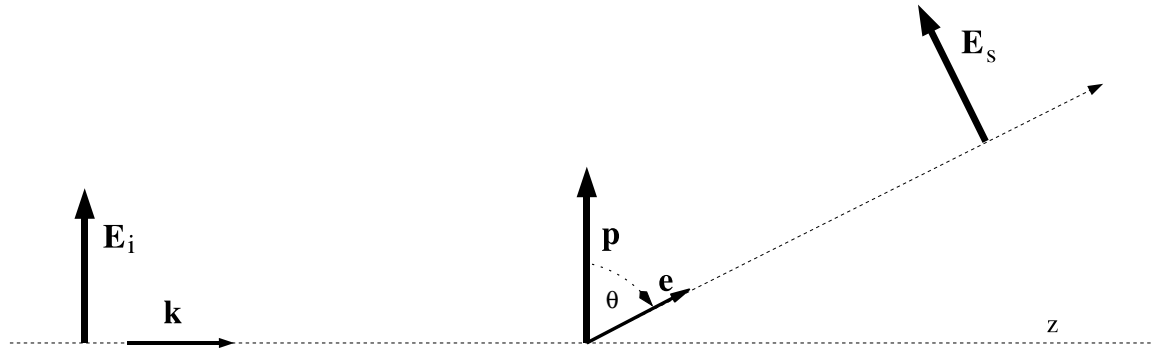
Figure 2.1: Diagram of an incident wave in the direction $\mathbf{k}$, with electric field $\mathbf{E}_i$ that excites a dipole $\mathbf{p}$, scattering the electric field along the direction of the vector $\mathbf{e}$. The resultant scattered electric field is $\mathbf{E}_s$. An incident wave oriented in the perpendicular direction to the scattering plane would produce a scattered electric field also in the perpendicular direction (Kruegel, 2003).

In the case of a sphere, the amplitude scattering matrix (2.2) also acquires a diagonal structure because the elements S_3 and S_4 vanish. S_1 and S_2 are only functions of $\nu = \cos\theta$, and depend on the boundary conditions of the electromagnetic field at the surface of the dust grain.

Fig. 2.2 represents the interaction of a plane wave, polarised in the y- and x-direction in panels (a) and (b) respectively, with a dipole. Panel (c) depicts the scattered emission by the dipole when the incident light is unpolarised. The scattered light will be unpolarised in the forward direction and linearly polarised at right angles from the scattering plane.

A plane harmonic wave of angular frequency ω, wavenumber $\mathbf{k}$ and electric field $\mathbf{E}(\mathbf{x}, t) = \mathbf{E}_0 \cdot e^{i(\mathbf{k}\cdot\mathbf{x} - \omega t)}$, that travels in the z-direction of a Cartesian coordinate system, has a complex amplitude that describes an ellipse in the $(x - y)$-plane along with time.

$$\text{Re } \mathbf{E} = \mathbf{E}_0 \sin(\beta)\cos(\omega t) + \mathbf{E}_0 \cos(\beta)\sin(\omega t) \tag{2.3}$$

where β denotes an angle whose tangent is the ratio of the major and minor axes of the ellipse. The polarisation ellipse is described by the length of the major and minor axes, and the angle between the major axis and the x-axis. The Stokes parameters are equivalent to these geometrical quantities. The advantage of using the Stokes parameters is that from γ-rays to infrared the electric fields cannot be measured directly. Instead, the detectors are based on the detection of signals proportional to the square of the electric field vector (i.e. intensity of the field), just in the same way as the Stokes parameters.

When a plane harmonic wave is scattered by a spherical grain, the Stokes parameters of the incident and scattered wave are linearly related through

$$\begin{pmatrix} I_s \\ U_s \\ Q_s \\ V_s \end{pmatrix} = \frac{1}{k^2 r^2} \begin{pmatrix} S_{11} & S_{12} & 0 & 0 \\ S_{12} & S_{11} & 0 & 0 \\ 0 & 0 & S_{33} & S_{34} \\ 0 & 0 & -S_{34} & S_{33} \end{pmatrix} \begin{pmatrix} I_i \\ U_i \\ Q_i \\ V_i \end{pmatrix} \tag{2.4}$$

(a)

(c)

(b)
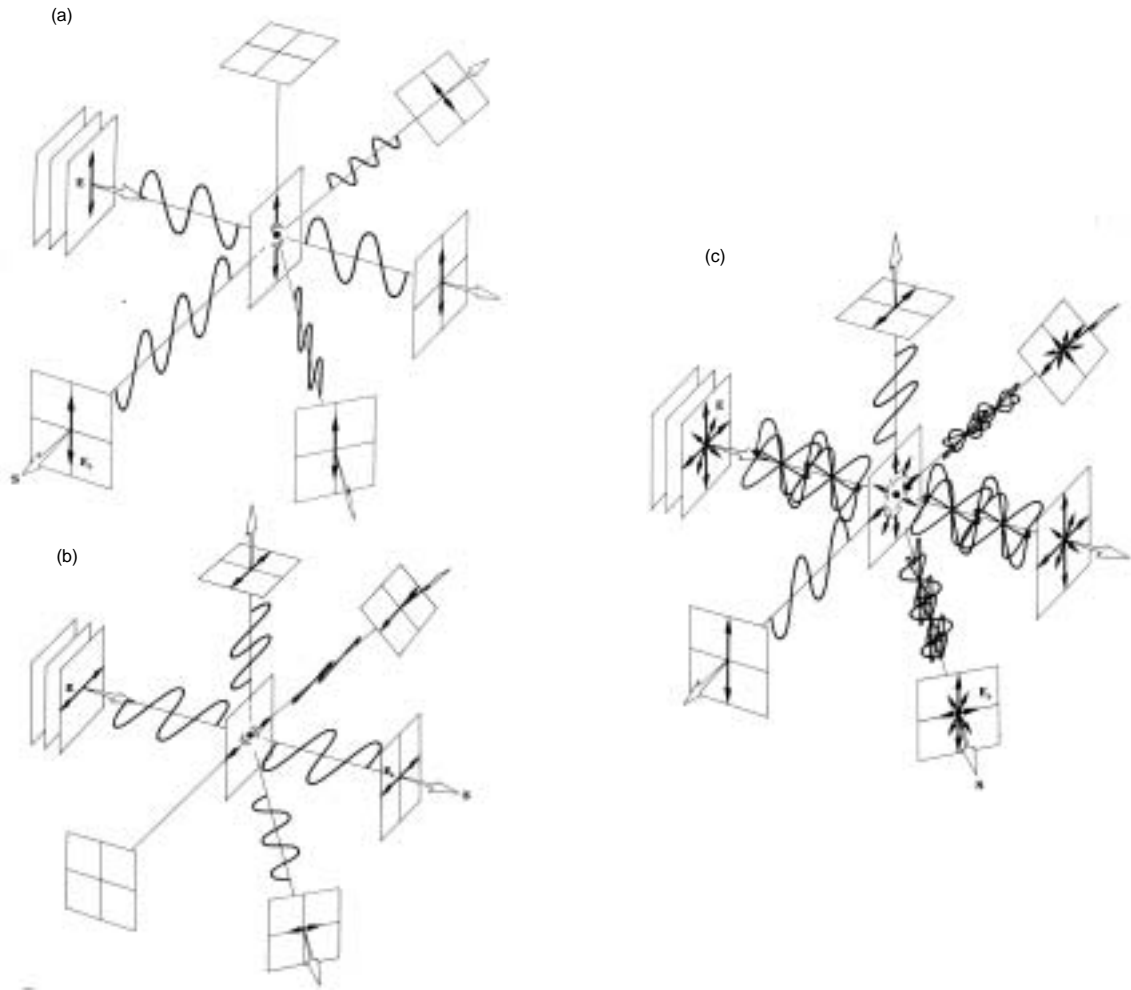
Figure 2.2: (a) and (b) Scattering by a dipole of linearly polarised light in the y-direction and x-direction, respectively. (c) Scattering of unpolarised light by a dipole. Figures obtained from Hecht and Zajac (1974).

where the S_{ij} are functions of the scattering angle (θ) and relate to the coefficients of Eq. (2.1) with the relations

$$S_{11} = \frac{1}{2}\left(|S_1|^2 + |S_2|^2\right) \tag{2.5}$$
$$S_{12} = \frac{1}{2}\left(|S_2|^2 - |S_1|^2\right)$$
$$S_{33} = \frac{1}{2}\left(S_2^* S_1 + S_2 S_1^*\right)$$
$$S_{34} = \frac{i}{2}\left(S_1 S_2^* - S_2 S_1^*\right)$$

and the polarisation degree is given by the quantity

$$p = \frac{|S_1|^2 - |S_2|^2}{|S_1|^2 + |S_2|^2} = -\frac{S_{12}}{S_{11}}. \tag{2.6}$$

Reflection nebulae are clouds of interstellar gas and dust in the proximity of bright stars that scatter and reflect (in the case of very big grains) the stellar emission. Their characteristic appearance in polarimetric maps is a centrosymmetric pattern of polarisation vectors perpendicular to the radial vector pointing toward the star. The previous section displays the basic explanation to this effect, but the details of the maximum polarisation degree and direction of maximum polarisation in the scattering plane are sensitive to size, shape and optical constant of the particle (m).

2.2.1 Analysing Polarised Light

As mentioned in the previous section, polarisation is best described by means of the Stokes parameters. The electric vector in the $(x - y)$-plane can be split into two components:

$$E_x = E_1 \sin(\omega t - \varphi_1) \tag{2.7}$$
$$E_y = E_2 \sin(\omega t - \varphi_2)$$

The Stokes parameters are four bilinear combinations of E_1, E_2, φ_1 and φ_2 (Chandrasekhar, 1950). They can also be referred to the $(x' - y')$-reference system (see Fig. 2.3) through the equation (2.3).
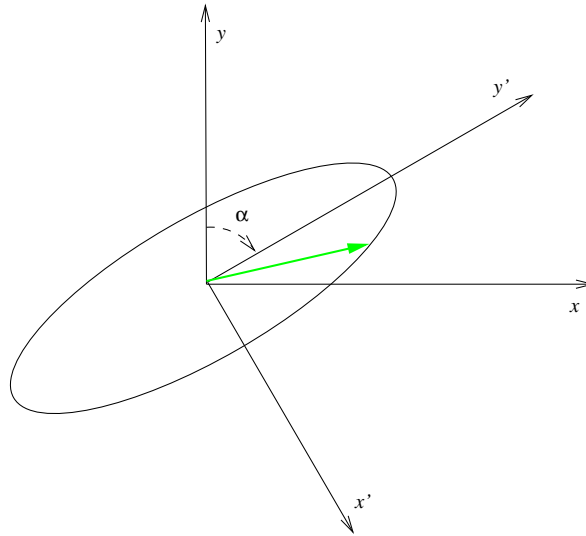
Figure 2.3: Polarisation ellipse described by the electromagnetic field with time, represented by the green arrow.

The expression of the Stokes parameters in both systems is

$$I = \qquad E_1^2 + E_2^2 = \qquad (Q^2 + U^2 + V^2)^{1/2} \tag{2.8}$$
$$Q = \qquad E_1^2 - E_2^2 = \qquad I \cos 2\beta \cos 2\alpha \tag{2.9}$$

$$U = -2E_1 E_2 \cos(\varphi_1 - \varphi_2) = I \cos 2\beta \sin 2\alpha \tag{2.10}$$

$$V = 2E_1 E_2 \sin(\varphi_1 - \varphi_2) = I \sin 2\beta \tag{2.11}$$

For pure linearly polarised light $V = 0$, and the polarisation degree of the light is

$$p = (Q^2 + U^2)^{1/2}/I \tag{2.12}$$

.

Substitution of Eq. (2.9) and (2.10) into this expression leeds to $Q = p \cdot I \cos 2\theta$, and $U = p \cdot I \sin 2\theta$, and thus the orientation of the polarisation is given by

$$\tan 2\theta = \frac{U}{Q} \tag{2.13}$$

The study of the polarisation state of light makes use of optical devices such as the polariser that transmits only the vibration in the plane determined by a certain direction (i.e. an angle ϕ) of the polariser. The transformation of the Stokes parameters accompanying the passage of light through the ideal polariser is described in Kruegel (2003) by

$$\begin{pmatrix} I' \\ Q' \\ U' \\ V' \end{pmatrix} = \begin{pmatrix} 1 & \cos 2\phi & \sin 2\phi & 0 \\ \cos 2\phi & \cos^2 2\phi & \cos 2\phi \sin 2\phi & 0 \\ \sin 2\phi & \cos 2\phi \sin 2\phi & \sin^2 2\phi & 0 \\ 0 & 0 & 0 & 0 \end{pmatrix} \cdot \begin{pmatrix} I \\ Q \\ U \\ V \end{pmatrix} \tag{2.14}$$

The intensity measured at the detector will then depend on the angle of the polariser (e.g. wire-grid, wollaston) in the form

$$I'(\phi) = \frac{1}{2} \{ I + Q \cos 2\phi + U \sin 2\phi \} \tag{2.15}$$

and according to this, a set of measurements in four directions, separated by $45°$ is sufficient to derive the Stokes parameters through the equations:

$$I_{tot} = \frac{1}{2} (I_0 + I_{45} + I_{90} + I_{135}) \tag{2.16}$$

$$Q = (I_0 - I_{90}) \tag{2.17}$$

$$U = (I_{45} - I_{135}) \tag{2.18}$$

and thus the normalised Stokes parameters ($u = U/I$, $q = Q/I$). The substitution of these values in Eq. (2.12) and (2.13) determine the polarisation degree and orientation of the electric field and the correspondent errors, computed through Gaussian propagation.

$$\sigma_p = \frac{\sqrt{u^2 \sigma_u^2 + q^2 \sigma_q^2}}{p} \quad \sigma_\theta = \frac{\sqrt{u^2 \sigma_q^2 + q^2 \sigma_u^2}}{2p} \tag{2.19}$$

If we assume that $\sigma_u = \sigma_q = \sigma_p$, the equation for σ_θ simplifies to

$$\sigma_\theta = \frac{\sigma_p}{2p} rad = 28.65° \frac{\sigma_p}{p} \tag{2.20}$$

2.2.2 Statistical Considerations

Linear polarisation measurements are subject to a bias. This bias arises from the calculation of the polarisation degree by determining the normalised Stokes parameters ($u = U/I$, $q = Q/I$). These measured Stokes parameters are estimates of the true normalised Stokes parameters (u_0, q_0). The degree of polarisation is defined from Eq. (2.12) as $p_0 = (q_0^2 + u_0^2)^{1/2}$, but the normally used estimator is $p = (q^2 + u^2)^{1/2}$ and it overestimates the true polarisation. Indeed, taking $q_0 = u_0 = 0$, the noise on the measured values of q and u yield a non-zero polarisation estimate.

Clarke et al. (1983) demonstrated that the probability function for normalised Stokes parameters is not a normal distribution, therefore, the joint distribution function for (q, u), once transformed to the (p, θ) coordinates and integrated over θ, gives the marginal distribution for p. This is the well-known Rice distribution for the degree of polarisation (Simmons and Stewart, 1985)

$$F(\mathrm{p}, \mathrm{p}_0) = \mathrm{p}e^{-\frac{(\mathrm{p}^2 + \mathrm{p}_0^2)}{2}} J_0(i\mathrm{p}\mathrm{p}_0), \qquad (2.21)$$

where J_0 is the zeroth order Bessel function, p and p$_0$ are actually p/σ_p and p_0/σ_p, respectively. Fig. 2.4 represents the Rice distribution for different values of p, showing that at low signal-to-noise ratio, the function presents skewness and kurtosis.
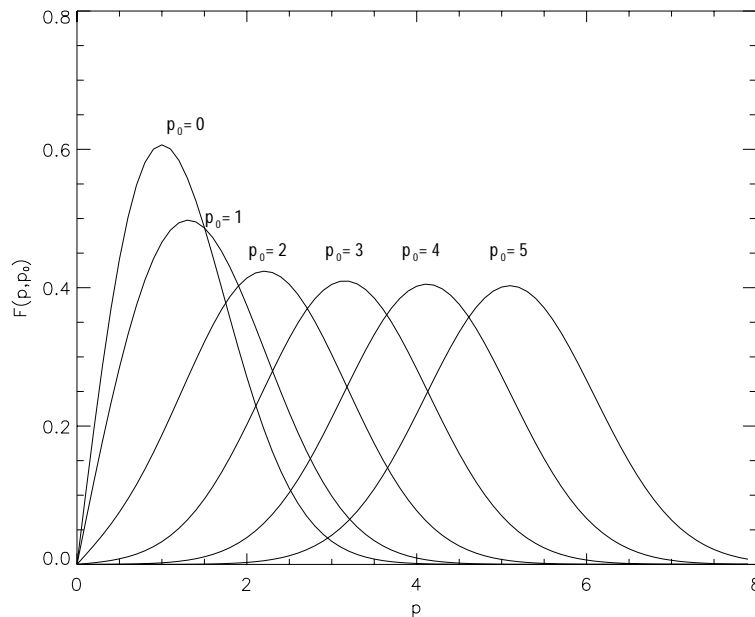
Figure 2.4: Illustration of the skewed behaviour of the Rice distribution as the signal-to-noise ratio decreases. This figure is published in Simmons and Stewart (1985)

There are four estimators of the true polarisation degree that can be used. Simmons and Stewart (1985) make a comparison between them, concluding that Wardle & Kronberg's estimator (Wardle and Kronberg, 1974) is the most adequate for the cases in which $p_0/\sigma_p > 0.7$, therefore this estimator will be used throughout this work. The function represented in Fig.

2.5 (Left) is used to derived the unbiased value of the polarisation degree for values of $p/\sigma_p < 6$ and the approximation $p_0 = \sqrt{p^2 - \sigma_p^2}$ in the cases of $p/\sigma_p > 6$.

For any estimator used, the confidence interval of the unbiased polarisation degree (p_0) can be calculated for the Rice distribution. Simmons and Stewart (1985) calculated the confidence interval [$\bar{p}$,$\underline{p}$ minimising the distance between the limits, implying then that $F(\bar{p}, p_0) = F(\underline{p}, p_0)$. The results of these intervals at the 1σ, 2σ and 3σ are presented in Fig. 2.5 (Right). For each measured polarisation degree (p), there exists an unbiased polarisation degree value (p_0) derived from the chosen estimator and a certain confidence interval of that value defined by the intersection of the value of p with each pair of functions in the graphic.
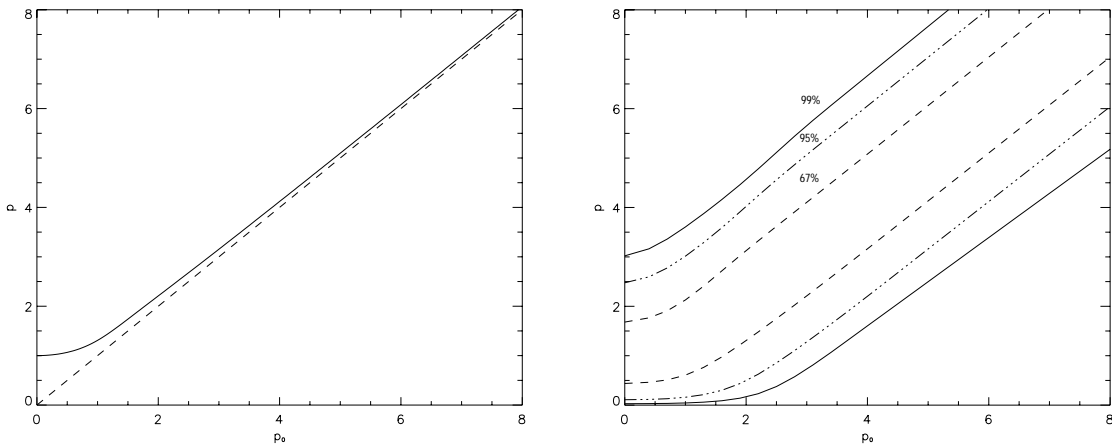
Figure 2.5: Left: Comparison of the Wardle & Kronberg's estimator in solid line with the unbiased estimator of p_0 (Simmons and Stewart, 1985). Right: Confidence intervals of the true polarisation p_0 at the $1\sigma(67\%)$, $2\sigma(95\%)$ and $3\sigma(99\%)$ from Simmons and Stewart (1985)

The marginal distribution for the orientation angle (θ) is the distribution function

$$G(\theta; \theta_0, p_0) = \frac{1}{\sqrt{\pi}} \left\{ \frac{1}{\sqrt{\pi}} + \eta_0 e^{\eta_0^2} \left[1 + erf(\eta_0)\right] \right\} e^{\left(-\frac{p_0^2}{2}\right)} \qquad (2.22)$$

where $\eta_0 = \frac{p_0}{\sqrt{2}} \cos 2(\theta - \theta_0)$, $p_0 = \frac{p_0}{\sigma}$ and erf is the Gaussian error function (Naghizadeh-Khouei and Clarke, 1993). The form of this equation is illustrated in Fig. 2.6 (Left).

The 1σ-confidence limit has been calculated by the numerical integration of the area under the function $G(\theta; \theta_0, p_0)$, for different values of p_0 and setting $\theta_0 = 0$ (see Fig. 2.6 (Right)).

2.2.3   Operational Calibrations

Astronomical polarisation degrees are relatively small, and therefore a carefull error calibration is important. These errors include:(a) background polarised flux, (b) polarisation degree zeropoint or instrumental polarisation, (c) scale error in the polarisation degree and (d) zeropoint in the polarisation angle.

Moonlit sky or galactic radiation are responsible for the polarised background present in polarimetric observations. This effect is especially noticeable in faint extended regions, such as reflection nebula. However, NIR observations are strongly dominated by the thermal
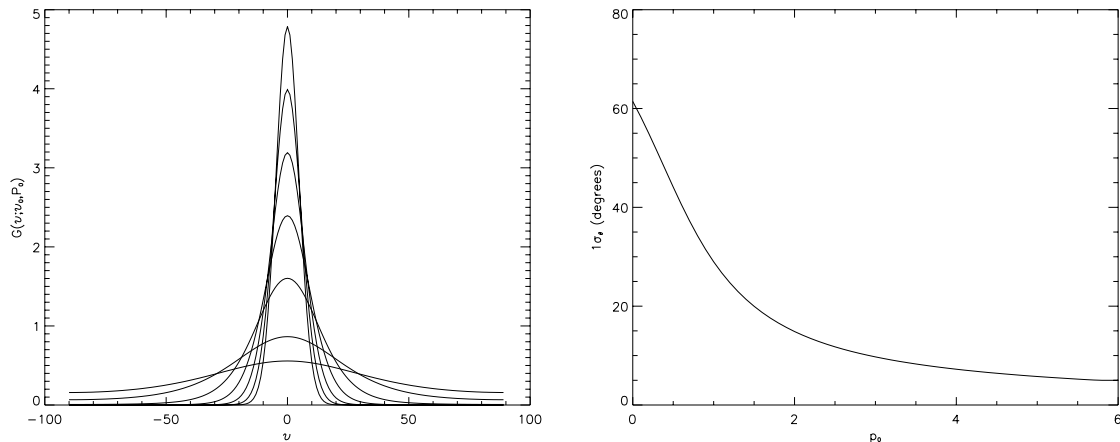
Figure 2.6: Left: Marginal distribution of the orientation angle $G(\theta; \theta_0, p_0)$ as function of θ for values of $p_0 = 0.5, 1, 2, 3, 4, 5, 6$. Right: 1σ confidence interval of the probability function $G(\theta; \theta_0, p_0)$.

emission of the atmosphere and the telescope, that also varies rapidly with time; for this reason, the observations are designed to achieve an optimal subtraction of the background, either by frequent sky-dips or by construction of a sky frame with a jittering pattern around the scientific target.

Telescopes and Instruments polarise the radiation to some extent. The sources of this polarisation are various: reflections or refractions of the beam by $45°$, different transmissivity of the polarisers, etc. In order to quantify this instrumental effect, the observation of an unpolarised standard is needed. This polarisation is vectorially added to the true polarisation signal, and thus vectorially subtracted during the reduction. Alternatively to the observation of an unpolarised standard star, the average of the polarisation degree of a randomly selected set of nearby stars of low polarisation can also be used for this purpose.

When the polarised light passes through a polarimeter an instrumental depolarisation occurs due to the non-perfect performance of analysers, in the way that an initial polarisation degree $x\%$ will be recorded as having a polarisation degree $\epsilon x\%$, ϵ being the efficiency. This polarimetric efficiency is calibrated by observing a polarised standard star (Whittet et al., 1992). Standard sources must also be calibrated themselves from the previous effects (see Fig. 2.7).

Finally, the reference of the polarisation angle with respect to some instrumental zeropoint must be set, although some measurements only need relative polarisation angles. The observation of a standard star with known polarisation angle sets the zeropoint in the angle. This is illustrated in Fig. 2.7, where the normalised intensity (with respect to the average) of the polarised standard HD38563C is represented with respect to the polariser orientation. The effect of the instrumental polarisation is corrected by the division of the data by the normalised intensities of the unpolarised star HD42807. The comparison of the polarisation parameters for the polarised standard given by Whittet et al. (1992) ($p = 2.21 \pm 0.55\%$, $\theta = 78° \pm 1.7°$) with the estimated ones sets an efficiency of $\epsilon = 0.82$ and a correction to the zeropoint of $-2°$.
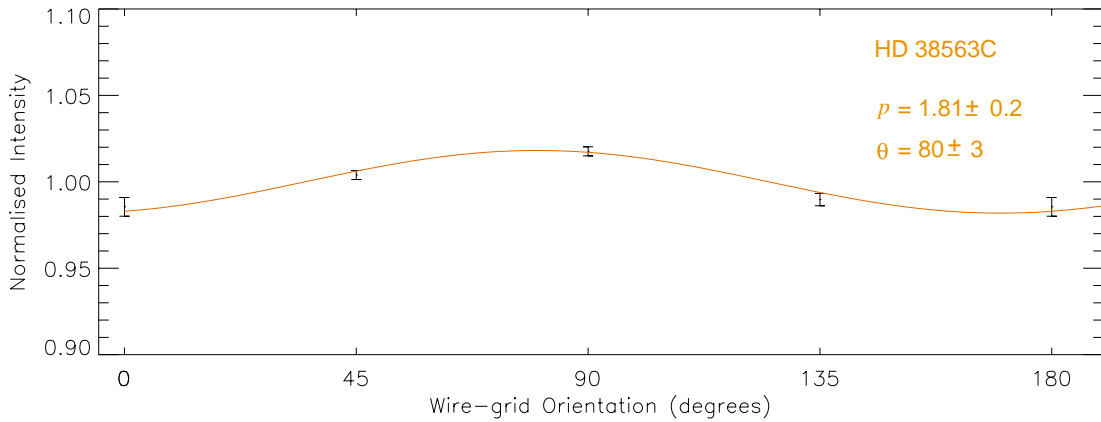
Figure 2.7: Polarisation curve of the polarised standard HD38563C, once corrected from instrumental polarisation with the normalised intensity of the star HD42807. The solid line represents the fit to the data. The parameters obtained with the Lavenberg-Marquardt least-squares fit are indicated in the upper right corner.

2.3   Weintraub's Method

The method, used to determine the location of the illuminating source of a reflection nebula, is based in the one developed by Weintraub and Kastner (1993). This method consists on calculating the crossing point (x_c, y_c) of the lines perpendicular to the polarisation vectors for each pair of vectors in the polarisation map. A weighting factor is calculated for every crossing point by multiplying the inverse of the uncertainties of the polarisation orientation of both vectors.

In order to accurately determine the centroid location, an iterative scheme is used. The first estimate of (x_c, y_c) is determined by calculating the mean of the solutions, together with the standard deviation. During subsequent iterations these calculations are repeated, but excluding the solutions that lie more than 3σ from the previous estimate of (x_c, y_c).

To illustrate the results of the method, a set of synthetic polarimetric map of a reflection nebula was produced. A $20''$-diameter centrosymmetric pattern, sampled with a pixelscale of $0''.32$, was generated to represent a reflection nebula, with a linear increment of the polarisation degree (see Fig. 2.3 for a radial profile of the polarisation degree for different geometries). Fig. 2.9 represents the polarimetric map for two error values of the orientation of the polarisation vectors ($5°$ and $10°$ respectively). Panels (a) and (b) represent the polarisation map if the entire reflection nebula is visible. The location of the illuminating source is coinciding with the centre of the nebula, but the 1-σ uncertainty ellipse increases with the uncertainty of the orientation of the vectors. Panels (c) and (d) depict the same calculation when only a partially centrosymmetric panel is visible (e.g. the rest of the intensity is obscured by foreground material). In this case, the centre of the uncertainty ellipse is displaced from the location of the star according to the error in the orientation of the polarisation vectors. Panels (e) and (f) show a slightly worse effect on the determination of the location of the illuminating source when the most inner vectors (i.e. the most noisy ones) are not detected.
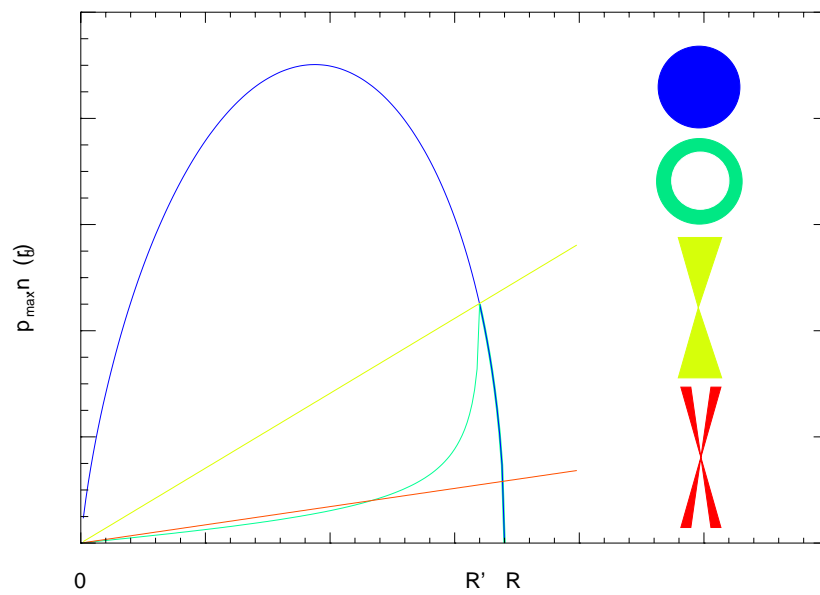
Figure 2.8: Radial profile of the integrated polarisation degree in the line of sight of four different geometries: sphere of radius R, shell of internal and external radii R′ and R, respectively, biconic with opening angle 15° and biconic with cavities of walls of 5°. A constant linear density (n_d) is assumed for all cases. The value p_{max} depends on the composition of the grains.
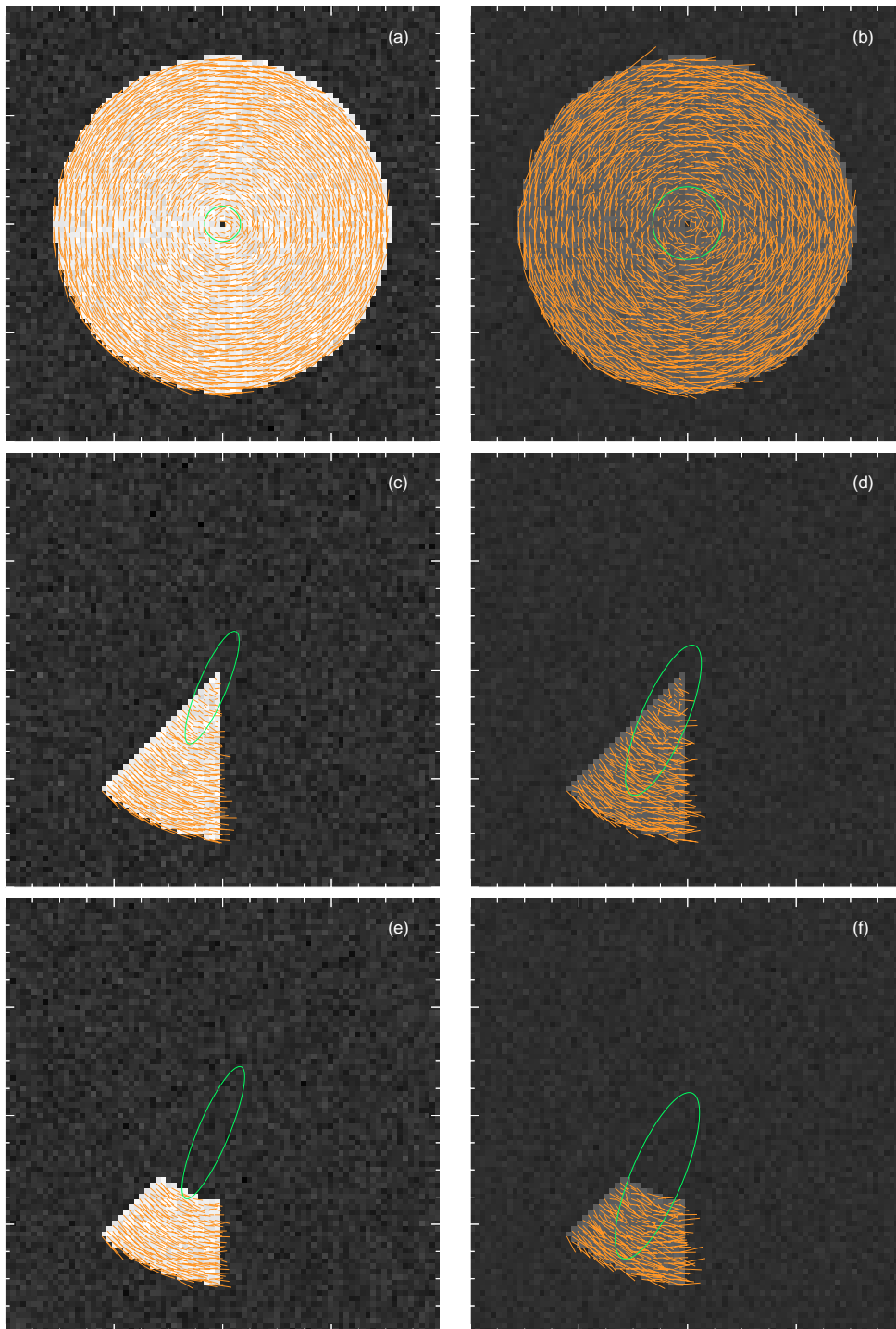
Figure 2.9: Models of polarimetric maps of a $10''$-diameter-reflection nebula in which the illuminating source is located at the centre of the maps. The degree of polarisation varies linearly from 5% to 40% with the radius. The maps have been modelled with $5°$ and $10°$ of error in the orientation for the left and right column, respectively. The green ellipse indicates the 1-σ uncertainty in the location of the illuminating source.

Object	Filter	IT[a]	pixelscale	FWHM[b]	Reference star	mag/band
		(s)	($''$/pixel)	($''$)		
S106	K' +wire − grid	$190{\times}5$	0.08	0.6	N033300164[c]	10.38/V
G77.96-0.01	K	210	0.04	0.5	CCDM J20296+3901D	11.4/V

Table 2.1: Observational polarimetric data

[a] Integration time.

[b] Spatial resolution at the reference star.

[c] GSC2 at ESO.

2.4   Circumstellar discs

Scattering models show that optically thick equatorial regions of reflection nebula correspond to discs in which multiple scattering translates into a departing of the patterns from centrosymmetry (Bastien and Menard, 1988, 1990). These vectors are characterised by low polarisation degrees and an orientation perpendicular to the symmetry axis of the bipolar nebula.

The detection of small circumstellar discs (radii ≤ 100 AU) is limited by the spatial resolution of the observations, since the photons detected can correspond to scattering from the material inmediately above or below (optically thin). Larger discs of radii in the range 10^3-10^4 AU are more likely to be detected (Weintraub et al., 1999). Comparison of the observations with scattering Monte Carlo models can also yield the inclination angle of these discs (Bastien and Menard, 1990).

2.5   Observations and Data Reduction

The polarimetric data of S106 and G77.96-0.01 was obtained during the commissioning time and subsequent observations of the Adaptive Optics system ALFA (Kasper et al., 2000) at the 3.6 m telescope on Calar Alto, between 2000 and 2002. In the case of S106, the polariser used was a set of four wire-grids of the OMEGA-Cass camera at four different orientations ($0°$, $45°$, $90°$ and $135°$) (Lenzen et al., 1998), whereas for G77.96-0.01 the $45°$ polariser was rotated to four directions in the sky ($0°$, $45°$, $90°$ and $315°$) to avoid the problem of the different transmissivity of each of the wire-grids.

Towards S106 a common jittering pattern was observed in order to produce a *moving sky* to subtract from the contributions of the background. Due to the higher resolution used for the images of G77.96-0.01, and thus the size of the extended emission, subsequent sky dips were obtained for this source for the same purpose. The data was coadded, sky subtracted and corrected from flatfield and bad pixels in the standard NIR reduction scheme. The images at different polarisation angles were registered and corrected from the instrumental polarisation by using numerous stars in the field, the polarisation of which is assumed to be zero on average. A polarised standard was observed in order to determine the zeropoint in the polarisation angle (θ). Since the interest of this study is mostly geometrical, the maps were not calibrated in flux. Other details of the observations are presented in Table 2.5.

2.6   Application I: S106

Sharpless 106 is a nearby (600 pc distance) bipolar H$_{II}$ region located near the centre of the 10^4 M$_\odot$ molecular cloud (Lucas et al., 1978; Bally and Scoville, 1982). This nebula appears in visual wavelengths as two conical cavities with an axis of symmetry at a position angle of $30°$ (Bally et al., 1998). The two lobes are separated by a dark lane, the northern lobe being more extincted than the southern one. Optical spectroscopy confirms that the gas in the north is redshifted, whereas the gas is the south is moving towards the observer (Solf and Carsenty, 1982). At NIR wavelengths a stellar source is visible at the location of the dark lane, together with eight other sources within a distance of $20''$ to the central source. This star ($\sharp$IRS 4 (Gehrz et al., 1982)) appears to be the source of ionisation and illumination of the nebula (Sibille et al., 1975; Allen and Penston, 1975; Pipher et al., 1976; Aspin et al., 1990). It was classified by Eiroa et al. (1979) as a late O/early B star, based on the NIR spectra, the colours and the total luminosity.

Richer et al. (1993) discovered in CS $J = 3 \rightarrow 2$ and C^{18}O $J = 1 \rightarrow 0$ maps a bright far-infrared source located $15''$ east from $\sharp$IRS 4, coinciding with H$_2$O maser emission (Stutzki et al., 1982), suggesting that this extremely embedded object could be a very young proto-stellar companion to $\sharp$IRS 4.

The bipolar morphology of S106 has been explained in terms of three different models (Bally et al., 1998). a) a parsec-scale circumstellar disc, supported by the detection of a large-scale molecular gas torus with different molecular tracers (Stutzki et al., 1982; Bally et al., 1998; Churchwell and Bieging, 1982). Its orientation would be roughly east-west and tilted $15°$ into the plane of the sky . b) A stellar wind of $\sharp$IRS 4 with a latitude dependence (Felli et al., 1984). c) A compact and very dense disc around the central star (P.A.$\sim 1115°$ (Hoare et al., 1994; Hoare and Muxlow, 1996)), whose ionised edge lies inside the surface where the radio continuum emission from the stellar wind becomes optically thick at 22 GHz (Persson et al., 1988).

As explained in Sect. 2.2, NIR polarimetric maps can help to unveil the presence of hidden sources and evidence the presence of circumstellar discs around YSO. A NIR polarimetric map was published by Aspin et al. (1989), with a resolution element of $1.24''/2$ pixel. However, the far-infrared source is located outside the field of view of this map.

Our K$'$ polarimetric map of Fig. 2.10 shows a clear centrosymmetric pattern over most of the nebula (except for the north-west south-east orientation), centred at the location of $\sharp$IRS4, consistent too with the MSX and IRAS sources. The black ellipse indicates the 1σ error ellipse in the location of the illuminating source of the entire nebula, following the Weintraub's method. The elongation of the polarised intensity towards the south seems to have polarisation vectors rotated by 90 degrees with respect to the general pattern, but the map does not appear disturbed in the area where the secondary companion, proposed by Richer et al. (1993), is located (approximately $5''$ away from one of the most highly ionised regions). I conclude that this secondary far-infrared source is not a strong illuminating source of the reflection nebula.

Despite the angular resolution of the K$'$-polarimetric map is the highest to date, the closest polarisation vectors to $\sharp$IRS4 must be considered with caution. The PSF variations due to the atmospheric aberrations and the spikes of the PSF can affect significantly the orientation of the polarisation vectors. Hence, this study concentrates on the detection of a large-scale disc. Moreover, a profile analysis of $\sharp$IRS 4 in the K$'$-band by Feldt et al. (2002) shows that
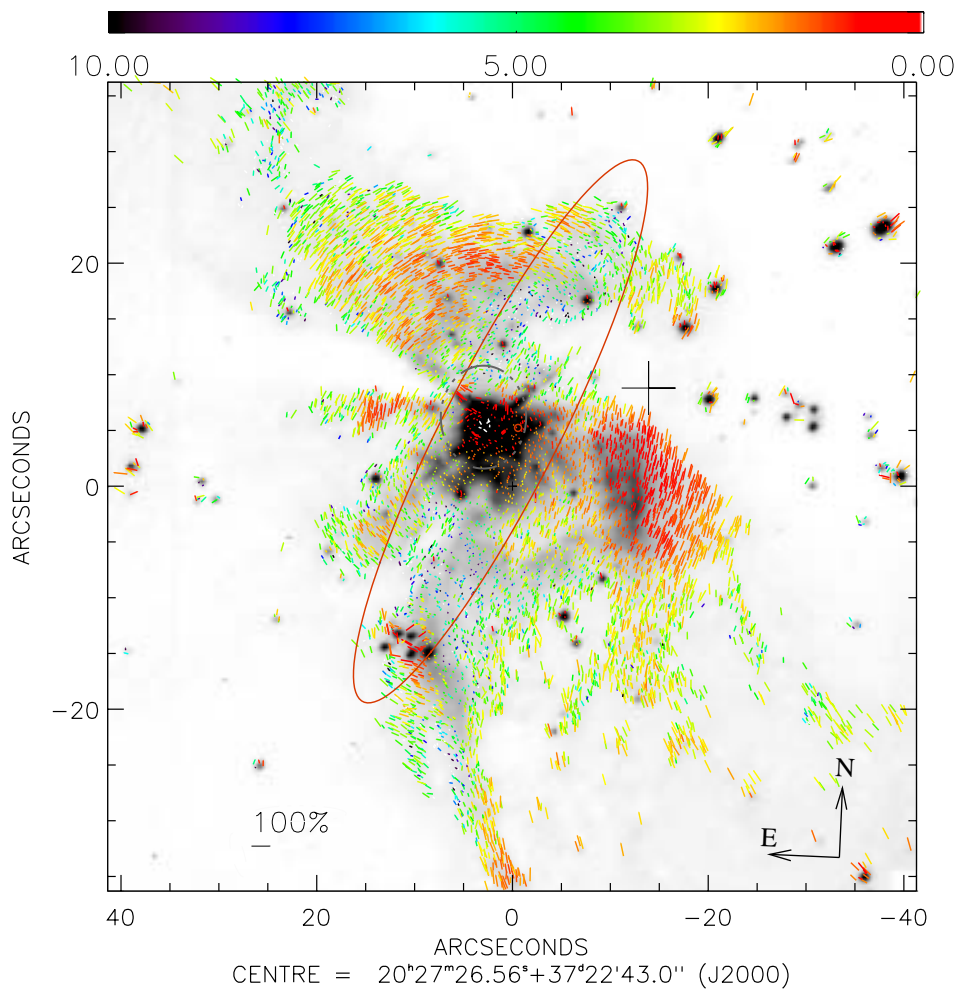
Figure 2.10: K′ polarimetric map of S106 with a FWHM=0.5″. The polarisation vectors shown correspond to intensities over the 3σ level and have been displayed one every 30 for the sake of clarity. The colourbar indicates the error in degrees on the orientation of the polarisation vectors. The black cross is located at the position of the H_2O maser and the 450 μm source (Richer et al., 1993). The 1σ estimated location of the illuminating source is represente by the black-dotted-line ellipse. The red ellipse indicate the IRAS point source while the circle indicates the MSX source.

no extension is detected towards the parallel and perpendicular direction formerly proposed (Hoare et al., 1994). This study is limited to the region within 0″17 (100 AU) to the central star. Fig. 2.10 does not show a systematic alignment of vectors, parallel to the expected orientation of the disc, although the extended emission does not extend far away from ♯IRS 4. This could be also interpreted as a consequence of foreground extinction or an optically thick region that depolarises the signal. However, the non-detection of this feature is compatible with the absence of such structure or the presence of a nearly edge-on circumstellar molecular disc.
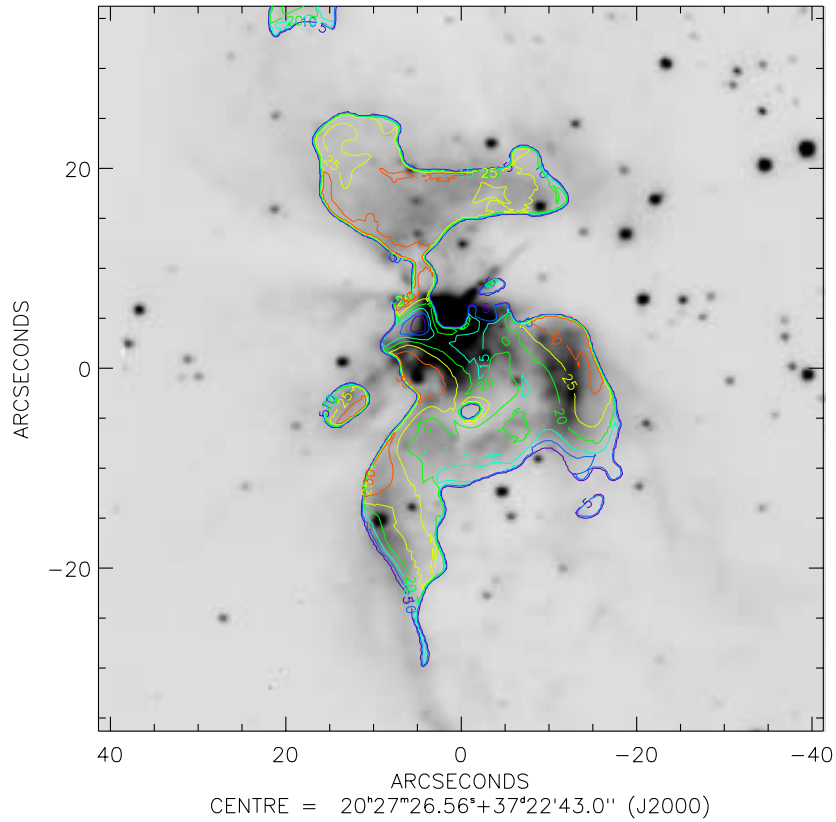
Figure 2.11: The greyscale corresponds to K′ image at spatial resolution 0.′′6, ranging between 5.4 mJy/□′′(light) and 7 mJy/□′′ (dark). Overlaying contours show the visual extinction in magnitudes.

Figure 2.11 shows the visual extinction map calculated for S106. This map has been obtained by comparing the observed Brγ-line emission of this region with that predicted from the scanned 1.3 cm VLA radio continuum map (Felli et al., 1984), following the procedure described by Feldt et al. (1998). The Brγ map has a total exposure time of 900 s. A K′ image was used to subtract the continuum, after rescaling to the bandwidth and transmissivity of the Brγ filter. Flux calibration was achieved through the interpolation of the J, H and K′ magnitudes of several stars in the field. The map presents visual extinctions up to values of 35 magnitudes. The regions of highest extinction correlate fairly well with the areas of polarised signal around 35%.

2.7   Application II: G77.96-0.01

This UCHII, located at a distance of 4.2 kpc, was initially catalogued at radio wavelengths (2 cm and 3.6 cm) as an irregular UCHII region (Kurtz et al., 1994). Subsequent studies at longer wavelengths and more compact configurations of the radio antenna, revealed a very extended emission, likely associated with the UCHII (Kurtz et al., 1999), that is presented in Fig. 2.14. The secondary peak of emission, located around $1'$ to the west, was also detected by Zoonematkermani et al. (1990) in the 21 cm line. Kurtz et al. (1999) consider the UCHII to be likely connected to the extended emission.

K-band spectra of five point-like objects whithin this region was presented in Hanson et al. (2002a), with poor spatial resolution, confirming that $\sharp 23$ is a foreground star. The first NIR images of the possible ionising sources extend ofver a small field of $40'' \times 40''$ (Alvarez et al., 2004) around G77.96-0.01, show a quite extended reflection nebula (see Fig. 2.12) and resolve the region of radio continuum emission into three sources, $\sharp 11$ being the most reddened source in the field ($A_V > 20$ mag). This star, located at the radio peak (see Fig. 2.13), is a good candidate to ionise the region. There exists no determination of its spectral type by means of photometry since it is only detectable in the K$'$ band, and only nebular lines are present in the spectra of Hanson et al. (2002a). The classification of the nearby sources through the colour-magnitude and colour-colour diagrams show three other stars ($\sharp 9, \sharp 7, \sharp 45$) with determined spectral types of late O/early B stars that could be contributing to the ionisation of the UCHII (Alvarez et al., 2004).

The K-band polarimetric map of G77.96-0.01 is displayed in Fig. 2.13, together with the contours corresponding to the 2 cm VLA map (Kurtz et al., 1994) in B configuration and the 3.6 cm VLA map in D configuration. The polarisation vectors are describing a partially centrosymmetric pattern in the north-west area, close to the $\sharp 11$ source. The illuminating source is estimated to be within the black ellipse, namely source $\sharp 11$. This radiation is then polarised by dust in an optically thin region while the absence of polarisation to the south of the UCHII indicates that the emission in K band toward this area is produced either by ionised gas emitting in the Brγ line, also indicating that no dust (scatterer) is present in this area. Despite polarisation vectors with acceptable SNR are also present to the south-east of the reflection nebula (i.e. near $\sharp 45$), no centrosymmetric pattern appears centred at the location of $\sharp 45$. This feature points to a scenario where multiple illuminators (at least $\sharp 11$ and $\sharp 45$) are responsible of the reflection nebula.

The fact that there exists polarised signal over most of the reflection nebula and this extends further than the UCHII region, coinciding with the extended radio continuum emission, could be an indication that the extended halo is not only linked to the UCHII region, but also possibly to several ionising stars, translating in a complex morphology. To confirm this link, near infrared recombination line images would be very useful. This represents a very interesting result because it illustrates the fact that the classification of ionised regions as ultra-compact suffers from the a bias introduced by the radio techniques. At radio wavelengths, the configuration of the antennas favours the detection of certain frequencies that could mimic the complex ionised regions with knots of high emission into ultra-compact HII regions.
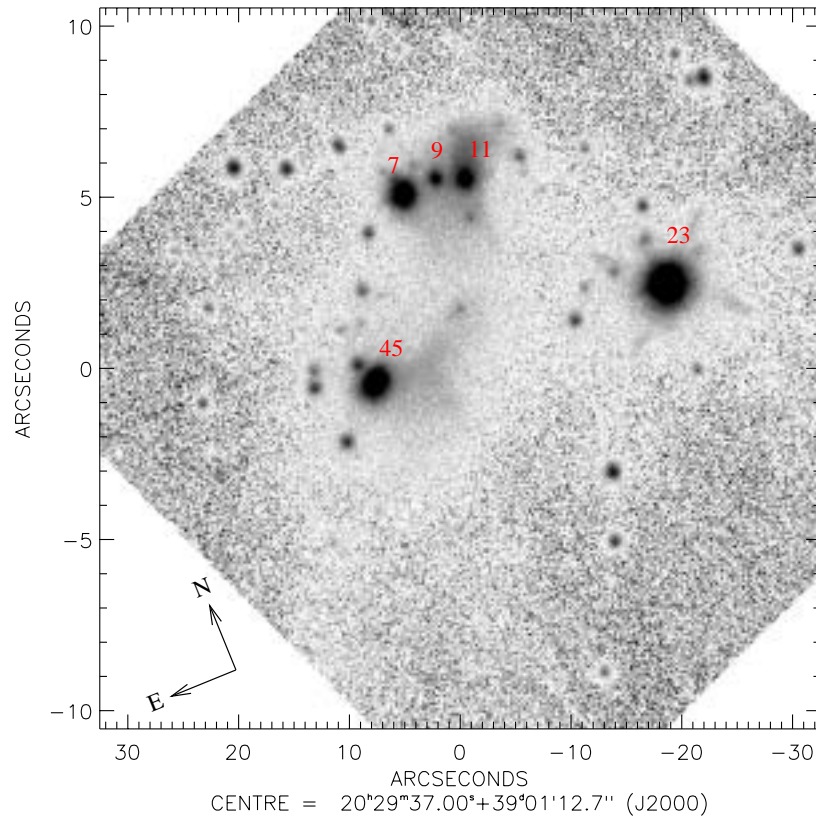
Figure 2.12: K′+wire grid at 45° image of G77.96-0.01 in arbitrary units. The spatial resolution is 0.″4. The red numbers indicate the detected sources following the nomenclature of Alvarez et al. (2004).

2.8   Conclusions

NIR polarimetric maps constitute a useful tool that helps analysing the detected stellar content of massive-star-forming regions, locating the main illuminating source of the reflection nebula and pinpointing the presence of bright source(s) that are undetected due to the high extinction present in these regions. NIR polarisation maps of two massive star forming regions have been analysed: S106 and G77.96-0.01. The far-infrared source detected by Richer et al. (1993) in the surroundings of the presumably ionising source of the bipolar nebula S106 is confirmed no to be significantly contributing to the illumination of the nebula. On the other hand, the polarimetric map does not indicate the presence of a parsec-scale circumstellar disc, proposed to be one of the possible scenarios to explain the bipolarity of this object. In the case of G77.96-0.01, on of the main illuminating sources has been confirmed to be ♯11 in the northern part of the reflection nebula. The presence of polarised signal over a larger area of the reflection nebula indicates that the UCHii region is possibly illuminated by the southern
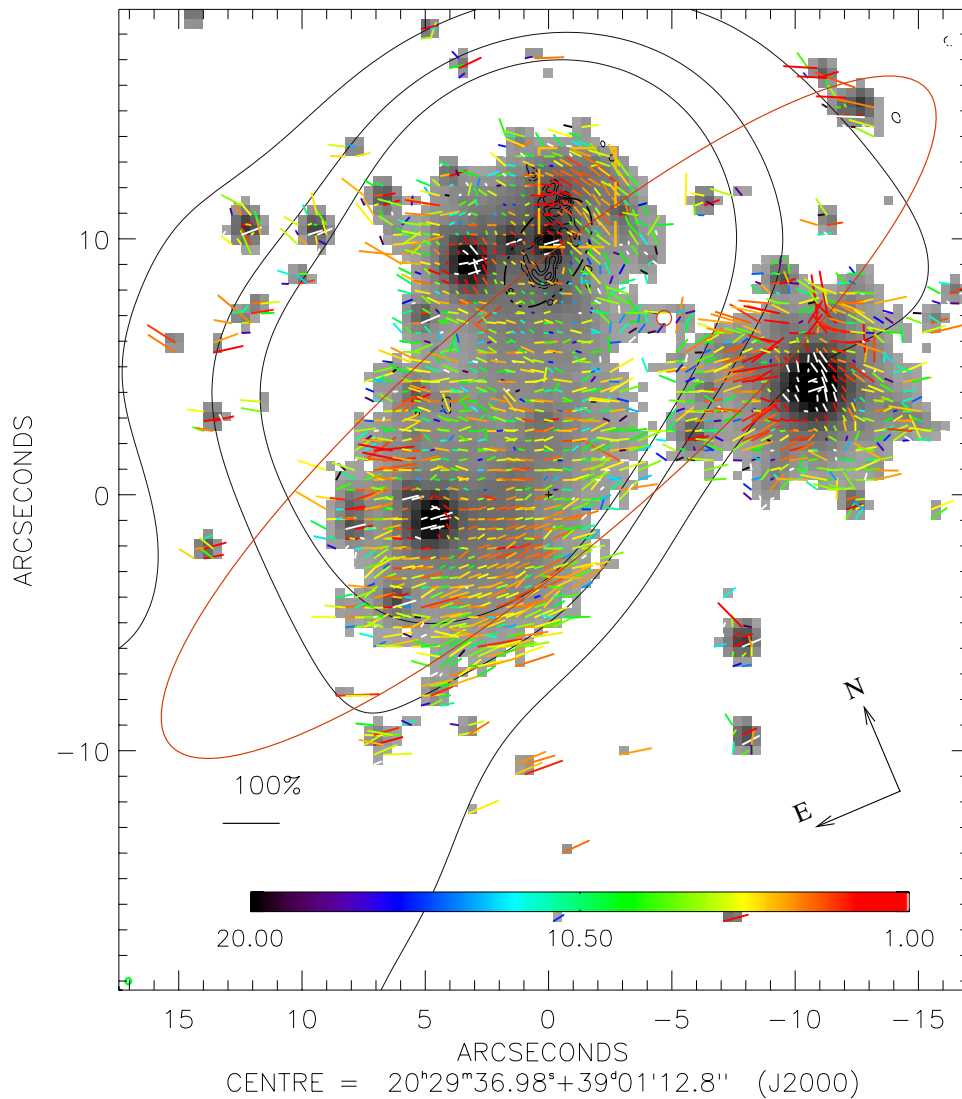
Figure 2.13: K′-polarisation map of G77.96-0.01 with ALFA. The original images have been rebinned with a box of 10×10 pixels. Weintraub's method was applied to the vectors inside the orange discontinuous box, resulting in an estimate of the location of the dominant illuminating source, represented by the black discontinuous ellipse. The black contours at the location of the star ♯11 are the VLA 2cm emission from (Wood and Churchwell, 1989). The black contours in the larger scale correspond to the same levels represented in Fig. 2.14. The red circle and ellipse depict the location of the MSX and IRAS sources, respectively.

star ♯45, and therefore linked to the extended halo detected by Kurtz et al. (1999).
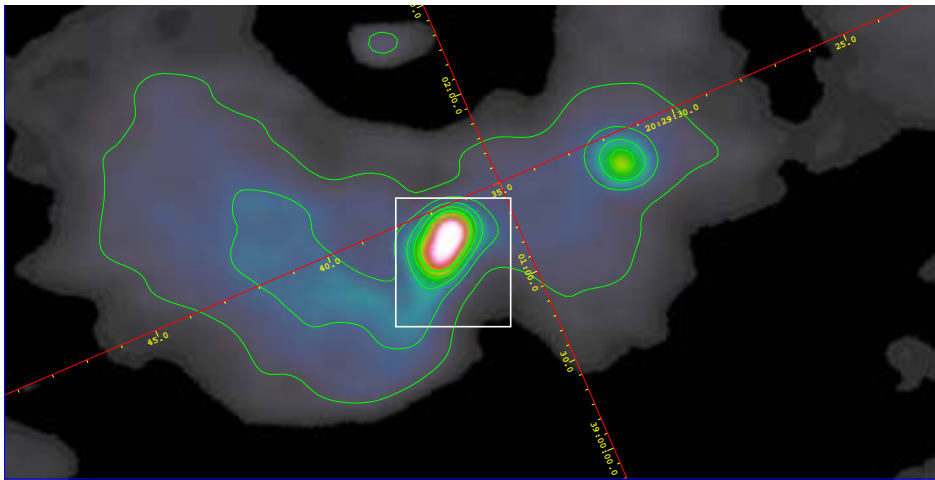
Figure 2.14: VLA 3.6 cm image of G77.96-0.01 in D configuration with contour levels 2.2, 9, 16, 23, 30 31 mJy/beam, kindly provided by S. Kurtz and published in Kurtz et al. (1999). The overlaying white box represents the field of the polarimetric map.

Chapter 3

AO-assisted Observations of G61.48+0.09

3.1 Introduction

The characterisation of the stellar populations of ultra-compact HII (UCHII) regions is one of the key means of understanding the formation and evolution of massive stars. Adaptive Optics (AO) assisted near-infrared (NIR) observations provide sufficient resolution, sensitivity and contrast to detect such populations at moderate extinction values. NIR high-resolution observations of G61.48+0.09 are presented, a morphologically complex UCHII region with two components, whose accessible stellar content in the NIR has been widely studied before. Broad- and narrow-band NIR imaging provides an accurate determination of the morphology of the reflection nebula and the ionised material at subarcsecond resolution. The comparison of images obtained in the hydrogen recombination lines with radio-continuum maps can be used to constrain the extinction produced by the foreground material.
NIR polarimetry provides additional information, pinpointing stars hidden by dust in the molecular cloud. If the cloud is optically thin, single scattering will dominate, producing a centrosymmetric pattern of the polarisation vectors centred at the illuminating source (Weintraub & Kastner, 1993; Weintraub et al., 1994, Henning & Stecklum, 2002).

In this chapter, high-resolution polarimetric and photometric observations are used to investigate in detail the UCHII region G61.48+0.09. The relatively small distance (2.5 kpc adopted; Goetz et al., 1999; Deharveng et al., 2000), as well as the high quality of the existing radio continuum maps, combined with the high spatial resolution achieved in NIR imaging make this source an excellent object for pushing further the limits of current knowledge of the stellar content and the physical properties of the surrounding material in UCHIIs.

3.2 The G61.48+0.09 region

G61.48+0.09 is a complex of two UCHII regions (G61.48+0.09A and G61.48+0.09B), located in the emission nebula Sh2-88B. They were first identified on the red print of the Palomar Sky Survey and studied in the radio continuum by Felli & Harten (1981). In the same paper, G61.48+0.09B was catalogued as a complex object with two ionised components B1 and B2, with B1 dominant in terms of radio flux (Fig. 3.1). The component B2 is located to the east

and has been classified as a spherical or unresolved UCHɪɪ region which subtends an angular size of $\sim3.''5$ on the sky (i.e. 0.04 pc at 2.5 kpc), whereas B1 is an extended cometary region ($\sim14''$, i.e. 0.17 pc) that is thought to undergo a champagne flow (Garay et al., 1994, 1998a and 1998b). Note that Wood & Churchwell (1989)(hereafter WC89) denoted the B2 peak of Garay et al. (1993) as G61.48+0.09A. Figure 79 in WC89 does not show the peak associated with the B1 component. However, it is present in the full-size 6 cm image that was obtained from the on-line version of the paper. Figure 80 in WC89 shows another peak of compact emission (G61.48+0.09B) which is located at the south-western edge of B1 (see Fig. 3.1).

The analysis of the velocity structure of CO lines in Sh2-88B showed the presence of molecular gas in the region and its association with the Hɪɪ region (Schwartz, Wilson & Epstein, 1973; Blair, Peters & Vanden Bout, 1975). The CO data reveal higher densities at the locations of the B1 and B2 components, explaining why no NIR counterparts are detected. The density decreases dramatically at the border of the detected Hα nebulosity (Deharveng & Maucherat, 1978). A molecular outflow was also identified (Phillips & Mampaso, 1991) and confirmed later by White & Fridlund (1992). However, these last authors admit the possibility of more than one outflow within the molecular cloud, thus explaining its complexity and the presence of substructures.

The first NIR study of G61.48+0.09 was performed by Evans et al. (1981) with a resolution of $16''$. Later, the 2.2 μm emission peak was resolved into a *trapezium system* of three stars (Deharveng et al., 2000). However, only part of the region traced by the radio-continuum emission and associated to the component B1 is visible at NIR wavelengths. The ionising source of this UCHɪɪ region was identified as star 82, the most eastern star within the trapezium, based on the high luminosity shown in the colour-magnitude diagram and its central location with respect to the radio-continuum emission. Deharveng et al. (2000) assigned a spectral type between O8.5V and O9.5V to this star. However, Evans et al. (1981) and Garay et al. (1998a, 1998b) explained the cometary morphology as produced by a champagne flow, the head of which is further east than star 82, near the 6 cm continuum peak.

G61.48+0.09 is associated with a very extended NIR nebula ($\sim30''$; Deharveng et al., 2000) to the south-west, which was partially traced in Hα emission (Deharveng & Maucherat, 1978). The Hα emission from diffuse gas is detected at a relative velocity of ~3 km s^{-1} with respect to the molecular cloud, which favours the presence of a flow. Evans et al. (1981) suggested that the gas traces a cavity in the front face of the molecular cloud.

Some immediate questions arise regarding this complex source. Can sources still embedded in the dense molecular cloud be pinpointed at NIR wavelengths through the scattered light traced by a linear polarisation map in the K$'$ band? Once the spatial distribution of the extinction is known, can I constrain better the photometric information on those stars that are detected in the NIR in order to identify the star or stars that are producing the Hɪɪ region? Is there any emission produced by shocked molecular hydrogen that confirms the existence of an outflow and its direction?

3.3   Observations and Data Reduction

The UCHɪɪ region G61.48+0.09 was observed during the nights of November 11 and 12, 2000, using the Adaptive Optics system ALFA (Kasper et al., 2000) with the NIR camera Omega-Cass (Lenzen et al., 1998a) at the 3.5m telescope on Calar Alto (Almeria, Spain). The reference star used by the AO system for the polarimetric images is located at α_{2000}=19^{h}46^{m}47^s,
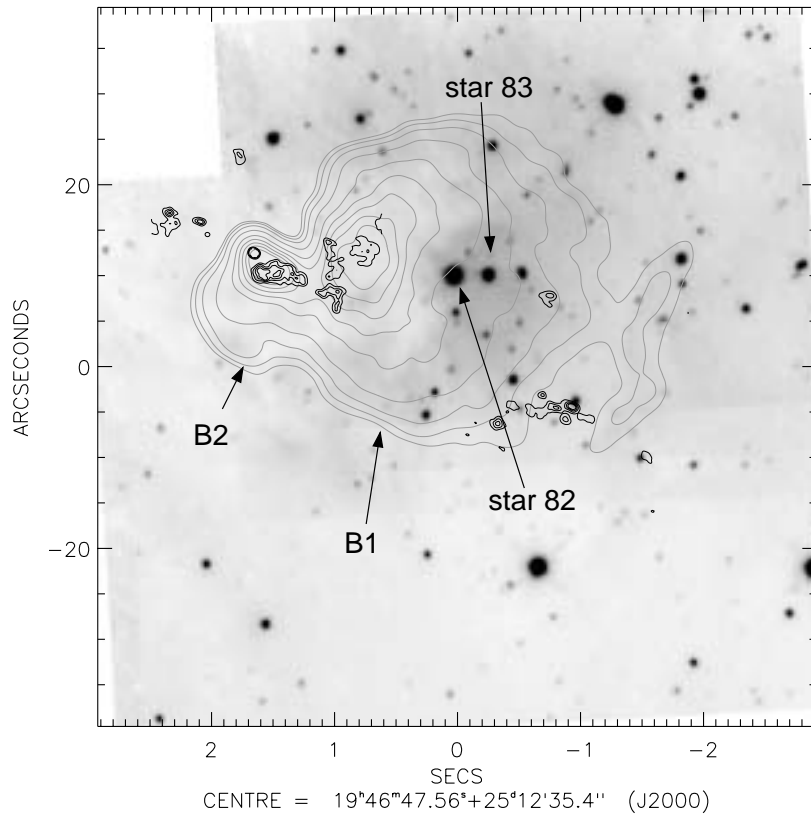
Figure 3.1: K′-band image of G61.48+0.09B on a logarithmic scale (between 35 mJy/□″ and 40 mJy/□″), obtained using the AO system ALFA (Alvarez et al., 2004, in preparation.). The grey contours correspond to the 6 cm continuum emission with a resolution of 3″ obtained with the VLA in C configuration (kindly provided by G. Garay). Contours are at flux values of 5, 8, 13, 25, 51, 76, 102, 127 and 152 mJy/beam. The lowest contour corresponds to a 20σ detection. The black contours indicate the 6 cm continuum emission with VLA in A configuration with a resolution of 0.″4 (WC89), highlighting the peaks in the emission. Contours are at 0.2, 1.6, 3.0, 4.4, 5.8 and 7.2 mJy/beam. The lowest contour corresponds to 1σ. Star 82 and star 83 follow the notation of Deharveng et al. (2000).

$\delta_{2000}{=}+25°12′13″$ (see Table 1). For the narrow-band images two reference stars were used ($\alpha_{2000}{=}19^h46^m47^s$, $\delta_{2000}{=}+25°12′13″$, $\alpha_{2000}{=}19^h46^m46^s$, $\delta_{2000}{=}+25°13′04″$), averaging after the two image sets. The pixelscale is 0.″08/pixel. Polarimetric images were obtained with the K′-band filter ($\lambda{=}2.118~\mu$m, $\Delta\lambda{=}0.35~\mu$m), whereas imaging of the Brγ and H$_2$(1–0)S1 emission was performed with the NB2.166 ($\Delta\lambda{=}23.2$ nm) and the NB2.122 ($\Delta\lambda{=}22.8$ nm) filters, respectively.

AO-assisted L′-band images ($\lambda{=}3.8~\mu$m, $\Delta\lambda{=}0.62~\mu$m) were obtained on June 12th, 2003 at the VLT/UT4 with the L27 camera of NAOS/CONICA (Rousset et al., 2000; Lenzen et al., 1998b). For these observations, star 82 served as the reference of the NIR-wavefront sensor,

using the N80C20-dichroic. The total exposure times and spatial resolutions achieved are summarised in Table 1.

3.3.1 Polarimetric observations: K′

Besides the NIR imaging and spectroscopy modes, a polarimetric facility is available for ALFA/Omega-Cass. The polariser consists of four wire-grids oriented in four different directions ($0°$, $45°$, $90°$ and $135°$) with transmission efficiencies of 87%, 97% and 90%, relative to the $45°$ wire-grid.

For every polariser, 5 exposures of 120 s integration time were obtained with slight offsets between them, in order to construct a sky image for each single orientation. For flat-fielding, sky subtraction and bad-pixel flagging, via the *variation method* (Ageorges & Walsh, 1999) with dome flats, the standard IR reduction techniques were followed. After registration of the four images with IRAF[1], spatial binning with a 4×4 box was necessary to increase the signal-to-noise ratio (SNR). The Stokes parameters are derived from the differences between the intensities of the four orientations, and determined the polarisation degree and angle of the polarisation vectors (Serkowski, 1962). Debiasing of the polarisation degree through the Wardle and Kronberg estimator accounts for the fact that the noise produces a bias in the estimate of the polarisation degree (p)(Serkowski, 1958; Simmons & Stewart, 1985). The error in the polarisation degree (σ_p) was determined by the Gaussian propagation of the sky error (dominant in the NIR images with long exposure times) for signal-to-noise values higher than 6. For smaller SNRs, the 1σ-confidence interval calculation (Simmons & Stewart 1985) was applied. The error in the position angle was calculated using the expression $\sigma_\theta = 28.648(\sigma_p/p)$ when $p/\sigma_p > 6$ (Serkowski, 1962). The expression from the error distribution of σ_θ that appears in Naghizadeh-Khouei & Clarke (1993) was used for $p/\sigma_p < 6$.

Calibration of the instrumental polarisation is performed by using the intensities of 17 field stars within the images and assuming them to be – at least on average – unpolarised. Observations of the polarised standard star HD 38563C, from the Whittet et al. (1992) catalogue, were used to correct the zero point of the polarisation angle and the average polarisation efficiency.

3.3.2 Narrow-band imaging: Brγ and H$_2$

In an analogous way, narrow-band images of the Brγ and H$_2$ emission were obtained in 5 offset positions with integration times of 150 s in every filter, for two sets of images. A different reference star was used for each of them (Table 1). No narrow-band images of the adjacent continuum were taken for calibration. The flux in the K′-band image was scaled to the width of the narrow-band filters, assuming that the bulk of the emission is continuum. The scaled continuum image was subtracted from the H$_2$ image, showing the absence of line emission. Therefore the H$_2$ image was utilised as continuum for subtraction of the Brγ image. Since no photometric standard was observed, J-, H- and K′-calibrated-aperture photometry on 5 stars in the field was used to interpolate and calibrate the flux density of the final Brγ and H$_2$ images.

---

[1]IRAF is distributed by the National Optical Astronomy Observatories, which is operated by the Association of Universities for Research in Astronomy, Inc. (AURA) under cooperative agreement with the National Science Foundation.

Filter	IT[a]	FWHM[b]	Reference star	mag/band
	(s)	($''$)		
K$'$ +wire − grid	120×5	0.6	GSC02114300957	12.96/V
Brγ	150×5	0.5	GSC02114300957,GSC02114300691	12.88,12.96/V
H_2	150×5	0.5	GSC02114300957,GSC02114300691	12.88,12.96/V
L$'$	29	0.13	star 82	9.4/K$_s$

Table 3.1: Observational data[a] Integration time.[b] Spatial resolution at the reference star.

3.3.3   Broad-band imaging: L$'$

L$'$-band images with NAOS/CONICA at the VLT were obtained with the chopping-nodding technique in order to correct for the thermal background noise. However, technical problems only allowed chopping with a throw of $20''$ and a total integration time of 29 s. This results in a sub-optimal subtraction of the background, limiting the study to point-like sources, and does not allow us to investigate any extended emission in the L$'$-wavelength range. Flux calibration was performed by observing the standard star HD106965 with the same optical set-up, but jittering over the field in order to construct a median-sky.

3.4   Results and Discussion

3.4.1   The illuminating source

Figure 3.3 shows the complex polarimetric map of G61.48+0.09 in the K$'$ band. Polarised light is present across the entire extension of the nebula; but only vectors with polarisation degrees between 10% and 80% are depicted to exclude depolarisation produced by multiple scattering and noise in very faint regions, respectively. The polarisation degree grows toward the edges of the nebula, attaining values of up to 35%. In such cases, the polarisation induced by the interstellar medium is negligible ($\sim$2%, c.f. Ageorges & Walsh, 1999). The presence of several stars in the region of nebular emission limits the area where information about the illuminating sources can be extracted. To determine the location of the illuminating source, I apply the method proposed by Weintraub et al. (1993), which calculates the intersection of the perpendicular to every pair of vectors, over arbitrarily selected areas. These areas must show an increasing polarisation degree with the distance to the presumed illuminating source. The average of these positions, using the signal-to-noise ratio of the polarisation angle as weighting factor, produces an estimate for the source position, including a certain error. I focus this analysis of this polarisation map on different areas around the two UCHII regions. (1) The two knots of emission (knot 1 and knot 2 in Fig. 3.3a), located at $\alpha_{2000}=19^h46^m49^s.3$, $\delta_{2000}=+25°12'36''$ and $\alpha_{2000}=19^h46^m49^s.0$, $\delta_{2000}=+25°12'26''$ respectively, exhibit a partially centrosymetric pattern. This pattern is compatible with the centre being at the location of the B2 component. Both regions show a high degree of polarisation and a good signal-to-noise ratio. Fig. 3.3a shows the positional error ellipse within a 99% certainty limit, using only the vectors in knot 1.

In Fig. 3.3b, also the vectors in knot 2 are considered. In both cases, the location of the illuminating source is consistent with the position of the B2 component traced by the 6 cm map. Thus, I conclude that the B2 component is internally illuminated. Fig. 3.2 shows
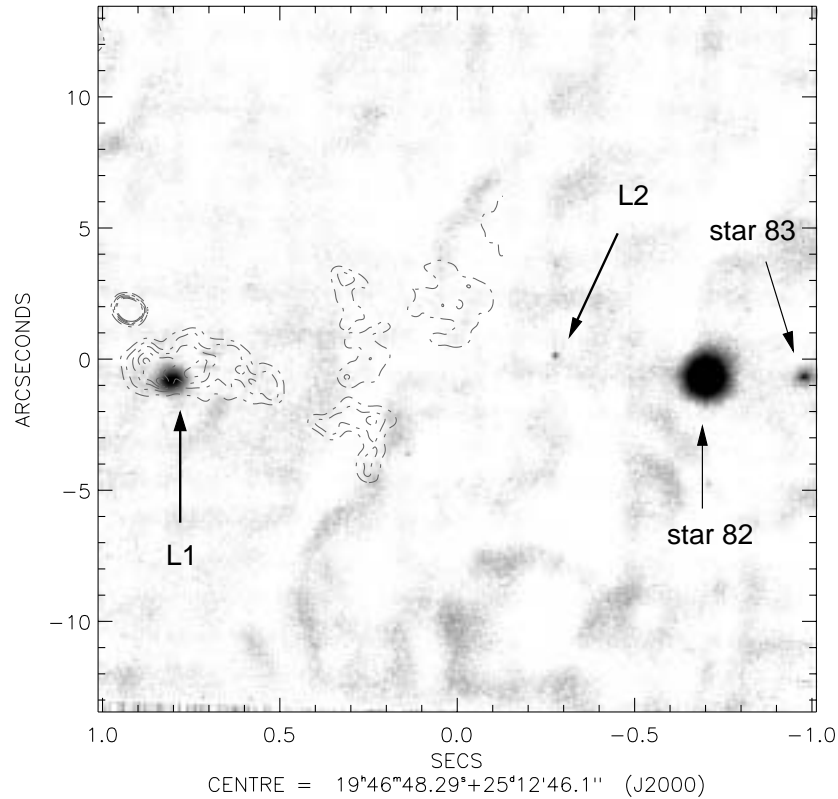
Figure 3.2: L′-band image with NACO at the VLT. The grey-scale varies from 0.07 Jy/□″ (white) to 0.2 Jy/□″ (dark). Two stars not detected in the J, H and K′ band are now located above the 3σ threshold (L1 and L2). The grey-dashed contours correspond to the 6cm VLA map (Wood & Churchwell 1989).

the L′-band image in which two new sources (L1 and L2), not present in the J-,H- and K′-band images, are detected with brightnesses of $m_{L'}$=8.0±0.1 mag and $m_{L'}$=11.5±0.1 mag, respectively. As seen in the figure, the position of source L1 coincides with the peak of the radio map at the location of B2, confirming the former polarimetric results.

(2) The polarisation map around the location of the B1 component is very complex, i.e. there are many possible illuminating sources. In addition, the extinction produced by the molecular cloud is very high, leading to strong depolarisation. Most of the polarisation is concentrated at the edges of the molecular cloud (see Deharveng et al., 2000, for a comparison with the CO emission). Due to the absence of a global centrosymmetric pattern, I focus on the local analysis of the map and the comparison with the different hypotheses related to the possible stellar population. The first possibility is that the most luminous star at NIR wavelengths (star 82) is the main illuminating source, which was also proposed by Deharveng et al. (2000) to ionise the region. However, the northern rim of the nebula, close to this star and where the signal-to-noise ratio is higher, shows no evidence of a dominant illumination coming from star 82. The second possibility is that, as was shown in the case of the B2 component, other

undetected stars remain hidden to the observer at shorter wavelengths but still illuminate the nebula. No star is detected in the NIR images at the position of the B1 radio continuum peak, due to the high extinction. An MSX source is located $\sim 3''$ to the south-west of the radio peak, coinciding with the tail of the arc. Note that even though the resolution of the MSX catalogue is low, the accuracy in the source position is high ($\sim 2''$). Hence, it is likely that hidden stellar sources may be located near the MSX source or near the peak shown by the radio maps, just like in the case of G29.96-0.02 (Pratap, Megeath & Bergin, 1999). To test this, areas with vectors perpendicular to the radio peak were selected (squared areas in Fig. 3.3c). The resulting position ellipse is displaced from this source, but also close to the position of the MSX source, and includes the location of L2. Alltogether, there is no evidence of star 82 being the main illuminating source of the nebula but most likely other embedded objects, such as L2, might contribute significantly to the illumination.

3.4.2 Brγ emission and extinction

The Brγ map is shown in Fig. 3.4. The estimate of the Brγ-line emission within a circular aperture of $17''$ diameter, centered at $\alpha_{2000}=19^h46^m47^s.1$ and $\delta_{2000}=+25°12'43''$, yields a flux density of 0.15 ± 0.08 Jy. The quoted error results from the propagation of the error in the flux calibration and the error in the aperture photometry. This flux density is consistent with the 0.16 ± 0.02 Jy estimated by Goetz et al. (1999), within the same aperture, with poorer spatial resolution.
The Brγ emission around the B2 component is very faint and coincides with knot 1 (see Fig. 3.4). The bulk of the Brγ emission traces the south-west quadrant of the radio continuum map for component B1, at the same location as the reflection nebula. Hα emission is also present in the same direction (Deharverg et al., 2000). Both features are consistent with the low density inferred from the CO map of this region (White and Fridlund, 1992).

Star 82 is the only stellar source clearly visible as a point source in the continuum-subtracted Brγ image (see Fig. 3.4). This feature is also detected in a K-band spectrum presented in Chapter 4. The rest of the stars in the field are well cancelled by the subtraction of the continuum. The FWHM of the point-like source ($0''.5$) is of the same order as in the unsubtracted image (i.e. unresolved), and hence originates within a region of ~ 1200 AU around the star. The Brγ flux density integrated over an aperture of radius $1''$, centered at the position of star 82 was 15 ± 8 mJy (i.e. 0.01 magnitudes in Ks, after the colour-correction derived from Alvarez et al. (2004), submitted).
The extinction map toward G61.48+0.09 (Fig. 3.5) was obtained by comparing the expected Brγ flux, derived from the 6 cm radio map obtained by G. Garay with the Brγ image, once the remaining emission at star 82 was subtracted with the IRAF package DAOPHOT. The visual extinction map was obtained after convolving the Brγ data to the resolution of the radio image ($\sim 3''$) in the same way as explained in Feldt et al. (1998), using the relation $A_V=9.29A_K$ (Mathis 1990). The dominant error source is the calibration of the Brγ flux, and the estimated error is approximately 2 visual magnitudes.
The map obtained with the same procedure as that used by Goetz et al. (2003) gives visual extinctions between 0 and 30 mag, in good agreement with those presented in this thesis. This estimate of the foreground extinction agrees also with the values derived from the photometry of selected stars (Goetz et al., 1999; Deharveng et al., 2000; Alvarez et al., 2004, ApJ in press). This method estimates the extinction towards the ionised gas, and it must therefore be used
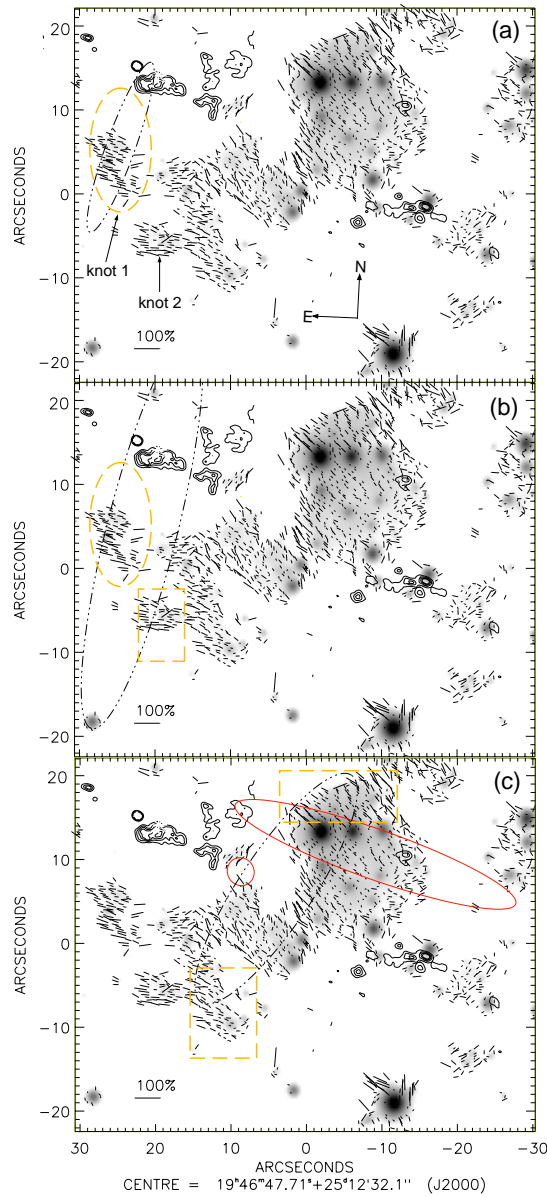
Figure 3.3: K′-band polarisation map of G61.48+0.09. Each of the three panels represents a different estimate of the position of the illuminating source. The black dot-dashed ellipses indicate the region where the illuminating source is located; calculated through Weintraub's method using the polarisation vectors located within the grey-dashed lines. The greyscale indicates the total polarised intensity, masked out according to the constraints of polarisation degree between 10 and 80%. Only one of every four vectors has been represented for clarity. The 100% polarisation vector is represented in the lower left corner of each panel. The grey-solid circle in panel (c) indicates the 1σ-error of the MSX point source position.The grey-solid 1σ-error ellipse represents the IRAS source position. The black contours represent the 6 cm continuum emission from the VLA in A configuration.
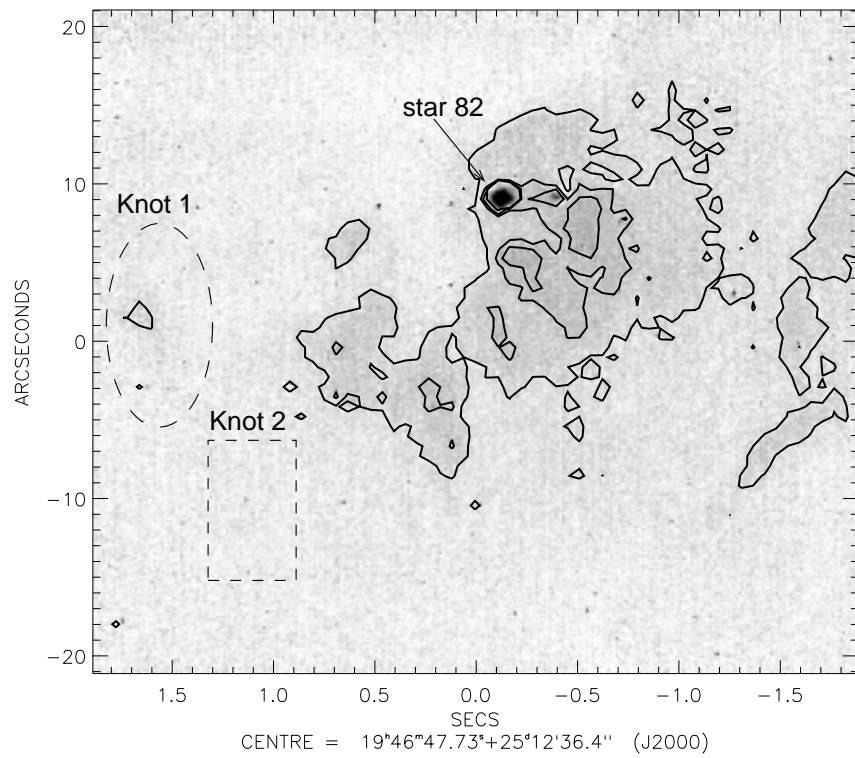
Figure 3.4: Continuum-subtracted Brγ image. Note the point-like remmant with a FWHM of $0.''5$ at the position of star 82. Overlayed contours at 0.3, 0.6, 0.8 and 1.1 mJy/$\square''$.

as an approximation when correcting the stellar fluxes.
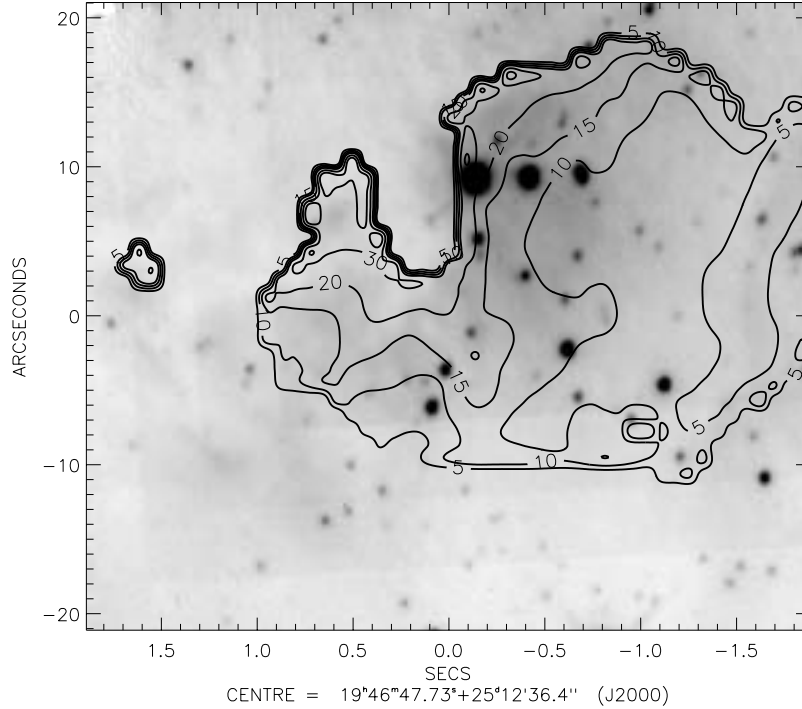
Figure 3.5: Visual extinction map of G61.48+0.09 comparing the calculated Brγ flux from the 6 cm continuum emission provided by G. Garay with the high-resolution Brγ map convolved to the same resolution. The contours are labeled with the extinction values in magnitudes.

3.4.3   The ionising sources

The radio data

Radio continuum observations give an estimate of the spectral type of the dominant ionising star that can be combined with the near IR photometric information to better pinpoint the characteristics of the stellar content of UCHɪɪs.

A number of assumptions need to be made to derive the minimum rate of Lyman continuum photons needed to produce the free-free radiation, probed by the radio continuum data: a) The radio continuum emission is optically thin, b) The ionising source is unique and emits isotropically, c) All the diffuse radiation-field photons are absorbed very close to where they were generated (i. e. the *on-the-spot* approximation or case B recombination), not having any effect on the local ionisation state, d) an ionic abundance of only hydrogen. Under these assumptions, the minimum rate of Lyman continuum photons is estimated with Eq. (1) and (3) of Kurtz et al. (1994). The calculation of the Lyman continuum photons, taking into account the ionic abundances He^+/H^+ by Simpson & Rubin (1990), leads to similar values.

Integrated flux densities for B1 and B2 at 6 cm were derived by Garay et al. (1993), leading to values of 4.36 Jy and 0.83 Jy respectively. They yield the rates of Lyman continuum photons $\log(N_{Lyc})$=48.4 for B1, and $\log(N_{Lyc})$=47.7 for B2. To calculate $\log(N_{Lyc})$ a distance of 2.5 kpc, an electron temperature of 10^4 K, an u_1=0.775 and $a \sim 1$ (Mezger & Henderson, 1966) were used. Comparison of this emission with models of stellar atmospheres yields the spectral type of the ionising star, assuming that the main contribution to the ionisation comes from only one star. According to the models of Vacca et al. (1996), I infer spectral types of O9.5V and B1V or B2V[2] for components B1 and B2, respectively.

In the case of G61.48+0.09B1, where the morphology of the radio map is clearly cometary, there is a possible identification of a central ionising star, given by the NIR data. Observations of the kinematics of the H92α line show that this component of G61.48+0.09 is undergoing a champagne flow (Garay et al. 1994). According to model calculations by Yorke et al. (1983), the Hii region experiencing a champagne flow has an ionisation-bounded side towards the molecular cloud and a density-bounded side in the direction away from the cloud. These correspond to the *head* (peak) and the *tail* of the radio map for B1, respectively (see Fig. 3.1). For this reason, the case B approximation is not fully realistic for these sources, since part of the photons are *escaping* in the directions towards the tail.

The lower limit of the Lyman continuum photon rate is then inferred from the radio emission measured only in a sector of the map in the direction that connects the central star with the maximum of the radio emission. The minimum angle of this sector is given by the resolution element (i.e. the beamsize) at the location of the peak emission. The obtained Lyman continuum photon rate must be divided by the solid angle, as seen by the star, that subtends this projected emission, and rescaled to all directions in order to obtain the total rate of Lyman continuum photons in the Hii region. In the plane of the sky, the angular dimension of this solid angle is equal to the angle of the sector. The angular dimension of the solid angle in the line of sight must be assumed. Three possibilities are proposed: a) equal to the dimension in the plane of the sky, b) equivalent to the angle subtended by the FWHM of the radio-peak continuum emission, c) all possible angles (i. e. 180°). Thus, the rescaling factors are $\frac{4\pi}{\Phi_B^2}$, $\frac{4\pi}{\Phi_B \cdot \Phi_{FWHM}}$ and $\frac{2\pi}{\Phi_B}$, respectively (see Appendix). The beamsize (3″05) subtends an angle $\Phi_B = 20°$ from the central star (α_{2000}=19^{h}46^{m}47^s.6, δ_{2000}=+25°12′45″6), while the FWHM subtends an angle of $\Phi_{FWHM} = 80°$.

The rate of Lyman continuum photons inferred from the initial circular sector is N_Φ=3×10^{47} phot s^{-1}. After rescaling it for each of the three geometrical assumptions, the $\log(N_{Lyc})$ results into 49.5, 48.9 and 48.7 for cases a), b) and c), respectively. Hence, the corresponding spectral types of the central star, inferred from the stellar models, are those of a O5, O8.5 and O8V star, respectively. Since there is no further information of the structure in the direction of the line of sight, I will consider this range of spectral types (varying over 3.5 spectral subclasses) as the best approximation to the spectral type of the ionising central star of G61.48+0.09B1.

---

[2]For the determination of these spectral types, an extrapolation of the models of Vacca et al. (1996) to spectral types later than B0.5V was used.

Can the NIR stellar content explain the energy budget?

Since L1 and L2 have only been detected at 3.5 μm (detection limits in J, H and K′ band
are 18.6, 18.2 and 16.5 mag, respectively), and there is no information at their location in
the extinction map, no determination of the spectral types of these sources was attempted.
The NIR colours of stars 82 and 83, and their central or close to central position within B1,
indicate that these are two possible stellar candidates for ionising the H$_{II}$ region.
The spectral classification of star 82 is revised (Deharveng et al. 2000), based on the new
determination of the extinction, new high resolution (0″57) photometry in the J, H and K_s
band (Alvarez et al., 2004, ApJ in press) and the photometry here determined in the L′ band.
The apparent magnitudes, m_J=16.1±0.1 mag, m_H=12.2±0.1 mag, m_{Ks}=9.4±0.2 mag were
calculated with DAOPHOT in IRAF, using the 2MASS[3] Point Source Catalogue for flux
calibration (Alvarez et al., 2004, ApJ in press). I have subtracted from the Ks magnitude
0.01 magnitudes associated with the residual Brγ emission (see Sect. 3.4.2). In the L′ band,
a $m_{L′}$=5.4±0.1 mag was determined with aperture photometry, and the error was estimated
by taking into account the uncertainty in the flux calibration. Due to the Brγ emission of
star 82, the value of the extinction (A_V=24±2 mag, see Fig. 3.5) must be considered as
an approximation at this location. Moreover, the PSF subtraction, described in Sect. 3.4.2,
provides a lower limit to this value, since it only accounts for foreground extinction and not
for intrinsic extinction.

In Fig. 3.7, the spectral energy distribution (SED) of star 82 is shown in the J, H, Ks and L′
bands. The observed SED is compared with theoretical SEDs of early type dwarfs (luminosity
class V) and supergiants (luminosity class Ia). I take the absolute magnitudes (M_V) from
Vacca et al. (1996) with spectral types in the range O3–B0 for dwarfs, and in the range O3–
O9 for supergiants. For later spectral types, values from Drilling & Landolt (2000) are used.
The intrinsic colours have been chosen from Wegner (1994), because they describe spectral
types up to O6/O5. Since the observed J magnitude is less likely to be affected by an intrinsic
excess, I utilised the J magnitude and the J–H colour as fitting criteria. Besides, an excess
in the J magnitude due to scattering is discarded because the J image of Deharveng et al.
(2000) shows that absorption clearly dominates at the position of star 82.The latest dwarf
spectral type that reproduces the observed J-band flux of star 82, considering A_V=24±2 mag
(see Fig. 3.5), is a B1V (see Fig. 3.7a). Earlier types with higher extinction values fit better
the SED of star 82. However, even an O3V star (the earliest available) is well below the
observed fluxes at H, Ks and L′ bands. This might be caused by the presence of an excess in
the local extinction (e.g. a disc). Another possibility is that the grain composition near the
star is different from that in the interstellar medium.

Supergiants show stronger fluxes for the same spectral types as dwarfs. In contrast to what
is observed for dwarfs, supergiants grow in luminosity at NIR wavelengths with later spectral
types. Therefore, in the case of star 82, an increase of the extinction favours the B-types. The
J magnitude and the J–H colour is better reproduced by a late B star with A_V=37 mag, but
the range of possible spectral types spreads from O9I (A_V=36 mag) to A0I (A_V=37 mag).

---

[3]This publication makes use of data products from the Two Micron All Sky Survey, which is a joint project
of the University of Massachusetts and the Infrared Processing and Analysis Center/California Institute of
Technology, funded by the National Aeronautics and Space Administration and the National Science Founda-
tion.

Yet the emission of star 82 in the Ks-band starts to be higher than predicted by the stellar models and shows a clear excess at 3.5 μm.

The use of the J-H-K photometry from Deharveng et al. (2000) yields similar results for both luminosity classes. Continuum excesses in the range of 2-10 μm are known to be present in B[e]-supergiants due to circumstellar dust (Zickgraf et al., 1986). The hypothesis that this star is a supergiant is consistent with the Brγ emission detected toward star 82, predicted by the models of spectral evolution of massive stars (Schaerer et al., 1996), which appears to be statistically more frequent among supergiants (Hanson, Conti & Rieke, 1996). Therefore, the data on star 82 is best reproduced by the spectral type of a B or late O supergiant.

Fig. 3.7c and 3.7d show the SED of star 83, compared with the theoretical SEDs of early-type dwarfs and supergiants. I used m_J=13.4$\pm$0.1 mag, m_H=11.8$\pm$0.1 mag, m_{Ks}=10.8$\pm$0.1 mag and $m_{L'}$=9.3$\pm$0.1 mag, which were calculated in the same way as previously described for star 82. The theoretical SEDs were extincted by an A_V=15$\pm$2 mag, derived from the extinction map. From Fig. 3.7d, I discard the possibility that star 83 is a supergiant because they are too luminous to reproduce the observed SED. Models of dwarfs under a visual extinction of 15 mag appear to be more suitable to describe star 83. Since star 83 is located well within the reflection nebulosity (see Fig. 2 in Deharveng et al., 2000), some contribution of scattered light to the J magnitude is expected. Therefore, the H magnitude and the H–Ks colour were the fitting criteria. Fig. 3.7c illustrates that a B0V spectral type can approximately explain the observed colours of star 83.

These estimates of spectral types must be considered with caution, since they are strongly affected by numerous uncertainties: the distance to the object, the method to determine the extinction, the presence of scattered light, etc.

Taking into account the two possible luminosity classes for star 82 estimated above, the combination of the spectral type of star 82 and star 83 amounts a logarithm of the rate of ionising photons in the range 47.0–49.9[4], if star 82 is a dwarf star, and <49.4 if star 82 is a supergiant. The estimate provided by the radio map, discussed in the former section, lies between log(N_{Lyc})=48.7-49.5. These ranges are represented in Fig. 3.6. The estimate that considers star 82 to be a dwarf includes values above the overlapping region, meaning that this star would be enough to produce the entire rate of Lyman continuum photons, derived from the radio continuum map. These early spectral types of dwarfs fit best the SED of star 82. Both models of dwarfs and supergiants show values below the overlapping region.Should the true spectral type of star 82 be contained in one of these best-fit regions, additional ionizing sources would be needed to explain the Lyman continuum photon rate. The best fit in the supergiant model corresponds to this regime. The polarimetric map and the presence of an excess of Brγ support this last hypothesis, indicating that L2 or possible undetected sources are contributing to the ionisation. However, NIR spectroscopy is mandatory to discriminate between these two possible spectral types for star 82 (dwarf/supergiant). If the classification of star 82 as a supergiant is confirmed by further observations, then an age spread might be responsible for the increasing size of the HII regions to the west (B1 component is a compact region), instead of the density gradient of the surrounding material. The use of more recent stellar models of Schaerer et al. (1997) and Smith et al. (2002) leads to a similar conclusion.

---

[4]The contribution of star 83 is considered constant and lower than log(N_{Lyc})=48.2
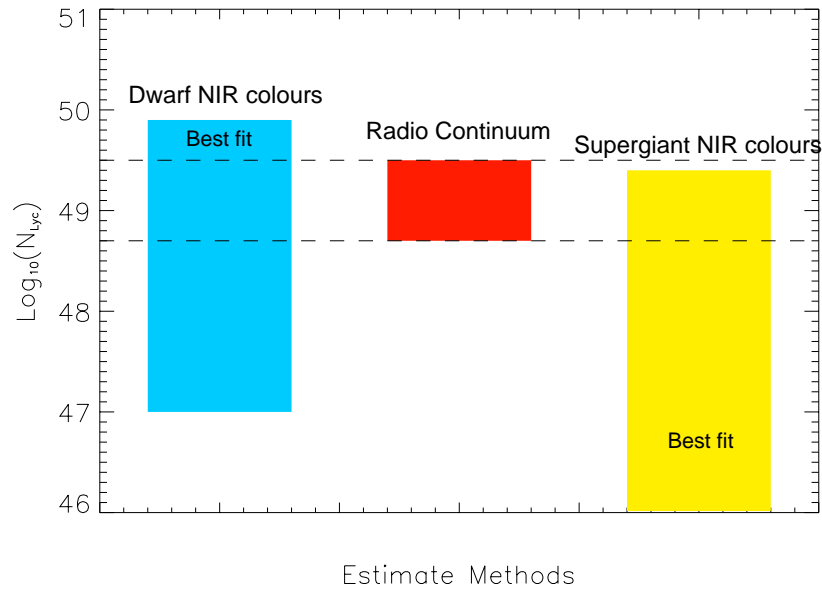
Figure 3.6: Comparison of the Lyman continuum photon rates, estimated through the radio-continuum map, and those modelled by the NIR colours of star 82, considering luminosity classes of dwarfs and supergiants.

Morphology

Figure 3.8 shows the structure of the Brγ-line map, the radio-continuum emission and the scattered light in the nebula. The ionised material, traced by the Brγ contours, is coincident with part of the continuum nebular emission. This common area appears dimmer in the 6 cm map, where the flux density drops faster. The polarised intensity over this area is very small and even negligible in many points. Considering the small extinction, an absence of scatterers can explain this effect.

The lack of Brγ emission over the rest of the B1 UCHII region (toward the north-east) is, very likely, due to the foreground extinction caused by the molecular cloud. The northern rim of the nebula, and, in general, the edges of the molecular cloud show a stronger scattered signal. In general, the Brγ line emission is very faint, but in these regions the extinction rises and the line is no longer detected. Instead, the polarised intensity grows. These regions would correspond to the walls of a cavity opened by a champagne flow, evolving toward the south-west, since no scattering particles are present in the direction toward lower densities of the molecular cloud.
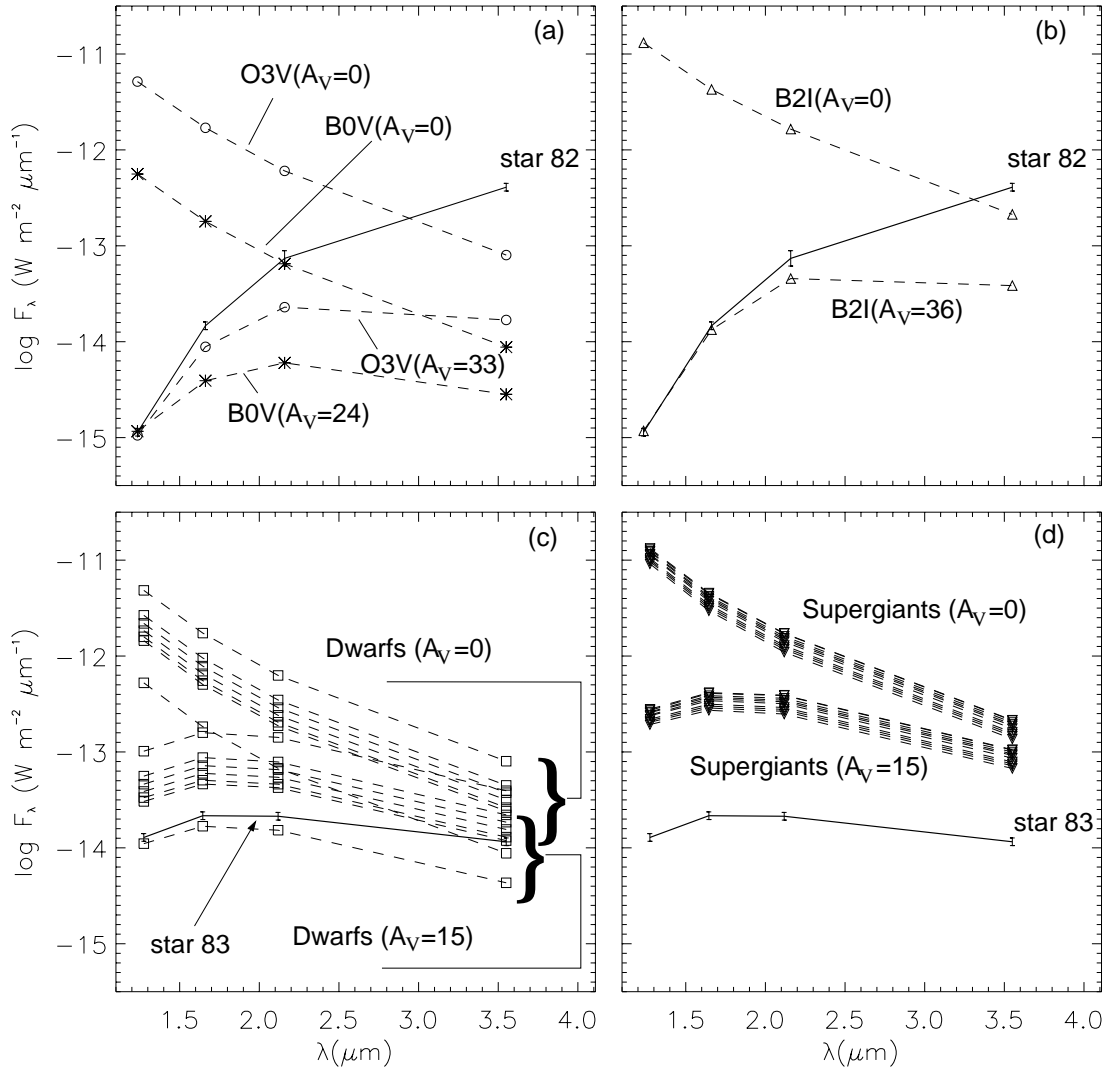
Figure 3.7: Comparison of the spectral energy distributions of star 82 and star 83 with stellar models at different visual extinctions. A distance of 2.5 kpc has been assumed. **a)** Comparison of star 82 with stars of luminosity class V. **b)** Comparison of star 82 with stars of luminosity class I. **c)** Comparison of star 83 with stars of luminosity class V in the range O3-B1. **d)** Comparison of star 83 with stars of luminosity class I in the range O3-B1.

3.4.4 Shocked Molecular Hydrogen–The Outflow

It was expected that the presence of a molecular outflow (Philips & Mampaso, 1991; White & Friedlund, 1992) would be traced in the $H_2(1-0)$ S(1) line. Narrow-band images at 2.12 μm, after subtraction of the continuum, do not show H_2 emission. The detection limit in this image is 3.5×10^{-4} Jy/$\square''$. Therefore, the upper limit for the extinction-corrected line
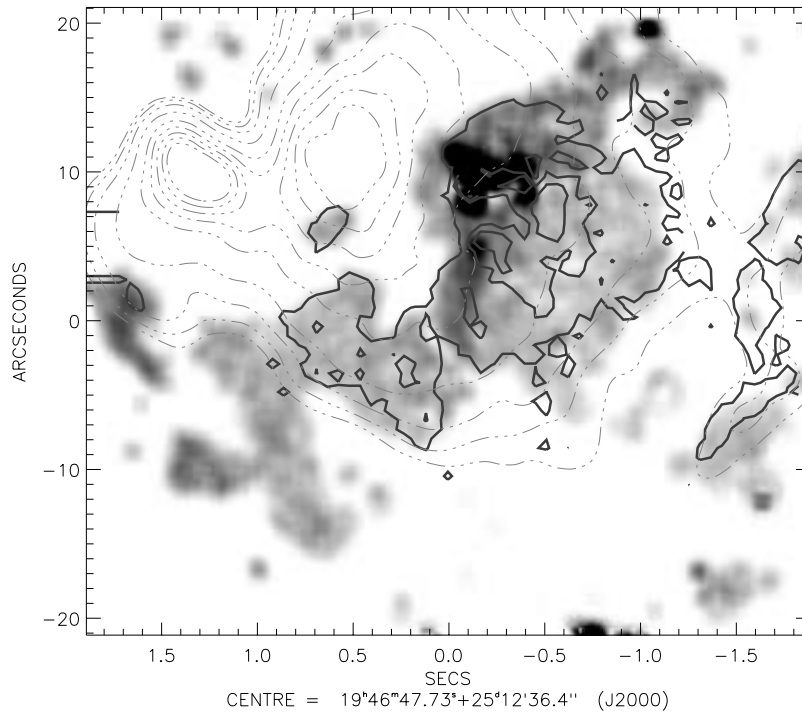
Figure 3.8: Image of the polarised intensity in G61.48+0.09. The solid lines represent the Brγ line emission with contours at 0.3, 0.6, 0.8 and 1.1 mJy/$\square''$. The dotted line corresponds to the 6 cm map with contours at 5, 8, 13, 25, 51, 76, 102, 127 and 152 mJy/beam.

intensity produced in areas where $A_V \sim 10$ mag (i.e. ~ 0.25 pc from star 82) is 8.9×10^{-4} Jy/$\square''$, and where $A_V \sim 20$ mag (i.e. 0.02 pc from star 82) is 2.4×10^{-3} Jy/$\square''$. These detection thresholds are compared with models of magnetohydrodynamic shock waves propagating at speeds between 5 and 50 km s^{-1} in molecular clouds (Draine et al., 1983). The kinematics of the molecular cloud (Schwartz, Wilson & Epstein, 1973; Blair, Peters & Vanden Bout, 1975) results in an average outflow velocity of ~ 20 km s^{-1}. Assuming that the outflow collides with the static surroundings, the models predict intensities lower than 1.6×10^{-5} Jy/$\square''$ (for densities around 10^4 cm^{-3} and B_0 between 50 and 100 μG) and higher than 1.6×10^{-3} Jy/$\square''$ (for densities higher than 10^6 cm^{-3} and B_0 between 500 and 1000 μG). Hence, this detection limit can exclude the presence of a shock at speeds > 20 km s^{-1} for the second case. However, these data cannot exclude the presence of shocks in the first scenario.

3.5   Conclusions

I have presented a high-resolution study of the UCHII region G61.48+0.09 at NIR wavelengths, resolving individual stellar components and studying the extended nebulosity associated with the HII region. The K$'$-band polarimetric map indicates that the B2 component is internally

illuminated and the presence of a point-like source at the same location in the L′-band image obtained with NACO is confirmed. The polarisation data also show that star 82 cannot the main illuminating source of the nebula, and that the contribution of other (undetected) stars is important.

A high resolution extinction map is used in combination with new NIR photometry, and the Brγ emission for star 82, to constrain the spectral type of the main ionising detected stars (star 82, star 83). The NIR SED of star 82 is compatible with a O3V-B1V star, with NIR excess in H, Ks and L′ or with a supergiant in the range O9Ia-A0Ia, showing an IR excess at 3.5 μm. The spectral type of star 83 is compatible with a B0V star. The combined energy budget of these two stars (if star 82 is an O9Ia star) appears to be sufficient to produce the rate of Lyman continuum photons in the B1 component inferred from the 6 cm map. This calculation assumes that the entire radio-emitting region is ionisation-bounded. However, since B1 is cometary (and therefore not ionisation-bounded) if we consider only the Lyman-continuum-photon rate necessary to ionise the radio peak of the B1 component and rescale it to the rest of the region, assuming a central isotropic radiating source, some of the spectral types that reproduce the NIR colours of star 82 and star 83 cannot justify this rate. This would mean that star 82 and star 83 are not the only ionising sources. Since a new star is detected close to the radio-continuum peak with an exposure time of only 29 s in the L′ band, I expect to find more embedded sources in future deep L′- and M′-band images.

An upper limit for the $H_2(1-0)$ S(1) emission is found, which cannot exclude the presence of shocks in lower-density scenarios with B_0 between 50 and 100 μG, but does exclude the existence of shocks if the density is higher than 10^5 cm^{-3} and B_0 between 500 and 1000 μG. The combination of the Brγ and polarisation maps reveals that ionised gas dominates the emission in the south-west region of the nebulosity, suggesting a lack of scattering particles. Toward the north-east scattering gradually begins to dominate and finally drops where the extinction rises sharply. This indicates that we are looking at the foreground wall of the cavity in extinction (north-east) and to the background wall from the scattered light (south-west). This picture reinforces the champagne flow model proposed by Garay et al. (1993).

Chapter 4

Long Slit Spectroscopy of G61.48+0.09

4.1 Introduction

Identification of the ionising sources highly embedded inside UCHɪɪs relies on various direct and indirect methods. Some indirect methods like the rate of Lyman continuum photons or the modelling of the nebular infrared lines must rely on estimates of the distances, geometry and presence of one single source. This same problem arises with the NIR and IR photometry (a direct method) in which the extinction must be calculated by assuming a dynamical distance. The previous chapter has been devoted to the analysis of the stellar content of G61.48+0.09, a complex UCHɪɪ, by means of several of these methods, such as the polarimetric maps and the rate of Lyman continuum photons, and its comparison with the already existing NIR photometry.

Photospheric lines in the NIR show a clear dependence with the effective temperature of the stars (Hanson et al., 1996). Early O-type stars show emission features, corresponding to C ɪᴠ (2.069, 2.078 and 2.083 μm) and N ɪɪɪ (2.115 μm), as well as He ɪɪ (2.188 μm) absorption lines. For late-O and early-B stars, He ɪ absorption lines provide a temperature diagnostic. Detection of stellar photospheric features have allowed the identification of the central ionising star in several Hɪɪ regions (Watson and Hanson, 1997; Martín-Hernández et al., 2003; Bik et al., 2002, 2003). K-band long-slit spectroscopy of several stars within G61.48+0.09 is intended to detect these photospheric features and to analyse the recombination nebular lines in order to better pin down the temperature of the main ionising stars and their spatial variations along the nebula.

4.2 Observations and Data Reduction

On 2003 September 20th and 21st, K-band spectra of G61.48+0.09 were obtained as part of a larger project comprising 5 northern UCHɪɪs, using the NIR long-slit spectrograph facility of NICS at the 3.5 m Telescopio Nazionale Galileo (Observatorio del Roque de los Muchachos, La Palma).

The $0''\!.75 \times 4'$ slit was used in order to obtain medium resolution spectra ($\lambda/\Delta\lambda$ =1700 in 3
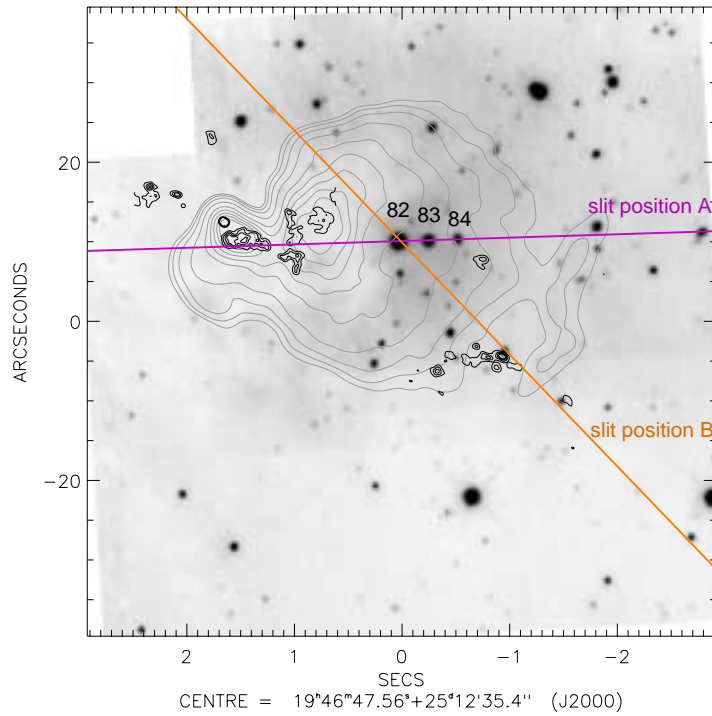
Figure 4.1: Same K′-band image of G61.48+0.09 as in Fig. 3.1. The two orientations of the slit are overlayed on the image. K-band spectra has been extracted for the stars marked in the image.

pixel) of four sources embedded in the free-free compact emission of G61.48+0.09 (see Fig. 4.1), namely stars 82, 83, 84 and 85 (following notation of Alvarez et al. (2004)). The slit was aligned in two different directions, with star 82 appearing in both orientations to permit registering the spectra. The grating setting covered the range of wavelengths between 2.0 and 2.3 μm. The sources were nodded along the slit in two different positions, separated by $\sim 40''$, allowing correcting for the sky background emission by subtracting one position from the other. The parameters of the NICS observations are summarised in Table 4.1.

The spectra were extracted in a synthetic aperture of $2 \times$FWHM $\times$ $0.''75$ width centred on each of the four stars. In order to correct for the atmospheric telluric absorptions, a nearby A0 star was observed after the observation of the UCHII. Early A stars are featureless across the entire K band, except for absorption in the Brγ line at 2.1661 μm. This feature was modeled with a Voigt profile and removed from the spectra of the standard. Calibration of the telluric absorption was performed by the division of the one-dimensional spectrum of the source by the A star spectrum. Finally, flux calibration was done by modelling the standard star with an artificial blackbody spectrum of T_{eff} =9792 K and by multiplying it by the *cleaned* spectrum of the source. However, due to the poor transparency of the night (cirrus were present on both nights) the flux calibration is only approximated (35%).

Parameter	2003 September 20	2003 September 21
Wavelength (μm)	1.93-2.36	1.93-2.36
Resolution	1700	1700
Integration time (seconds per offset position)	600 ($\times$ 8 offset position)	600 ($\times$ 4 offset position)
Pixel scale ($''$)	0.25	0.25
Slit ($''$)	0.75	0.75
P.A. ($°$)	92	44
FWHM ($''$)	0.6	0.5
Standard star	HD188485	HD188485

Table 4.1: Parameters of NICS for the data set.

4.3 Results and Discussion

4.3.1 Stellar Spectra

Spectra in the two slit positions are presented in Fig. 4.2 and Fig. 4.3. The errors have been computed by calculation of the standard deviation of the different spectra obtained throughout the two nights, after normalisation. All stars reproduce roughly the Ks-broad-band photometry reported by Alvarez et al. (2004). One of the most prominent characteristics detected in the spectra is the steep slope in the continuum of star 82, which appears in the two spectra obtained at the different slit orientations. The presence of an absorption feature at a wavelength slightly swhortward of the Brγ line (also detected in the calibration standard) prevented the registration of the spectra from both slit orientations. This slope could be produced by two possible effects: (a) a very strong extinction; higher than that estimated in Sect. 3.4.2 of Chapter 3 for this source (for a comparison, see the spectra in Fig. 4.4 after dereddening), (b) a strong excess, possibly produced by circumstellar material.

There seems to be no evidence of photospheric features, even in the case of star 82, whose S/N$\sim$80. This fact was also reported by Hanson et al. (2002b) on similar observations of stars 82, 83 and 84, obtained with the MMT. However, the overall low SNR (see column [3] of Table 4.2) does not allow ruling out OB features, that may be detected with 8 m-class telescopes.

Recombination lines of hydrogen and helium are used to probe the radiation field of underlying stars in compact H II regions (Hanson et al., 2002b; Kaper et al., 2002a; Martín-Hernández et al., 2003; Watson and Hanson, 1997). The nebular recombination lines detected in all the spectra correspond to HeI (2^1P-2^1S) at 2.0581 μm and HI (4-7) Brγ at 2.1661 μm, which are very strong. A weak presence of molecular hydrogen H$_2$1-0 S(1) is detected in most sources. Line intensities are given in Table 4.2, after dereddening them with the estimated extinction values, derived in Chap. 3 for G61.48+0.09. There are other three unresolved HeI (4^3S-3^3P) transitions at 2.1127 μm and one at 2.1138 μm (4^1S-3^1P) in this wavelength range that are only detected for star 84. Upper limits are derived for four sources at this wavelength, considering the 3σ level of detection and the average FWHM of the detected lines. Some authors have inferred temperature properties of the embedded stars (Armand et al., 1996; Depoy and Shields, 1994) from the HeI line at 2.0581 μm, but this line is complicated to model due to the fact that it can be influenced by collisional excitation from the metastable 2^1S level and from the triplet series (Lumsden et al., 2003). Only more recent photoionisation models, such as CLOUDY, include most of this effects, but this calculation has to be left for
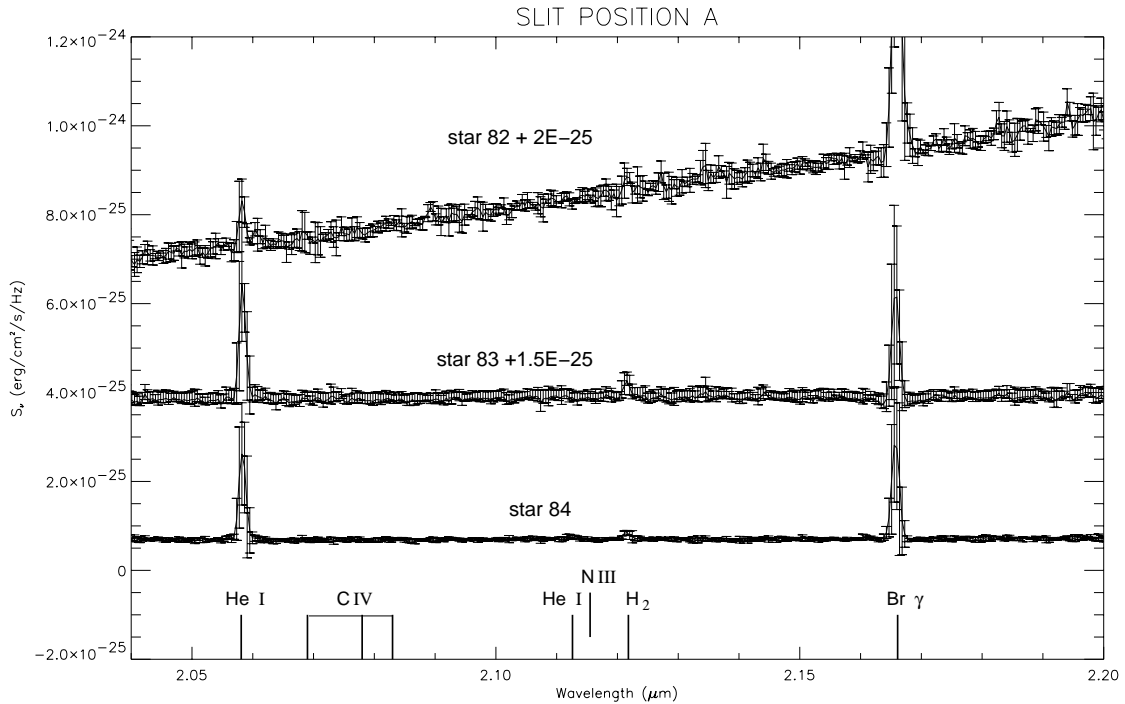
Figure 4.2: K-band spectra of stars 82, 83 and 84 obtained integrating over a $1''2 \times 0''75$ synthetic aperture in the slit orientation A. The identification of the lines detected and their intensities are listed in Table 4.2

the future. Instead, the use of line intensities and upper limits derived from the HeI 2.11 μm transition can reveal some information about these stars.

Comparison of the line intensity ratio I(He 2.11)/I(Brγ) with Table 3 of Hanson et al. (2002a), reproduced in Table 4.3, shows that, to the limit of detection, star 82 and 83 are not compatible with an early O star. This is compatible with the spectral type O9.5, derived from the radio continuum observations and presented in Chapter 3. The star 84 is likely an early O star, while star 85 is compatible with any O-spectral type.

4.3.2   Spatial Variation of Nebular Lines

The nebular line emission extends over $\sim 25''$ along both slit orientations. The spatial distribution of this nebular emission could be traced using the HeI (2^1P-2^1S) at 2.0581 μm and HI (4-7) Brγ at 2.1661 μm lines. The intensities obtained in 10 minutes of integration time, once subtracted from the continuum and normalised, are presented in Fig. 4.5. The spatial profile presents a strong peak coinciding with the location of star 82. Apparently, this peak might correspond to the spectrum of the star, as reported in Chapter 3. The fact that a similar enhancement is not seen in the HeI line supports this conclusion. In this case, the estimate of the nebular helium to Brγ ratio would be lower and the conclusion on the spectral type of this star addressed in the previous section would not be valid.

The spatial distribution of the nebular emission traced by the two lines is very similar, dropping fast in the east direction for slit position A and to the north-east in the slit position B. This is very likely produced by the foreground extinction, that has been proven to reach up to forty magnitudes in the visual (see Chapter 3), since the radio continuum emission extends further (see Fig. 4.1). Despite this effect, a slight increase is observed at $\sim 9''$ east
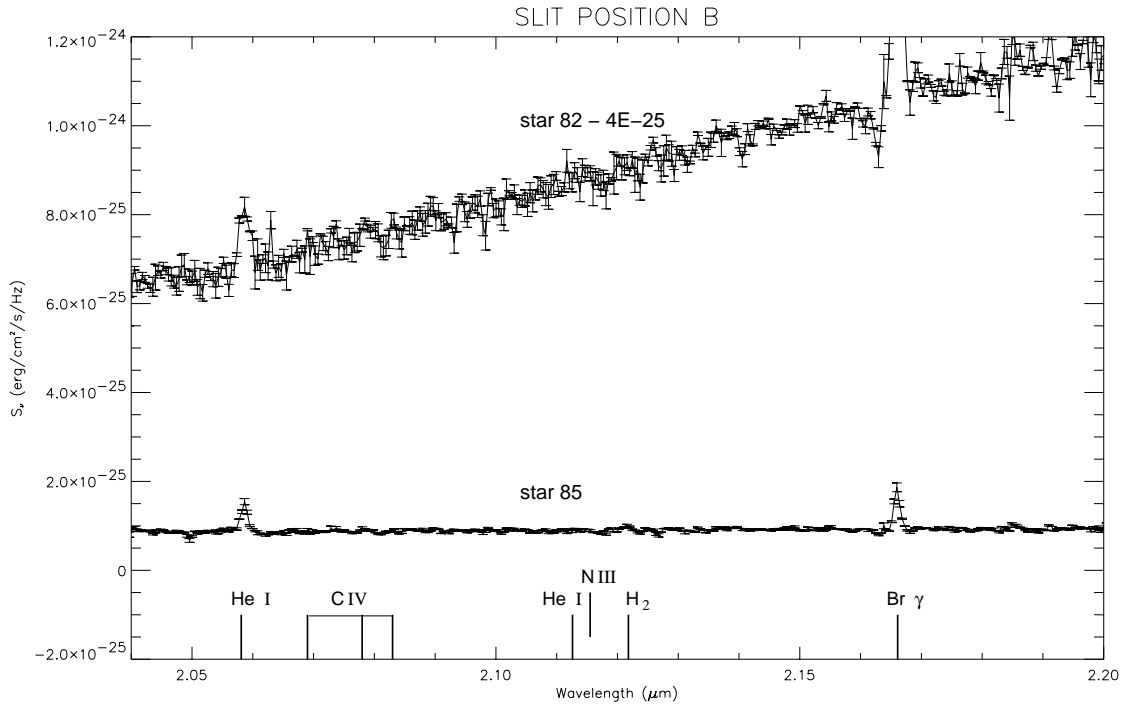
Figure 4.3: K-band spectra of stars 82 and 85 obtained over a $0.\!''5 \times 0.\!''75$ synthetic aperture in the slit orientation B. The identification of the lines detected and intensities are listed in Table 4.2

from star 82, around the location of the peak in the radio continuum map. In the $5''$ region around the location of star 82 there exists a significant mismatch between the two spatial line profiles. This characteristic is also indicative that star 82 has a lower temperature than 40000 K, since at higher temperatures, both H and He are singly ionised and the radius of the volume occupied by H^+ and He^+ hydrogen and helium coincide. In Fig. 4.5 Left, the normalised intensity of the HeI drops faster to the west, increasing again at $20''$ from star 82. This corresponds to the diffuse tail observed in radio continuum and in broad-band images (see Fig. 4.1). This tail is also traced by the spatial profiles extracted from the slit orientation B, but the bridge between the region and the tail is fairly continuous (at the location of star 85, $\sim19''$ from star 82). This shows that indeed there is ionised material, most likely in a compact region, since it mostly shows up in the 6 cm map at high resolution.

4.4 Conclusions

I have presented the stellar NIR long slit spectra around the location of four stars deeply embedded in the UCHII G61.48+0.09 and the surrounding nebular material, with a slit oriented in two directions. Unfortunately, no photospheric lines have been detected for any of the stellar objects. However, the signal-to-noise ratio of these spectra is still too low to rule out OB features. Alternatively, upper limits could be given for the HeI 2.11 μm line and line ratios relative to the HI Brγ, allowing to constrain the spectral types of stars 82 and 83 to later than O7, respectively. The spatial variation of the nebular lines reveals an excess of HI Brγ, confirming what was reported in Sect. 3. The mismatch between the profiles of the two lines indicates that star 82 has a temperature lower than 40000 K. Further follow-up observations
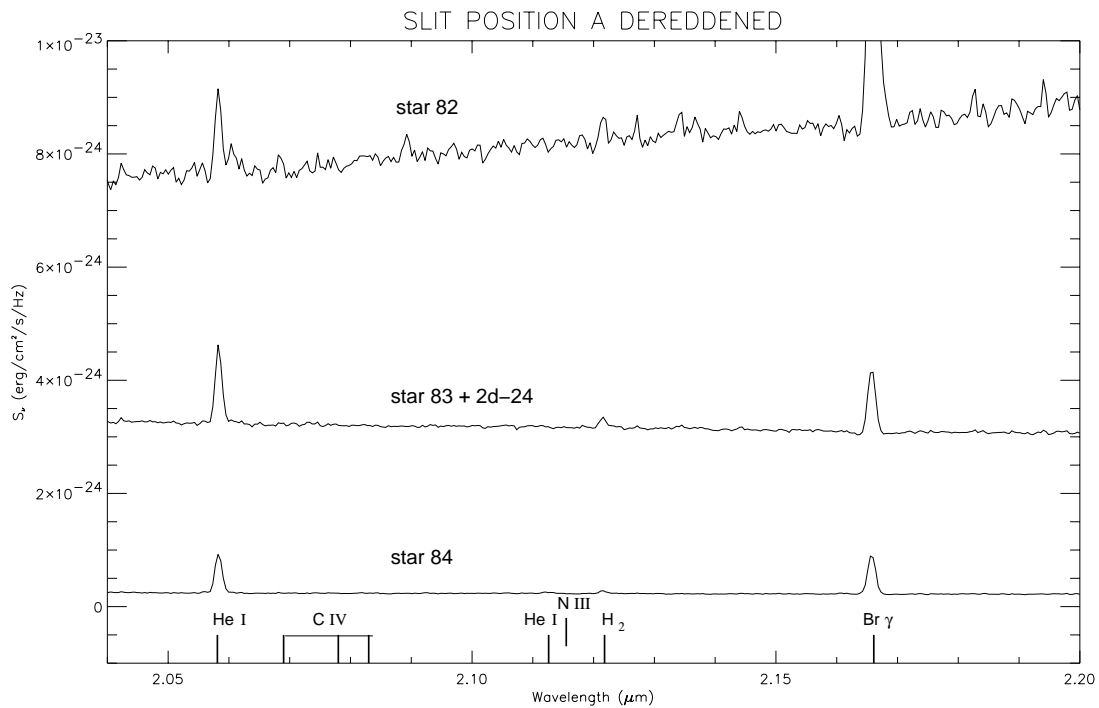
Figure 4.4: Same spectra as in Fig. 4.2, dereddened by the visual extinction calculated in Chap. 3 and listed in column [4] of Table 4.2

with larger telescopes (8m-class) will significantly increase the SNR, allowing the detection of photospheric lines that might put firmer constrains in the temperature of the stars, unveiling finally the ionising source of this UCHII. Further detailed modelling of nebular recombination lines of H and He should be performed using a detailed photoionisation code.
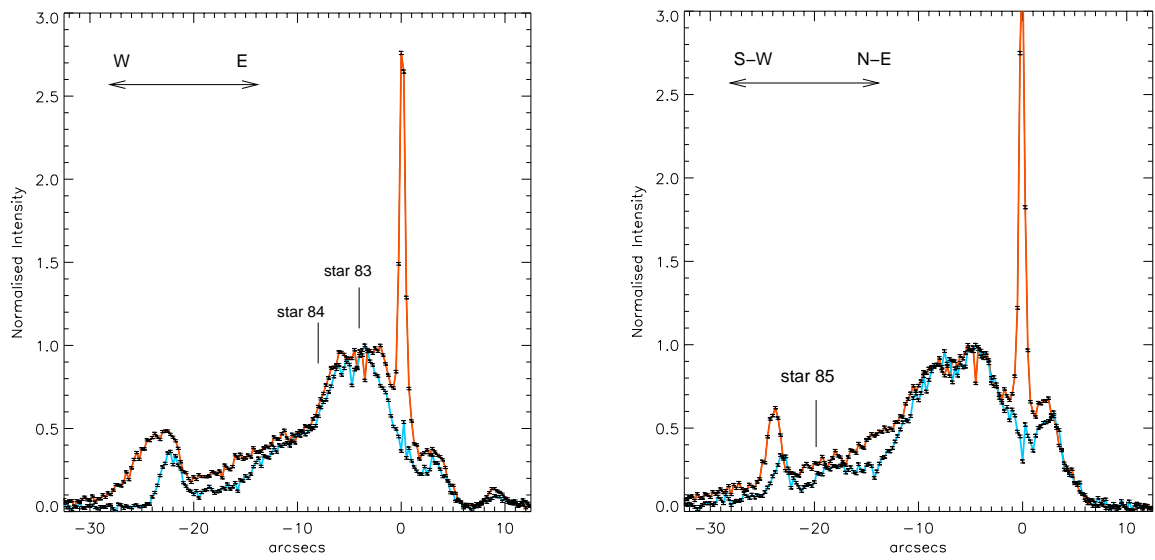
Figure 4.5: Left: Spatial variation of the Brγ (blue-solid line) and HeI 2.0581 μm (red-solid line) lines along the slit A, oriented in an east-west direction. The intensity has been normalised to the maximum of the nebular emission outside the peak region. The origin of the horizontal axis corresponds to the location of star 82. Right: The same diagram is represented for the slit B, oriented in the NE-SW direction.

Slit	Object	S/N	A_V^* (mag)	HeI 2^1P-2^1S 2.0581 (μm)	HeI $4^{3,1}$S-$3^{3,1}$P 2.11 (μm)	H$_2$ 1-0 S(1) 2.1218 (μm)	H 7-4(Brγ) 2.1661 (μm)	I(He 2.06)/I(Brγ)	I(He 2.11)/I(Brγ)
					Flux (in 10^{15} erg/s/cm^2)				
A	star 82	75	24	120.3	<19.2	–	729.9	0.165	<0.026
A	star 83	60	15	131.6	<3.4	25.3	112.3	1.172	<0.031
A	star 84	35	11	69.94	3.25	7.4	70.13	0.993	0.046
B	star 82	50	24	243.9	<44.2	–	1018.7	0.239	<0.043
B	star 85	30	9	16.9	<1.5	–	18.2	0.928	<0.085

Table 4.2: Dereddened line intensities.* A$_V$ estimated in Chap. 3.

Approximate T_{eff} (K)	Spectral Type	I(He 2.11 μm)/I(Brγ)
≥40000..........	≤ O7V	≥0.035
39000-34000....	Late O	0.030-0.010
<34000..........	No O Star	≤0.010

Table 4.3: Based on Benjamin et al. (1999) and assuming T_{eff} =7500 K, n_e=10^3 cm^{-3}, and a helium abundance ratio of n(He)/n(H)=0.10.

Chapter 5

Kinematical Study of G5.89-0.39

5.1 Introduction

As explained in Chapter 1, the kinematics of UCHIIs give an insight into the formation mechanism of massive stars and their interaction with the surrounding molecular cloud. Signs of outflows & discs have been identified in $\sim$8 YSO (Garay and Lizano, 1999) and in some examples of UCHII (Garay et al., 1998a,b; Okamoto et al., 2003a) as support for the accretion mechanism. In the previous chapters I focused on the ionising sources that produce the HII regions. Here, I will analyse the kinematical structure of one of the most striking examples of UCHIIs.

G5.89-0.39 (also known as W28 A2) is an UCHII region, first identified as a very compact HII region by radio observations (Turner et al., 1974), and later catalogued as a shell type of $\sim$5″ diameter, with a spatial resolution of 0.″4 at 2 and 6 cm with the VLA (Wood and Churchwell, 1989; Zijlstra et al., 1990). This source is located at a distance of 1.9 kpc, and shows a ring-like structure that has been proposed to be produced by the evacuation of the inner cavity, due to the wind of the ionising-central star (Wood and Churchwell, 1989). The spectral type of the central star has been inferred from radio observations at various wavelengths. Initial studies from Wood and Churchwell (1989) assumed that the emission at 2 cm was optically thin, giving a spectral type B0V. Later studies revealed that the continuum emission toward this UCHII is optically thin for wavelengths shortward than 1.3 cm (Gomez et al., 1991), and the emission at this wavelength yields a spectral type O8/O8.5V, consistent with that estimated from the full spectral energy distribution (Faison et al., 1998). Subsequent studies in the NIR, at high angular resolution, have focused on the stellar population and the direct detection of the ionising source (Feldt et al., 1999, 1998, 2003), not finding evidence of the presence of a central source, but an off-centre star (α_{2000}=18^{h}00^{m}30^{s}44$\pm$0^{s}013, δ_{2000}=-24°04′00.″9$\pm$0.″2), whose determined spectral type derived from its position in the L, L$-$K diagram is O5V.

G5.89-0.39 has a highly energetic outflow that has been widely studied with different tracers and various spatial resolutions. Harvey and Forveille (1988) observed G5.89-0.39 in several molecular lines: CO (1-0), ^{13}CO (1-0), C^{18}O (1-0), identifying a bipolar outflow in the east-west direction, and estimating the total mass of the outflow $\sim$70 M$_\odot$. This east-west direction was however proposed to be that of a disc located almost outside the ionised area, and surrounding a central star (Zijlstra et al., 1990), while the outflow (in a northwest-southeast orientation) would be originating from the disc (Gomez et al., 1991). Recently, the study of

the H92α radio-recombination line and the 8.3 GHz continuum with the VLA (Rodríguez-Rico et al., 2002) concluded that the velocity gradient inside the ionised region requires more than rotation to be explained. NIR observations also support the northwest-southeast orientation of a bipolar structure (Harvey et al., 1994). The study of the expansion of G5.89-0.39 by Acord et al. (1998) yielded an expansion rate of 4 ± 1 mas yr^{-1}, and at the same time, showed a preferred direction of this expansion (slightly northwest-southeast). C^{34}S single-dish observations, with spatial resolution $\sim18''$, showed a north-south orientation of the outflow (Cesaroni et al., 1991), also supported by the position of the H$_2$O masers (Hofner and Churchwell, 1996). Yet, another orientation was proposed for the outflow by Acord et al. (1997) since the SiO v=0 (1–0) line, observed with the VLA, at a resolution of $\sim2.5''$, shows a northeast-southwest bipolarity, also indicated by the hydroxyl maser emission (Argon et al., 2000) within the radio-continuum emission.

It has been underlined before that the spatial resolution of these observations cannot rule out the superimposition of various outflows in G5.89-0.39 (Acord et al., 1997, 1998). However, the morphological classification of this source, that suggests the presence of a central star, has induced conclusions on a single central star.

A further evidence for the presence of moving matter in G5.89-0.39 is given in the NIR wavelength range through the H$_2$ emission at 2.121 μm that was detected initially by Oliva and Moorwood (1986) with a poor spatial resolution, and later by Feldt et al. (1999) with a resolution of 1.5$''$ in three locations around the UCH$_{II}$ region (A, B and C), at a projected average distance of $\sim10''$. The most prominent area of emission is located $\sim8''$ to the south of the nebula (integrated flux = $1.2(\pm0.1) \times 10^{-16}$ W m^{-2}), appearing unresolved with their low spatial resolution (see Fig. 5.1). This same work proposed a north-south orientation of the outflow, associated with the A and C regions.

This chapter is aimed to investigate the driving source(s) and orientation of the outflow in G5.89-0.39 in the small scales, at high angular resolution, paying special attention to the nature and kinematics of the nearby H$_2$ emission and the Brγ emission, produced by the ionised gas within the nebula. The analysis is based on long-slit spectroscopy in the K band and Fabry-Perot imaging, also at wavelengths around 2 μm. The data presented could be compared with published NACO broad-band images, showing the region at the highest spatial resolution to date.

5.2   Observations and Data Reduction

5.2.1   NIR-Long-slit Spectroscopy

Long-slit spectroscopy of G5.89-0.39 in the K band (2.0–2.4 μm) was obtained in September 2000 with the Adaptive-Optics system ALFA (Kasper et al., 2000) at the 3.5 m telescope (Calar Alto, Spain). The AO system was locked on the star S301200139515[1] (m$_V$ =13.2), giving an average resolution of $\sim0.''6$. The $0.''36$-wide slit was positioned in an almost north-south orientation over G5.89-0.39 and the knot of H$_2$ emission, located at $\sim8''$ south of the nebula (see Fig. 5.1). The spectral resolution was R=500 and the pixel scale $0.''08$/pixel. Two exposures were taken with $\sim2.''5$ separation, with a total integration time of 32 minutes. Standard data reduction techniques were applied, except that for flat-fielding, and for the wavelength calibration and detector's distortion, I utilised the OH sky-lines present in the

---

[1]Following notation of the GSC 2.2 Catalogue

spectra. Because of the close airmass at which both the object and the calibrating star were, the telluric absorption was calibrated by simply dividing the spectrum by that of the star SAO186169. Since the interest is centred only in the line intensity ratios, no flux calibration was obtained.
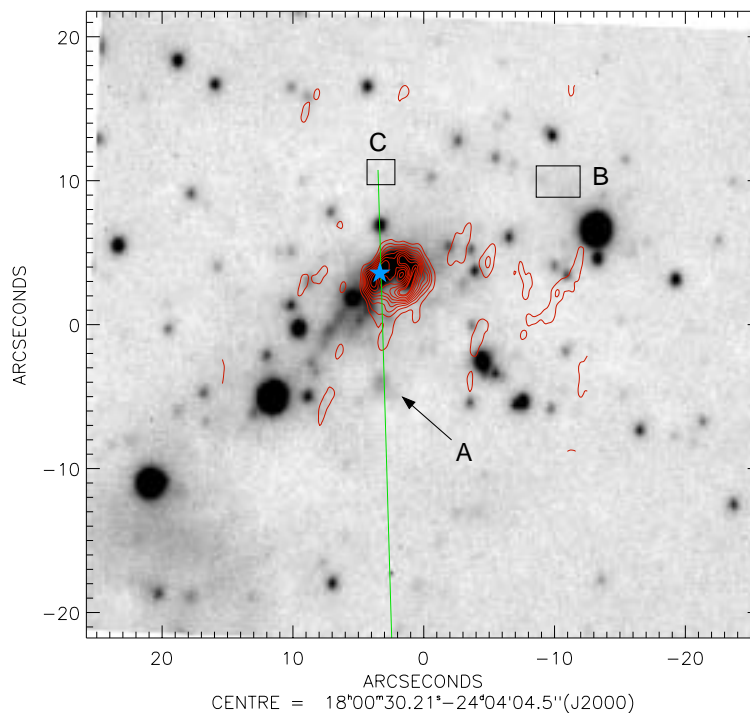
Figure 5.1: ALFA K-band image of G5.89-0.39 from Alvarez et al. (2004) in logarithmic scale. The greyscale varies from 60 mJy/□ ″ (light) and 62 mJy/□ ″ (dark). Red contours represent the 2 cm emission (Wood and Churchwell (1989)) at -0.06, -0.03, 0.03, 0.06, 0.09, 0.11, 0.14, 0.17, 0.20, 0.23, 0.26 and 0.27 Jy/beam. The blue star represents the location of the possible ionising star, detected by Feldt et al. (2003). The orientation of the $0''36$ width slit on the sky is depicted in green. The knots of H_2 emission at 2.122 μm, are labeled after Feldt et al. (1999).

5.2.2 Fabry-Perot Spectroscopy

Observations of G5.89-0.39 were conducted in March 2000 at the 3.6 m telescope in La Silla (Chile), with the combination of the ESO's AO system ADONIS (Beuzit et al., 1994) and the instrument Graf (Chalabaev et al., 2003). Graf is a 3D spectrograph that operates in the NIR and makes use of a Fabry-Perot interferometer (FPI) (a Queensgate FPI with 500 μm of average plate spacing), providing a spectral resolution $\lambda/\Delta\lambda{\sim}7000$ or Δv=40 km s^{-1} in the K band. The field of view of this instrument is limited by a rectangular mask of $17''{\times}12''$ in the K band and the pixelscale is $0''1$/pixel. Observations of the H_2 v=1-0 S(1) emission line of the UCHII and surroundings (with the window rotated in the north-south direction), and

Brγ toward the ionised region were performed under very good seeing conditions.

The reference star for the ADONIS system is S301200139515, an m$_V$=13.2 mag star from the GSC-2 catalogue at ESO.

Each of the regions was observed in two different offset beam positions, separated by 4$''$, in order to subtract the background emission. After combination of the beams, every single channel has a total on-source integration time of 360 seconds. The southern knot was observed over 9 velocity channels, with centre on the H$_2$ v=1-0 S(1) emission line, and the observations of the ionised nebula are composed of 11 velocity channels around Brγ. Since the interest is focused only on the shifts and shape of the velocity profiles, no flux calibration was performed for these observations. Calibration of the pixel sensitivity for every single wavelength-channel was made by taking images of a white lamp, subtraction of the bias and normalisation, following the standard reduction techniques. The wavelength calibration of the data was performed by observing the krypton lines, centred at 2.1902513 μm and 2.1165471[2] μm, respectively, produced by a calibration lamp (with steps of 1.21$\times$ 10^{-4} μm). The first one was used to calibrate the observations of the Brγ line (2.16553[3] μm), while the second was used for the H$_2$ v=1-0 S(1) line data. This calibration includes the determination of the wavelength zeropoint calibration and the phase shift correction (see Sect. 5.2.2). The data cube corresponding to the calibration line is analysed at every pixel location, in the wavelength direction. The line profile at each pixel is fitted to a Gaussian, whose centre describes a paraboloid over the x,y dimensions (see Fig. 5.2). The wavelength corresponding to the vertex of the paraboloid sets the zeropoint, and the distance from the plane of the vertex to the paraboloid in the z direction is the *phase shift*. For every wavelength of the datacube, the line profile is interpolated, according to the corresponding phase shift at this location. This transforms the paraboloidal surfaces for each wavelength into planes (see Fig. 5.3). The residual rms of the phase calibration is equivalent to an error of $\sim$3 km s^{-1}.

To reduce the noise, it was necessary to apply a spatial median filter with a box size of 5$\times$5 pixels, which did not severely degrade the spatial resolution.

Fabry-Perot data description

Graf is a Fabry-Perot interferometer that provides spectral information over a field of view of 17$''\times$12$''$. The interferometer, placed in the collimated beam of the telescope, consists of two semi-transparent plates with tunable separation. The signal, modulated by the interferometer is re-imaged on the detector, yielding a cube of images (each one corresponding to a determined separation of the plates). A filter isolates one of the transmitted interference orders and the respective observed wavelength. The transmissivity of a Fabry-Perot interferometer, illuminated by a monochromatic radiation of wavelength λ, is defined by Airy$'$s formula:

$$\frac{I}{I_0} = \frac{1}{1 + F\sin^2\frac{\delta}{2}},\tag{5.1}$$

where $F = 4R/(1 - R)^2$, with R being the reflectivity of the etalon plate coatings, and $\frac{\delta}{2} = \frac{2\pi}{\lambda}nd\cos\epsilon$. This transitivity is maximum when

$$m\lambda = 2nd\cos\epsilon,\tag{5.2}$$

---

[2]Air wavelength

[3]Air wavelength
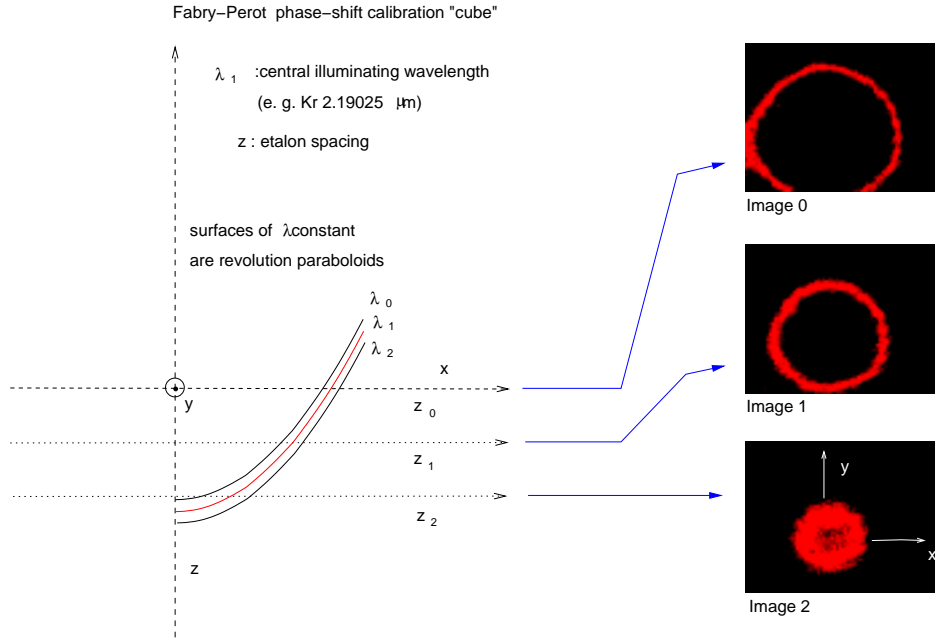
Figure 5.2: Sketch of the Fabry-Perot phase-shift calibation images obtained with the calibration lamp. The images allow to reconstruct the paraboloid surface and the shift between the theoretical wavelength of the lamp and the observed one.

where m is the interference order, n is the refraction index of air, d is the separation between the plates and ϵ is the incident angle of the collimated light onto the etalon.

For fixed values of λ and ϵ, Eq. 5.2 is satisfied by a series of equally spaced separation values (d), one for each order (m). Therefore, as d varies, the profile consists of a periodic series of relatively narrow and symmetrical peaks, interspersed with almost complete darkness.

Equation 5.2 shows that the wavelength transmitted by the etalon for a certain interference order is not only dependent on the separation of the plates, but also on the incident angle of the light (i.e. the position on the detector). This effect causes the spatial directions $(x,y;z)$ to not correspond to the desired spectral directions $(x,y;\lambda)$. Assuming that the separation of the plates (d) has a linear relationship with the parameter z, Eq. 5.2 can be rewritten as

$$m\lambda = (A + Bz)\cos[\tan^{-1}(\frac{r}{C})] = \frac{A + Bz}{\sqrt{1 + \left(\frac{r}{C}\right)}} \tag{5.3}$$

where $A = 2nd_0$ and $B = 2nc$, and the angle from the optical axis is redefined as $\epsilon = \tan^{-1}(r/C)$, and r and C correspond to the distance from the optical axis in pixels and the focal length of the camera in pixels, respectively (Gordon et al., 2000). After a quadratic approximation, Eq. 5.3 can be expressed by

$$m\lambda \approx A + Bz - \left(\frac{A}{2C^2}\right)r^2 \tag{5.4}$$

This is the equation of a paraboloid for every wavelength, with centre on the optical axis. In

the case of Graf, the dependency of the z-dimension with the separation of the plates appears automatically in the header of the data cube. The process of transforming the paraboloids in planes that correspond to a single wavelength is known as *phase shift calibration.*
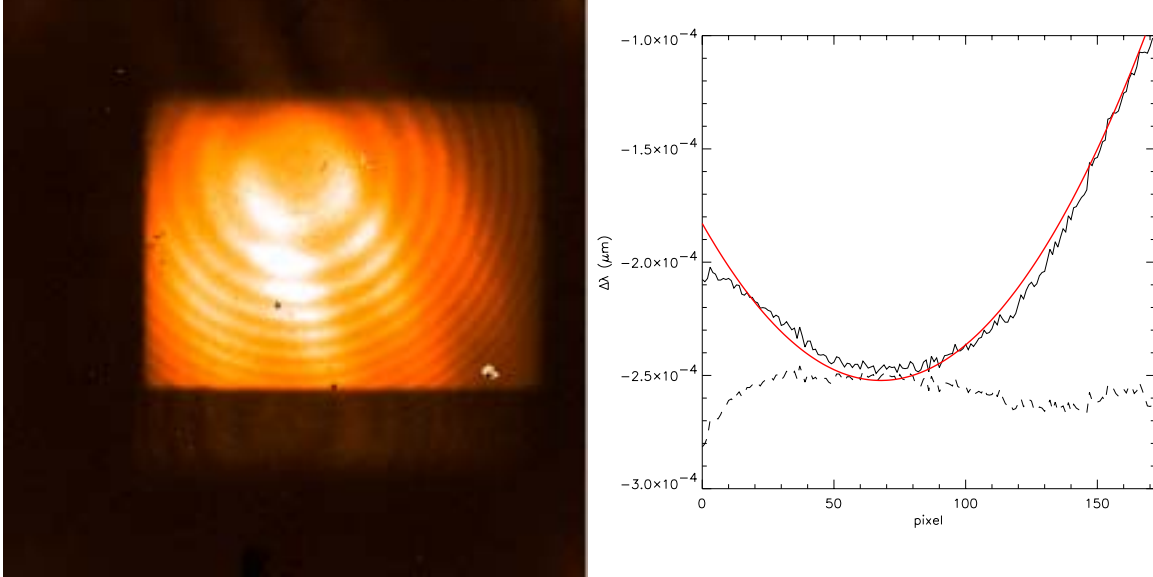
Figure 5.3: Left: Image of one of the channels of the raw krypton phase cube. The visible interferometric rings are due to parasitic interferences produced in the filter located at the entrance of the cryostat and at the surface of the detector. Right: The black solid line represents the wavelength of maximum transmission of the 2.1902513 μm krypton line over one line in the spatial direction of the calibrating phase cube. The red line is the model fitted to the data. The broken line depicts the residuals after the phase shift calibration of the same cube.

For more information on the calibration of Fabry-Perot observations see Gordon et al. (2000); Hartung (2003) and references therein.

Astrometry

The astrometric calibration of the Graf observations is extremely difficult due to the small field of view of the Fabry-Perot, and becomes specially challenging in the cases of extended emission. The astrometry of the Brγ images was made by comparing the image of integrated velocities with the NACO Ks image, using the point-like source reported by Feldt et al. (2003). With only one star, no platescale solution could be calculated, and therefore the platescale of the Graf-SHARP manual ($0\rlap{.}''1$/pixel) is assumed for these images. In the case of the southern knot (A), there are no point-like sources; hence the position of the dark lane was used to register the declination and the line that joins the two lobes for the right ascension. The final astrometric precision is $0\rlap{.}''2$.

5.3   Results and Discussion

The Fabry-Perot observations of G5.89-0.39 and the $20''$ around it in the H$_2$ v=1-0 S(1) detect only the emission at the location of the southern knot (A), previously reported by Feldt et al.

(1999). For this reason, the kinematical study of the emission at this wavelength is limited to the location of this southern knot. The field of view in the case of the Brγ Frabry-Perot images is centred at the location of G5.89-0.39 and its analysis focuses on the ionised region.

5.3.1 The Southern Spot: H_2 line emission

The analysis of the H_2 emission detected in the brightest spot, $\sim 10''$ south from G5.89-0.39, aims to find out whether this emission is connected to the outflow previously reported towards this UCHII region. The location of this knot is also coincident with the position of the blue lobe, detected in the $C^{34}S$ maps, and constitutes one of the main arguments for the north-south orientation of the outflow (Cesaroni et al., 1991).
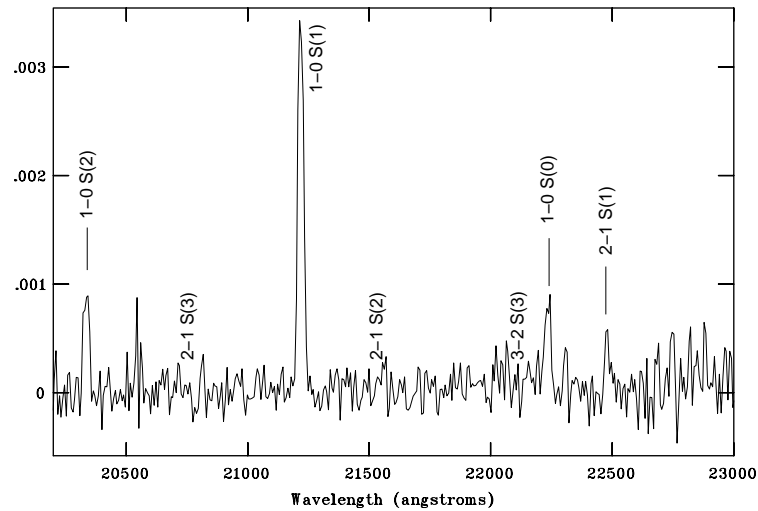
Figure 5.4: ALFA K-band spectrum of the knot south of G5.89-0.39. The spectral resolution is R$\sim$500.

The H_2 emission can be caused either by radiative excitation (fluorescence) or by collisional excitation (shocks). To discriminate between these two excitation mechanisms, the ratios between several ro-vibrational emission lines (especially those with upper energy levels v=2) have been studied.

In Fig. 5.4, the long-slit K-band spectroscopy of this knot, with low spectral resolution (R$\sim$500), is presented. Even with a low signal-to-noise ratio (the spectrum is not flat-fielded), the H_2 ro-vibrational lines v=1-0 S(2), v=1-0 S(1), v=1-0 S(0) and v=2-1 S(1) are detected (see Fig. 5.4). The lines v=3-2 S(3), v=2-1 S(3) and v=2-1 S(2) are below the noise levels. The upper limit in the transmissivity of the K-band filter (2.427 μm) renders impossible the study of the Q-lines of the molecular hydrogen, whose comparison with the S rotational transitions would derive the extinction toward this source.

The line intensity ratios with respect to the v=1-0 S(1) line are presented in Table 5.1. The errors are derived through the Gaussian propagation of the residuals of the fit to a Gaussian profile for every line.

The non-detection of v=3-2 S(3), v=2-1 S(3) and v=2-1 S(2) yield upper limits in the ratios,

Model	log n (cm^{-3})	log χ $\times$ISRF	T (K)	1-0 S(2) 2.034 μm	2-1 S(3) 2.074 μm	2-1 S(2) 2.154 μm	3-2 S(3) 2.201 μm	1-0 S(0) 2.223 μm	2-1 S(1) 2.247 μm
14[a]	3.5	3.0	100	0.50	0.35	0.28	0.18	0.46	0.56
Gm3o[b]	4.0	2.0	300	0.46	0.31	0.23	0.15	0.44	0.52
Mw3o[b]	5.0	4.0	500	0.37	0.47	0.19	0.21	0.30	0.46
Rh3o[b]	6.0	5.0	1000	0.28	0.24	0.09	0.08	0.33	0.24
S1[a]	n/a	n/a	1000	0.27	<0.01	<0.01	<0.01	0.28	<0.01
S2[a]	n/a	n/a	2000	0.37	0.8	0.03	<0.01	0.21	0.08
This work				0.26(0.03)	<0.01	<0.01	<0.01	0.23(0.04)	0.10(0.03)

Table 5.1: Line intensity ratios with respect to the v=1-0 S(1) line, calculated with UV pumping models (Draine and Bertoldi, 1996; Black and van Dishoeck, 1987) and thermal distributions, caused by shocks (Black and van Dishoeck, 1987). The first models are mostly sensitive to densities (first column) and radiation fields (second column).

[a] Models of Black and van Dishoeck (1987)

[b] Models of Draine and Bertoldi (1996)

but this already indicates that this is thermally excited gas, since only the first vibrational levels are populated. In this table, the new results are compared with the models on infrared emission of H_2, excited by radiative absorption and by thermal excitation produced by shocks. The first models contemplate two regimes: densities below a critical value ($\sim 10^4$ cm^{-3}), where the excitation is produced by the UV radiation (Black and van Dishoeck, 1987), and densities above this limit, where thermal collisional excitation becomes dominant (Draine and Bertoldi, 1996). The last two models (S1 and S2) correspond to pure thermal distributions of H_2, normally heated by shocks.

This comparison of line intensities points to the H_2 emission being caused by thermal excitation through shocks. Moreover, the ratio between the intensities of v=2-1 S(1) and the v=1-0 S(1) line is consistent with the predictions from C-type shock models (Burton et al., 1992). I finally conclude that the H_2 emission is most probably caused by shocks.

5.3.2 The Southern Spot: Kinematics

It is well-known that CO outflows and H_2 emission are spatially well correlated, appearing this last one typically as jets or knots. In the case of G5.89-0.39, the east-west orientation of the ^{12}CO outflow given by Harvey and Forveille (1988) does not agree with the location of the H_2 emission by Feldt et al. (1999). However, these authors acknowledge a velocity gradient in all directions, traced by the ^{13}CO, that together with the poor spatial resolution of the radio data do not rule out other possible orientations.

The kinematical information obtained with the Fabry-Perot interferometer of the H_2 v=1-0 S(1) line in the wavelength range 2.1199-2.1212 μm is presented in figures 5.2 and 5.5. The map of integrated velocities is depicted in Fig. 5.5 Left, including the continuum emission. This map reveals that this source is resolved into two knots oriented in the north-south direction, being confirmed by the K_s-band NACO image of the same region (Feldt et al., 2003) at an angular resolution of 0″11, shown in Fig. 5.5 Right.

Table. 5.2 represents a mosaic of velocity channels obtained from the continuum-subtracted H_2-line emission of the source, once corrected for the motion of the observer in the direction of
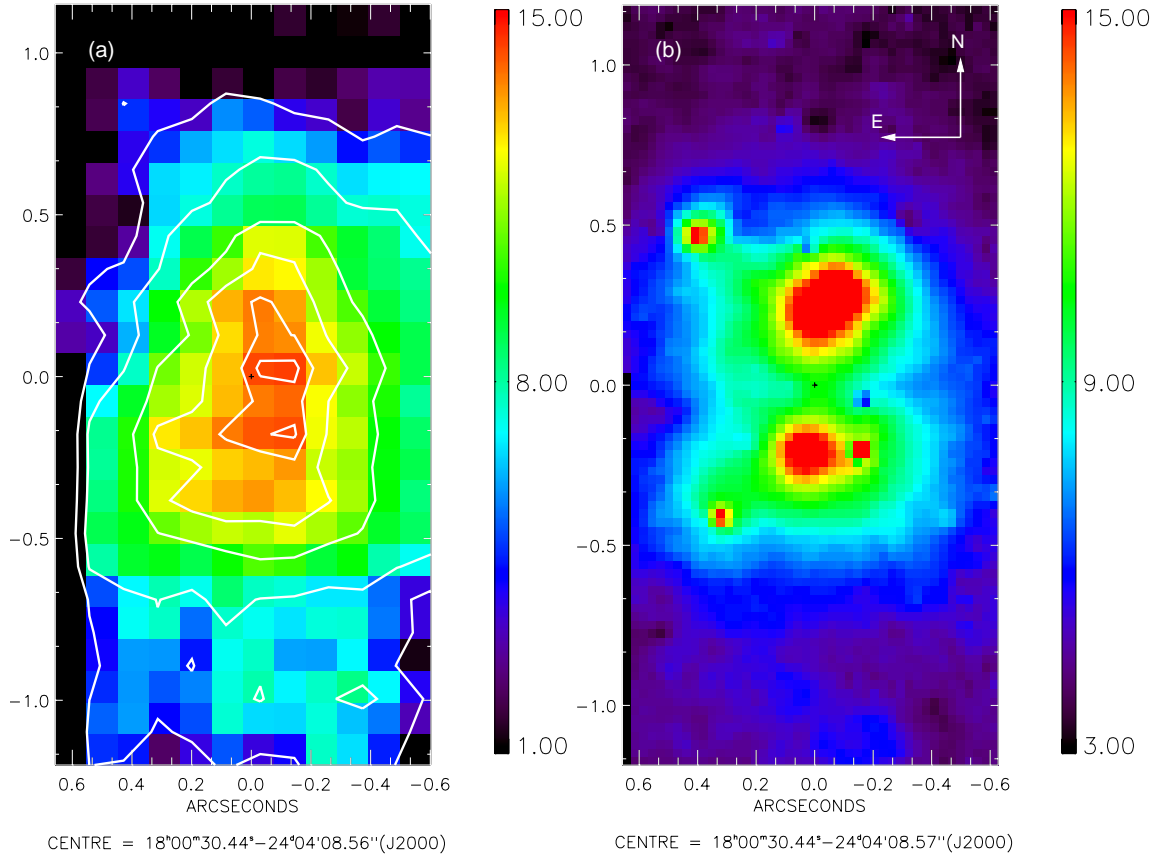
Figure 5.5: (a): Integrated image of the velocity channels at the location of the southern knot (A) obtained with ADONIS+Graf in arbitrary units. The original channels have been spatially smoothed with a box 5×5 pixels. The colourbar indicates the sigma-level over the background. Contours represent 3, 5, 8, 10, 12 and 13σ levels. b): NACO Ks-band image of the same field with a total exposure time of 600 s. The image is in logarithmic scale, ranging between 14 and 16 mJy/$\square''$.

G5.89+0.39, and referred to the local standard of rest (LSR). The calculation of the corrected radial velocity has made use of a velocity of the sun of 20 km s^{-1}, relative to the LSR. No systemic velocity has been subtracted due to the projected distance to the ionised nebula. It is then confirmed the pure H_2-line emission of this object that Feldt et al. (1999) addressed at lower resolution. The mosaic shows that the flux is dominant in the northern lobe for the radial velocities between $v_{LSR} = -90$ and $v_{LSR} = -50$ km s^{-1}, whereas the southern lobe becomes brighter between the $v_{LSR} = -30$ and $v_{LSR} = +10$ km s^{-1} velocity channels. This last value is coincident with the systemic velocity of the molecular cloud.

These blueshifted velocities with respect to the systemic one are compatible with the $C^{34}S$ observations (Cesaroni et al., 1991) and the H_2O maser emission (Hofner and Churchwell, 1996) (although not in absolute values), both on a larger scale ($\sim 10''$). The velocity gradient of 50 km s^{-1} present over a projected distance of ~ 900 AU with the lower limit at the

systemic velocity suggest that this object, ∼9500 AU south from G5.89-0.39 could be a non-resolved or asymmetric low velocity bow shock (Yu et al., 2000) in desceleration whose flow axis would pass over the UCHII (possibly close to the location of the already detected star). This hypothesis is consistent with the fact that no source has been detected at millimetric wavelengths at the location of this southern knot (Sollins et al., 2004), ruling out the existance of an independent source deeply embedded. Confirmation of this hypothesis would require the detection of a redshifted counter-shock, being the northern knot (C) a candidate, since according to the Ks-band NACO image, it is located at approximately 7.5″ to the north. The fact that no H_2 line emission has been detected in the Fabry-Perot observations at this location could be due to the low sensitivity of the data or to the non-sampling of the redshifted velocities (maximum velocity= $+30\,\mathrm{km\,s^{-1}}$). I conclude that the H_2 emission south of G5.89-0.39 (labeled as A-knot) can be justified by a bow shock produced by a jet/outflow whose origin could be located inside the ionised region. Mid-infrared spectroscopy could help to probe the suggested outflow activity, together with a high-resolution CO map.

5.3.3   Brγ-line velocity structure toward the UCHII

G5.89-0.39 was also observed in the Brγ-recombination line with Graf in the spectral range of 2.16459-2.16607 μm. The aim of these observations was to study the kinematics of the ionised material and its connection to the outflow or outflows.
Fig. 5.6 is a mosaic of nine velocity channels in the Brγ emission line of this UCHII, spatially smoothed with a median filter over a box of 5×5 pixels. The tenth channel has been considered as continuum and subtracted from every single frame. The velocities are referred to the Local Standard of Rest and need to be subtracted from a systemic velocity of ∼10 km s^{-1} (Cesaroni et al., 1991; Acord et al., 1997). In panel (j) the integrated image of the 11 velocity channels is shown, whereas panel (k) depicts the Ks-band NACO image of the same region, with a 3.7 times smaller pixelscale and a higher spatial resolution (FWHM=0″.13). Despite the fact that the NACO image in the Ks filter has a higher contribution from the continuum, the ADONIS+Graf image resembles quite well the structures observed at higher spatial resolution. In both images, the morphology of the emission is not that of the shell structure derived from the 2 cm VLA map. It shows a clear elongation in the northwest-southeast direction, already reported in other studies at 1.3 cm and NIR wavelengths (Gomez et al., 1991; Feldt et al., 1999). The extension to the south-east seems to have the origin at the location of the reported massive star (Feldt et al., 2003).
A single Gaussian was fitted to the cut along the velocity channels, for every spatial position, and the results are presented in Fig. 5.7. Panel (a) shows the centre of the fit (mean velocity), with the errors depicted in panel (c). The sigma of the Gaussian (i.e. the velocity dispersion) to the line profile is presented in panel (b) and its correspondent errors in panel (d).
The map of the mean velocity in Fig. 5.7(a) ranges between v$_{LSR}$ = −90 km s^{-1} and v$_{LSR}$ = +10 km s^{-1}, once the system velocity has been subtracted, with a mean value of v$_{LSR}$ = −27 km s^{-1}. The errors in the mean velocity are finally calculated by adding the corresponding variance from panel (c) and the error derived from the *phase shift calibration*. Finally, the errors can be as low as 4 km s^{-1} in the brightest regions.

The general structure of the velocity map is complicated. One substructure is immediately evident in the western side of the ionised material. This region shows a biconical morphology oriented in the north-west–south-east direction with an opening angle around 80 degrees and

a projected velocity that varies from -45 to 14 km s^{-1}.

The calculated velocity dispersion in Fig. 5.7(b) must still be corrected from the instrumental width and the thermal broadening in order to obtain the component of the velocity dispersion due to the turbulence. The natural width is considered negligible, compared to these two contributions. The instrumental broadening has been derived from the sigma of the krypton calibration line (1.7 km s^{-1}). According to the Maxwell-Boltzmann distribution for the velocities of atoms in an isothermal sphere, the velocity dispersion is derived from the expression (Binney and Tremaine, 1987; Osterbrock, 1989)

$$\sigma_{th} = \sqrt{\frac{k_B T}{m}} \qquad (5.5)$$

The thermal broadening of the velocity dispersion has been calculated using a typical value for the temperature of 10^4 K (Spitzer, 1978; Osterbrock, 1989), yielding a contribution of 9.1 km s^{-1}. The final velocity dispersion is given by

$$\sigma_{nth} = (\sigma_{obs}^2 - \sigma_{inst}^2 - \sigma_{th}^2)^{\frac{1}{2}} \qquad (5.6)$$

in Jiménez-Vicente et al. (1999), where σ_{obs} is the observed velocity dispersion, and σ_{inst} and σ_{th} are the instrumental and thermal dispersion, respectively.

The averaged velocity dispersion over the extension of the Brγ line emission of the nebula is 36 ± 17 km s^{-1}. This value is compatible with the expansion velocity calculated by Acord et al. (1998), that amounts 35 km s^{-1}. With this value, some physical parameters can be calculated, namely the energy, the momentum, and the dynamical age of the UCHII. For that purpose, the mass of the ionised gas was estimated by using the values of the diameter and U-parameter published by Wood and Churchwell (1989) on this source at 2 cm, after rescaling them to the adopted distance throughout this work (1.9 kpc). The equations presented in Mezger and Henderson (1967) are used for this conversion. The derived values are presented in Table 5.3.

The energy, momentum and dynamical age differ significantly between the CO outflow and the UCHII region. This difference has been proposed to be due to the fact that the outflow could have been driven before and the massive star formed later the ionised region (Okamoto et al., 2003b). The estimated dynamical age is consistent (whithin the errors) with that determined from VLA observations at 3.6 cm, over a time span of 5.3 yr (Acord et al., 1998). Considering the parameters derived from the 2 and 6 cm data in Wood and Churchwell (1989) (D= 1900 pc, $n_e = 27.72 \times 10^4 \, cm^{-3}$, $\log(N_{Lyc}) = 48.38$, angular diameter at half-power of $3\rlap{.}''85$), the dynamical age can be also calculated following the equations (5) and (9) of the same article. Assuming a density of the ambient cloud $\sim 10^5 \, cm^{-3}$ and a sound speed in the ionised gas $\sim 10 \, km \, s^{-1}$, the inferred age of G5.89-0.39 is $\sim$500 yr. Future observations in the H$_2$ shocked molecular lines will elucidate whether this new location of a possible outflow, apparently not connected to the already detected massive star, and if the already studied CO-outflow could be the result of the superimposition of several sources.

5.4 Conclusions

A high spectral and spatial resolution study of the kinematics of the outflow toward the shell-type UCHII region G5.89-0.39 has been presented. The symmetric morphology of this region has been originally considered an indicator of the presence of a central single massive star

with an evacuated cavitiy around it. The recent detection of an apparently massive star (O5) located off-centre (Feldt et al., 2003) and the extensively debated orientation of the outflow seems not compatible with the original simple picture. In this NIR kinematical study of the 0.1 pc surrounding region a possible connection between the massive outflow, the H_2 emission, the detected star and other possibly driving sources were analysed.

Long-slit spectroscopy of the unresolved knot A of H_2 emission $8''$ south from G5.89-0.39 revealed the shocked nature of this emission, while the Fabry-Perot data of this region in the same line revealed the presence of two knots of emission whose kinematical structure is compatible with a descelerating bow shock (average velocity$= -50\,\mathrm{km\,s^{-1}}$) with a possible origin in the UCHII region.

Fabry-Perot observations of the $Br\gamma$ line emission present in the HII region unveiled a biconical structure (P.A.$\sim 135°$), located to the west and not coincident with the previously detected star, with a remarkable velocity gradient between the two cones. This candidate of bipolar outflow can be suggestive of the presence of an undetected source within this UCHIIregion, departing from the unique and central source scenario. Deep L- and M-band imaging are needed to confirm this possibility. The averaged velocity dispersion derived from this Fabry-Perot data allowed a determination of the energy (1.7×10^{45} erg), momentum (4.63 $M_\odot$ km s^{-1}) and dynamical age (964 yr), this last being consistent with a former determination of Acord et al. (1998), based on measurements of the proper motion of the gas traced by radio emission.
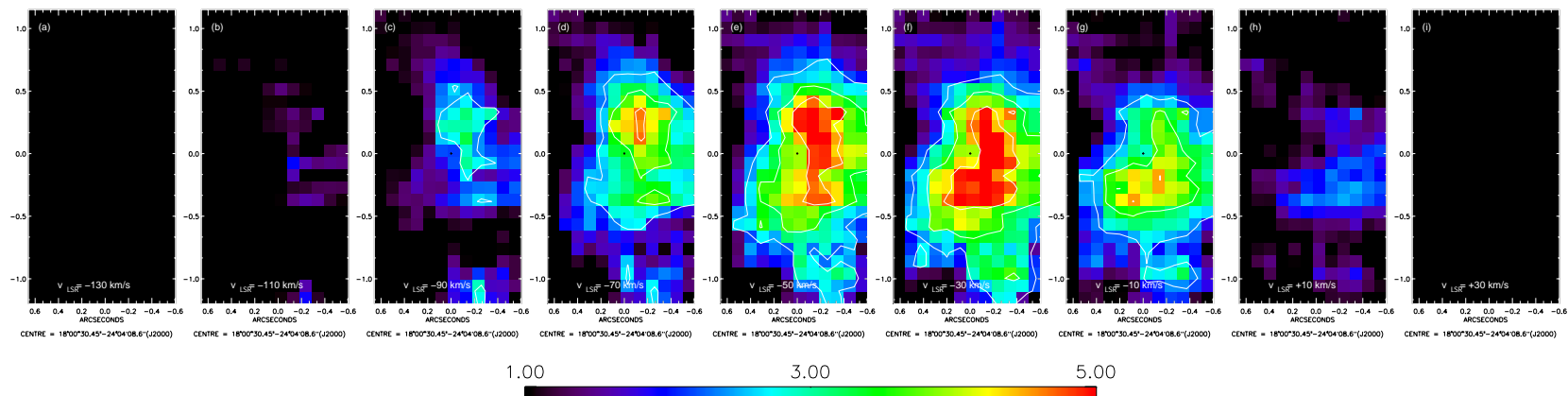
Table 5.2: Velocity channels in the H_2 v=1-0 S(1) line of the southern spot. The colourscale indicates the sigma level of the counts with respect to the background. White contours represent 2, 3 and 5σ levels.
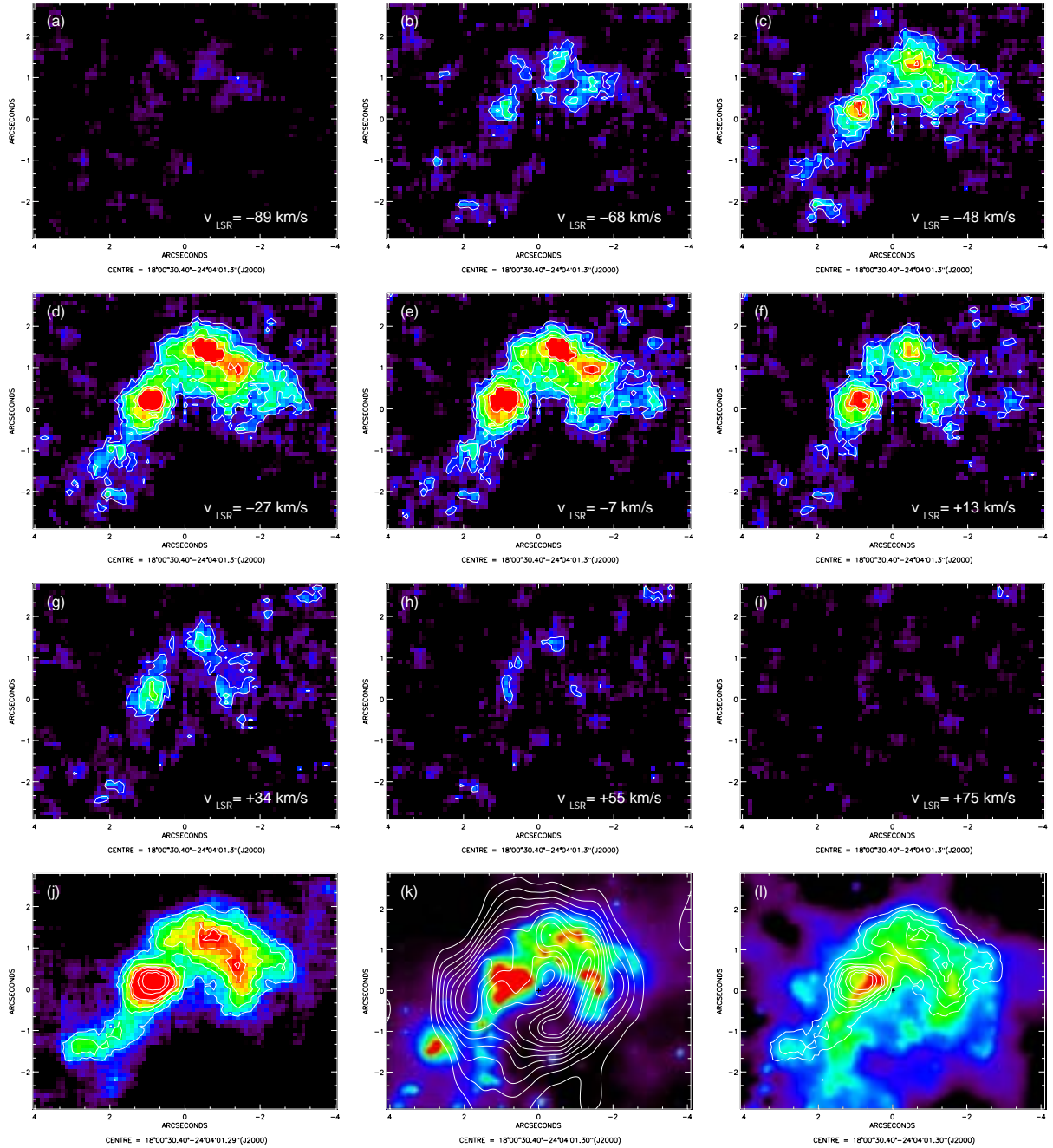
Figure 5.6: Panels (a) to (i) correspond to the velocity channels of the Brγ emission line, observed with Graf in count rates. White contours correspond to 2, 3, 4, 5, 6, 10 and 20 σ levels. The pixelscale is 0″1/pixel. The integrated emission, including the continuum, is presented in panel (j). Overlaying contours represent the 3, 5, 8, 10, 12 and 13 σ levels of the count rates. The panel (k) shows the same field in the Ks filter, obtained with NACO from Feldt et al. (2003). The logarithmic colourscale ranges from 14 to 21 mJy/□″. The 2 cm VLA map from Wood and Churchwell (1989) is represented by the contours at -0.06, -0.03, 0.03, 0.06, 0.09, 0.11, 0.14, 0.17, 0.20, 0.23, 0.26 and 0.27 Jy/beam. (l) shows the L emission in a logarithmic scale, as seen by NACO, with the colourscale range between 3 and 1783 mJy/□″.
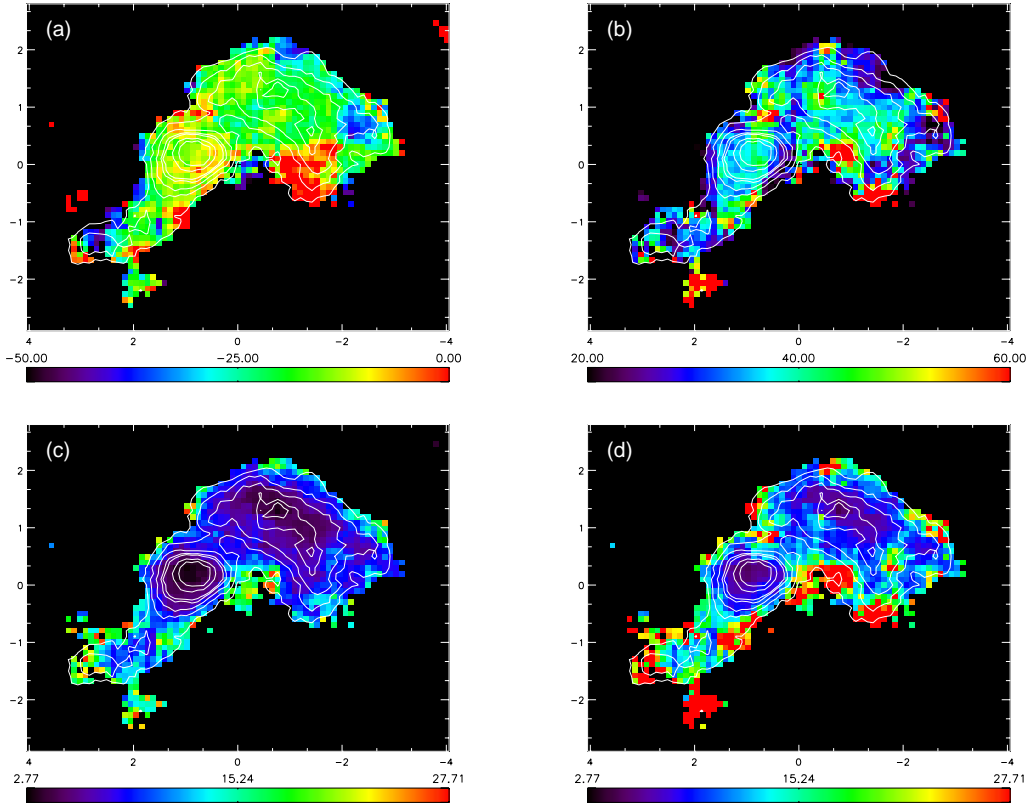
Figure 5.7: (a): Peak velocity of the fitted Gaussians to the 10 channels of the Brγ line. (c) errors in the peak position of the Gaussian, determined by Monte Carlo simulations. (b): FWHM of the fitted Gaussians and (d) errors in the determination of the FWHM. The locations with fitting errors above 27 km s^{-1} and count rates below the 3σ level of the background have been masked out. The colourbars indicate the scale in km s^{-1}. The white contours represent the total intensity, presented in panel (j) of Fig. 5.6

	Harvey and Forveille (1988)*	Acord et al. (1997)	This work
Energy= $\frac{1}{2}M_{ion}\sigma^2$ [erg]	8×10^{47}	-	$(1700\pm1.6) \times 10^{42}$
Momentum= $M_{ion}\sigma$ [M$_\odot$ km s^{-1}]	1600	-	4.63 ± 4.18
τ_{dyn}= r/σ [yr]	2000	600^{+250}_{-125}	964 ± 454

Table 5.3: Parameters of G5.89-0.39 derived from the radial velocity dispersion of the Brγ line.
* Outflow traced by CO observations.

Chapter 6

Summary and Future Work

This thesis work has been focused on the high resolution study of massive stars in UCHii, concentrating on two main aspects:(1) The identification and characterisation of the massive star/stars responsible of the Hiiregion by means of indirect methods as polarimetry, NIR recombination nebular lines and direct techniques such as the SED analysis and search of photospheric lines.(2) The dynamical nature of massive stars through one of the most morphologically simple UCHii, G5.89-0.09.

The main conclusions and remaining questions are summarised in the following, while an outline of the future work is also proposed.

6.1 Pinning Down the Ionising Star

Understanding the high-mass end of the IMF passes through the identification of the ionising stars during the UCHii-phase. The recent progress in the NIR detectors and the development of Adaptive Optics as an enhancement of the spatial resolution, contrast and sensitivity capabilities has opened a new window to understand the most compact phase of massive star formation. To date, this boom has translated into numerous examples of imaging photometry of UCHiis that are indeed limited by the uncertainty in the determined distance and the presence of colour excesses. The ionising sources are also dominant illuminators (if we only consider ZAMS stars) in a dusty environment, and therefore they can be spotted with NIR polarimetric maps and their characteristic centrosymmetric pattern. This indirect method has been used for the YSO S106 at a higher angular resolution than ever before and in the case of two UCHiis (G77.96-0.01 and G61.48+0.09). For G77.96-0.01, the star coincident with the radio continuum emission (♯11) is confirmed to be the main illuminator and likely the ionising source. However, the absence of a global centrosymmetric pattern in the reflection nebula indicates that also ♯45 can be an ionising source and that this multiple system would extend further than the radio continuum emission. This would be in good agreement with the proposed connection of the compact emission with the extended halo detected by Kurtz et al. (1999).

G61.48+0.09 is one of the best examples of complex UCHii regions in which one of the components could be externally ionised by the already detected stellar population. The combination of indirect and direct methods was aimed to determine the ionising source(s) responsible of this UCHii region. The NIR polarimetric map unveiled for the first time the presence of deeply embedded sources (later also detected in the L′ band), concluding that

both individual components of this UCHɪɪ harbour massive stars, highlighting a possible completeness problem of the stellar content. The use of high resolution observations at both NIR and radio wavelengths required a new approach to the treatment of the geometry of the ionised material, requiring an ionising source with spectral type as early as O5V. Combination of colour classification and the detection of a Brγ excess suggest the presence of an already evolved star (star 82) that could mimic into the ionising source responsible of one of the components (similar conclusions on two more UCHɪɪs are presented in (Alvarez et al., 2004)). Multiband spectroscopy is necessary to confirm this possibility. The presence of evolved massive stars (age $>10^7$ yr) could confirm the existence of a retarding evolution mechanism, already proposed by Wood and Churchwell (1989).

An attempt of classification of this same object through the analysis of the K-band photospheric lines around several sources was conducted with observations of a 4m-class telescope. The low signal-to-noise ratio of the observations and the embedded nature of the stars did not allow the detection of such features while the recombination nebular lines were strong enough to derive some rough properties from the line intensity ratios. Yet, the combination of all this information for G61.48+0.09 does not yield the confirmation of the ionising source, nor the univocal spectral classification of the ionising candidates.

I conclude that high-resolution and sensitive observations of UCHɪɪs are mandatory to better understand the massive stellar population, but still not enough to fully determine their physical parameters. Combination of several indirect and direct methods is still necessary and sometimes insufficient.

6.2   Dynamical structure of G5.89-0.09

The formation scenario of massive stars is still not completely understood, since the extrapolation of the low-mass formation mechanism of accretion is not able to theoretically justify the existence of the most massive stars. The detection of outflows/jets and discs constitute an observational evidence of accretion. The early stages of massive stars are especially indicated to seek for these structures.

G5.89-0.09 has one of the most powerful outflows in the Milky Way. Its apparently simple morphology has been always used as an indication of isolated massive star formation. Despite this symmetry, different kinematical studies do not agree with respect to the orientation of this massive outflow.

High spatial and spectral resolution techniques have helped tracing two different indicators of jet/outflow activity inside and in the surroundings of the ionised nebula. The analysis of the most prominent area of shocked molecular hydrogen is compatible with a north-south orientation of the outflow. The ionised material shows instead a biconical structure whose origin does not coincide with the previously detected star and a flow axis not compatible with the location of the shocked molecular hydrogen. This uncovered complexity of the dynamical structure in the NIR agrees with other studies in the mm and sub-mm range of similar regions, concluding that high resolution is mandatory to disentangle this confusion problem. The short dynamical age derived for G5.89-0.09 (964±454 yr) is consistent with the former estimate of Acord et al. (1998) and the theoretical expansion calculated from the radio data.

6.3   Future Work

It is obvious that the highly embedded nature of massive star formation poses a limitation on the completeness of the massive star content in UCHɪɪs. Hence, imaging and spectroscopy in L and M band will open the accessibility to the most embedded stars in these regions. High spatial resolution is then a *must* that becomes feasible with the development of NIR wavefront sensors in the field of Adaptive Optics. Examples like NACO at the VLT (southern hemisphere) and in the close future PYRAMIR at Calar Alto (northern hemisphere) offer a new possibility of coverage for high spatial resolution observations of deeply embedded objects. Surveys of UCHɪɪs at an unprecedented spatial resolution will cast more light on the massive tip of the IMF. The dynamical studies of massive stars in UCHɪɪs will soon profit from innovative instruments, performing in combination with Adaptive Optics techniques, such as the Fabry-Perot interferometer facility recently commissioned in NACO (R$\sim$1000) and the integral field spectrometer SPIFFI (R=2000-4000), operating together with a multi-conjugated Adaptive Optics system.

Appendix A

Appendix

The Determination of the Rate of Lyman Continuum Photons

The way to determine the number of Lyman continuum photons for the case of a ionised region starts with the equilibrium equation between photoionisation and recombination:

$$N_{H^0} \int_{\nu_0}^{\infty} \frac{F_\nu}{h\nu} a_\nu(H^0) d\nu = N_e N_p \alpha(H^0, T) \tag{A-1}$$

where N_{H^0} is the density of hydrogen, F_ν is the density flux, $a_\nu(H^0)$ is the photoionisation cross section of the hydrogen and $\alpha(H^0, T)$ is the recombination coefficient of the hydrogen. Since $F_\nu = \pi F_{ast\nu}$, the astrophisical flux at any distance r from the surface of the star is

$$F_{ast\nu}(r) = F_{ast\nu}(R) \frac{R^2}{r^2} e^{-\tau_\nu} \tag{A-2}$$

and Eq. A-1 translates into:

$$N_{H^0} \int_{\nu_0}^{\infty} \frac{\pi F_{ast\nu}(R)}{h\nu} \frac{R^2}{r^2} e^{-\tau_{nu}} a_\nu(H^0) d\nu = N_e N_p \alpha(H^0, T) \tag{A-3}$$

The optic depth at any radii of the nebula is $\tau_\nu = \int N_{H^0}(r) a_\nu(H^0) dr$, so then $\frac{d\tau_{nu}}{dr} = N_{H^0}(r) a_\nu(H^0)$ and subsituting in Eq. A-3 and integrating, we have

$$R^2 \int_{\nu_0}^{\infty} \frac{\pi F_{ast\nu}(R)}{h\nu} \int_0^{\infty} e^{-\tau_\nu d\nu} = \int_0^{\infty} N_e N_p \alpha(H^0, T) r^2 dr \tag{A-4}$$

inside the sphere $N_e = N_p = N_H$ and outside is 0, therefore the integration limits of r are $[0, r_1]$, and the expresion is

$$R^2 \int_{\nu_0}^{\infty} \frac{\pi F_{ast\nu}(R)}{h\nu} d\nu = \frac{1}{3} r_1^3 N_H^2 \alpha(H^0, T) \tag{A-5}$$

and since $Q(H^0) = \int \frac{L_\nu}{h\nu} d\nu$ and $L_\nu = 4\pi R^2 \pi F_{ast\nu}$, then

$$Q(H^0) = \frac{4\pi}{3} r_1^3 N_H^2 \alpha(H^0, T) = V N_H^2 \alpha(H^0, T) \tag{A-6}$$

When there is spherical symmetry one only needs the electron density and the volume of the sphere
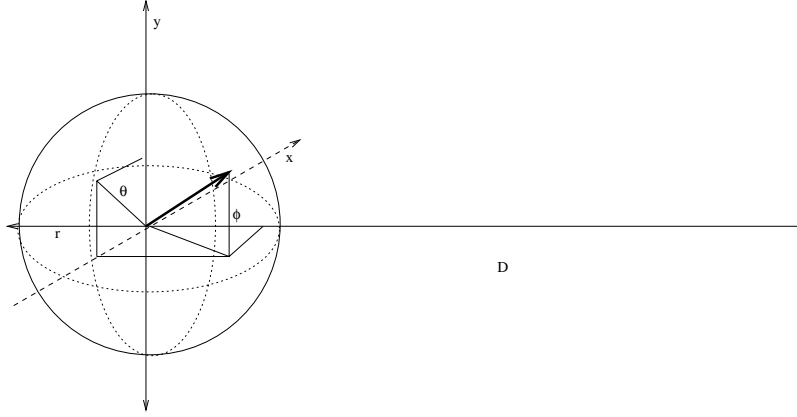
Figure A.1: Correspondence between coordinates (x, y, r) and (θ, ϕ) of any location inside the sphere.

The Electron Density of the Ionised Hydrogen in HII Regions

The brightness temperature describes the radiation emitted from a certain point and it is:

$$T_b = T_e(1 - e^{-\tau}) \approx T_e\tau \text{ for} \tau \ll 1 \tag{A-7}$$

The optical depth for free-free emission is:

$$\tau = 8.235 \times 10^{-2} \left(\frac{T_e}{K}\right)^{-1.35} \left(\frac{\nu}{GHz}\right)^{-2.1} \left(\frac{\int N_e^2 dr}{pc \cdot cm^{-6}}\right) \tag{A-8}$$

The last term of the equation is the **emission measure**. Now, instead of cartesian coordinates (x, y, r) we will use apparent angles

$$\theta = (x^2 + y^2)^{1/2}/D; \quad \phi = r/D \tag{A-9}$$
$$\tag{A-10}$$

Using Eq. A-7 in Eq. A-8 one can relate the emission measure with the brightness temperature, which is the measurable variable. The relation between the antenna temperature T_A and the brightness temperature T_b leads to the expression

$$\frac{2\pi}{\Omega_m} \int \theta d\theta f(\theta) \int N_0^2(\theta, \phi)d\phi = \frac{T_A}{82.35a\eta_B} \left(\frac{T_e}{K}\right)^{0.35} \left(\frac{D}{kpc}\right)^{-1} \left(\frac{\nu}{GHz}\right)^{2.1} \tag{A-11}$$

where Ω_m, η_B are parameters of the antenna and a is a correction factor for the approximation of τ (the optical depth). At this point, in order to integrate the second integral, we need to assume a geometrical model an certain conditions:

- A spherical, cilindric or exponential geometry

- A constant density inside the geometry

With this two conditions is possible to make the integral. Lets say we take the spherical model, then the integral

$$\int_{-\sqrt{\left(\frac{\theta_{sph}}{2}\right)^2-\theta^2}}^{+\sqrt{\left(\frac{\theta_{sph}}{2}\right)^2-\theta^2}} N^2(\theta,\phi)d\phi = N_0\theta_{sph}\sqrt{1-4\theta^2/\theta_{sph}^2} = N_0\theta_{sph}\psi_s(\theta) \qquad \text{(A-12)}$$

and this last function $\psi_s(\theta)$, together with the first integral of Eq. A-11 is the modified solid angle subtended by the source on the sky(see Fig. A).

$$\Omega_s = \int 2\pi\theta d\theta\psi(\theta) \text{ where } \psi(\theta) = \cos\alpha = \frac{\phi}{\theta_{sph}/2} = \sqrt{1 - \frac{\theta^2}{(\theta_{sph}/2)^2}} \text{(A-13)}$$
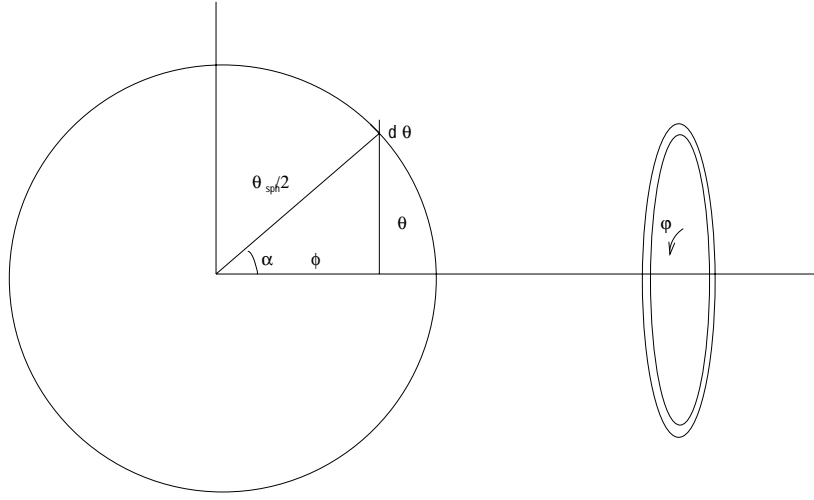
Figure A.2:

For a sphere of radius $\theta_{sph}/2$, $\Omega_s = \frac{\pi}{6}\theta_{sph}^2$, for a wedge of angle φ_0, the solid angle $\Omega_s = \frac{\varphi_0}{3}\left(\frac{\theta_{sph}}{2}\right)^2$, and for the intersection of a wedge with a cut along the ϕ direction (see Fig. A)

$$\Omega_s = \frac{\varphi_0}{\theta_{sph}/2}\left[\frac{\left(\left(\frac{\theta_{sph}}{2}\right)^2-\theta_{int}^2\right)^{3/2}}{3} - \frac{\left(\left(\frac{\theta_{sph}}{2}\right)^2-\theta_{ext}^2\right)^{3/2}}{3}\right] \qquad \text{(A-14)}$$

Finally, the introduction of the relation between the Antenna temperature and the flux density yields the density as it appears in most places

$$\left(\frac{N_0}{cm^{-3}}\right) = u_1 a^{1/2} 6.351 \times 10^2 \left(\frac{T_e}{10^4 K}\right)^{0.175} \left(\frac{\nu}{GHz}\right)^{0.05} \left(\frac{S_\nu}{Jy}\right)^{-0.5} \left(\frac{\theta_G}{arcmin}\right)^{-1.5} \qquad \text{(A-15)}$$

The factor u_1 depends directly on the solid angle subtended by the source on the sky. The excitation parameter $U = rN_0^{2/3}$ is independent of the source size, but not of the geometry. For a sphere, this is $\sqrt{\frac{6}{\pi}}\left(\frac{1}{1.471}\right)^{\frac{3}{2}}$.
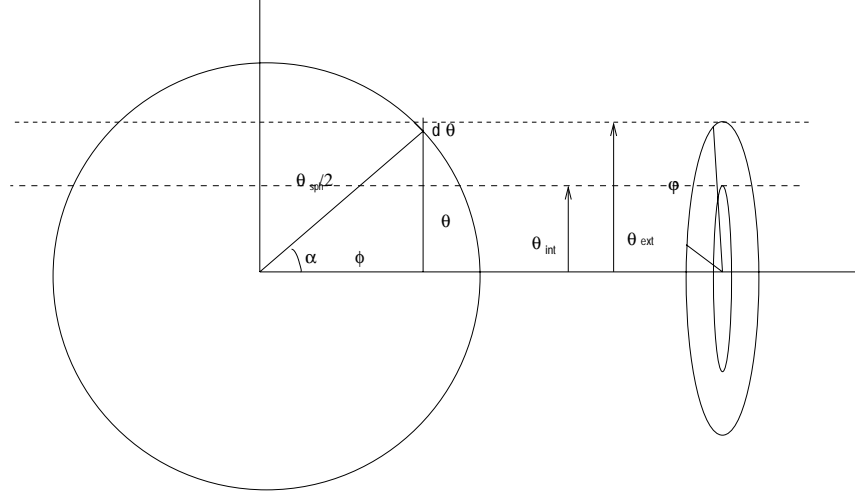
Figure A.3:

Using One Wedge of the Radio Map

The equation that Kurtz et al. (1994) propose in the paper, includes the spherical model in its factors already. The geometrical factors, once the density is introduced vanish and therefore there is no dependence on the geometry if one uses the volume and solid angle of the same object (i.e. a sphere, a cylinder, a wedge). Using the solid angle of a part to determine the electron density and then the volume of the whole sphere makes that the geometrical dependency does not simplify and then we will have some geometrical factor in the final Lyman continuum photons.

In the case of shells, the emission varies so much that authors have considered that they only must take the casquet of the sphere corresponding to the shell into account to calculate the electron density. From the depth of the sphere on the line of sight $(\Delta s = 2\sqrt{r_0^2 - r_i^2})$ obtain the electron density and then, the radiation will not be averaged, they only take the parts where it seems to be constant and strong. Also Garay et al. (1993) used the same technique. We use the wedge to determine the number of Lyman continuum photons that are passing through it. Since this is only one part of what the star emits, we need to rescale the value by a certain factor. To do that, we know that the radiation from an element of surface dA is

$$L_\lambda d\lambda = \int_{\phi=0}^{2\pi} \int_{\theta=0}^{\pi/2} \int_A I_\lambda d\lambda dA \cos\theta \sin\theta d\theta d\phi \qquad (A-16)$$

The factor $cos\theta$ appears because the net density flux is the component perpendicular to the surface. The integral of the components tangent to the surface will be 0. In order to compare the luminosity of the wedge with the total luminosity we integrate Eq. A-16 for the two cases. For the total luminosity, the limits for the solid angle will be $\int_{\phi=0}^{2\pi} \int_{\theta=0}^{\pi/2}$ and for the area $\int_{\phi=0}^{2\pi} \int_{\theta=0}^{\pi}$. For the wedge, the solid angle integrates over the whole hemisphere and the are integrates over $\int_{\phi=0}^{\phi_0} \int_{\theta=0}^{\pi}$. The ratio between the two luminosities is
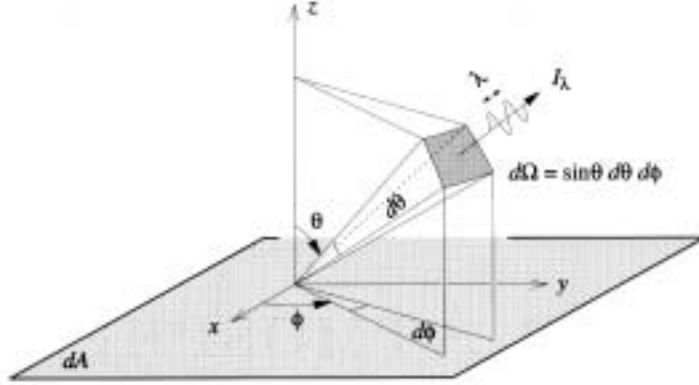
Figure 9.1 Intensity I_λ.

$$\frac{L_{tot\lambda}d\lambda}{L_{wed\lambda}d\lambda} = \frac{4\pi^2 R^2 I_\lambda d\lambda}{\pi\phi_0 I_\lambda d\lambda} = \frac{2\pi}{\phi} \tag{A-17}$$

Then, this is the factor to rescale the number of Lyman continuum photons measured over only one wedge, in order to obtain the total number of Lyman continuum photons emitted by the star.

In the case described by Fig. A, the factor to multiply the number of Lyman continuum photons, obtained by measuring the flux density on a wedge of angle φ_0 with internal radius θ_{int} and external radius θ_{ext}, for is

$$factor = \frac{2\pi}{\varphi_0 \left[\left(1 - \frac{\theta_{in}^2}{\left(\frac{\theta_G}{2}\right)^2}\right)^{3/2} - \left(1 - \frac{\theta_{ext}^2}{\left(\frac{\theta_G}{2}\right)^2}\right)^{3/2} \right]} \tag{A-18}$$

Bibliography

Acord, J. M., Churchwell, E., and Wood, D. O. S. (1998). The Expansion Rate and Distance to G5.89-0.39. *ApJ*, 495:L107.

Acord, J. M., Walmsley, C. M., and Churchwell, E. (1997). The Extraordinary Outflow toward G5.89-0.39. *ApJ*, 475:693.

Allen, D. A. and Penston, M. V. (1975). Infrared sources in obscured regions. *MNRAS*, 172:245–248.

Alvarez, C., Feldt, M., Henning, T., Puga, E., and Brandner, W. (2004). in press. *A&A*.

Argon, A. L., Reid, M. J., and Menten, K. M. (2000). Interstellar Hydroxyl Masers in the Galaxy. I. The VLA Survey. *ApJS*, 129:159–227.

Armand, C., Baluteau, J.-P., Joubert, M., Gry, C., and Cox, P. (1996). The near-infrared spectrum of ultracompact HII regions. *A&A*, 306:593.

Aspin, C., McLean, I. S., Schwarz, H. E., and McCaughrean, M. J. (1989). Ccd observations of bipolar nebulae. *A&A*, 221:100–104.

Aspin, C., Rayner, T. J. McLean, I. S., and Hayashi, S. S. (1990). Infrared imaging polarimetry and photometry of s106. *MNRAS*, 246:565–575.

Bally, J. and Scoville, N. Z. (1982). Structure and evolution of molecular clouds near H II regions. II - The disk constrained H II region, S106. *ApJ*, 255:497–509.

Bally, J., Yu, K., Rayner, J., and Zinnecker, H. (1998). Hubble Space Telescope Wide Field Planetary Camera 2 Observations of the Young Bipolar H II Region S106. *AJ*, 116:1868–1881.

Bastien, P. and Menard, F. (1988). On the interpretation of polarization maps of young stellar objects. *ApJ*, 326:334–338.

Bastien, P. and Menard, F. (1990). Parameters of disks around young stellar objects from polarization observations. *ApJ*, 364:232–241.

Beuther, H., Schilke, P., Sridharan, T. K., Menten, K. M., Walmsley, C. M., and Wyrowski, F. (2002). Massive molecular outflows. *A&A*, 383:892–904.

Beuzit, J., Hubin, N., Gendron, E., Demailly, L., Gigan, P., Lacombe, F., Chazallet, F., Rabaud, D., and Rousset, G. (1994). ADONIS: a user-friendly adaptive optics system for the ESO 3.6-m telescope. In *Proc. SPIE Vol. 2201, p. 955-961, Adaptive Optics in Astronomy, Mark A. Ealey; Fritz Merkle; Eds.*, pages 955–961.

Bik, A., Kaper, L., Hanson, M. M., and Comerón, F. (2002). The Stellar Population of Ultracompact HII Regions: the Case of IRAS 10049-5657. In *ASP Conf. Ser. 267: Hot Star Workshop III: The Earliest Phases of Massive Star Birth*, page 343.

Bik, A., Lenorzer, A., Kaper, L., Comerón, F., Waters, L. B. F. M., de Koter, A., and Hanson, M. M. (2003). Identification of the ionizing source of NGC 2024. *A&A*, 404:249–254.

Binney, J. and Tremaine, S. (1987). *Galactic dynamics*. Princeton, NJ, Princeton University Press, 1987, 747 p.

Black, J. H. and van Dishoeck, E. F. (1987). Fluorescent excitation of interstellar H2. *ApJ*, 322:412–449.

Blitz, L. (1993). Giant molecular clouds. In *Protostars and Planets III*, pages 125–161.

Brandner, W. and Potter, D. (2002). High-Contrast Imaging Science with Adaptive Optics. In *Scientific Drivers for ESO Future VLT/VLTI Instrumentation Proceedings of the ESO Workshop held in Garching, Germany, 11-15 June, 2001. p. 264.*, pages 264–+.

Burton, M. G., Hollenbach, D. J., and Tielens, A. G. G. (1992). Mid-infrared rotational line emission from interstellar molecular hydrogen. *ApJ*, 399:563–572.

Cesaroni, R., Walmsley, C. M., Koempe, C., and Churchwell, E. (1991). Molecular clumps associated with ultra compact H II regions. *A&A*, 252:278–290.

Chalabaev, A., Le Coarer, E., Le Mignant, D., Rabou, P., Petmezakis, P., and Mignart, Y. (2003). Spectroscopy with adaptive optics: example and quality of GraF data. In *Instrument Design and Performance for Optical/Infrared Ground-based Telescopes. Edited by Iye, Masanori; Moorwood, Alan F. M. Proceedings of the SPIE, Volume 4841, pp. 382-389 (2003).*, pages 382–389.

Chandrasekhar, S. (1950). *Radiative transfer*. Oxford, Clarendon Press, 1950.

Churchwell, E. and Bieging, J. H. (1982). CN line emission from the molecular clouds associated with S106 and and NGC 7538. *ApJ*, 258:515–532.

Clarke, D., Stewart, B. G., Schwarz, H. E., and Brooks, A. (1983). The statistical behaviour of normalized Stokes parameters. *A&A*, 126:260–264.

Depoy, D. L. and Shields, J. C. (1994). The He I 2.06 micron to BR gamma ratio in 12 planetary nebulae. *ApJ*, 422:187–192.

Draine, B. T. and Bertoldi, F. (1996). Structure of Stationary Photodissociation Fronts. *ApJ*, 468:269.

Eiroa, C., Elasser, H., and Lahulla, J. F. (1979). Excitation and nature of the bipolar nebula S 106. *A&A*, 74:89–92.

Evans, N. J. (1999). Physical Conditions in Regions of Star Formation. *ARA&A*, 37:311–362.

Faison, M., Churchwell, E., Hofner, P., Hackwell, J., Lynch, D. K., and Russell, R. W. (1998). Infrared Spectroscopy of Ultracompact H II Regions. *ApJ*, 500:280.

Feldt, M., Puga, E., Lenzen, R., Henning, T., Brandner, W., Stecklum, B., Lagrange, A.-M., Gendron, E., and Rousset, G. (2003). Discovery of a Candidate for the Central Star of the Ultracompact H II Region G5.89-0.39. *ApJ*, 599:L91–L94.

Feldt, M., Puga, E., Weiß, A. R., and Hippler, S. (2002). The Massive Star Forming Region S106. In *ASP Conf. Ser. 267: Hot Star Workshop III: The Earliest Phases of Massive Star Birth*, page 367.

Feldt, M., Stecklum, B., Henning, T., Hayward, T. L., Lehmann, T., and Klein, R. (1998). The ultracompact H II region G45.45+0.06. A pearl necklace in the sky. *A&A*, 339:759–772.

Feldt, M., Stecklum, B., Henning, T., Launhardt, R., and Hayward, T. L. (1999). High-resolution imaging of ultracompact H II regions regions. II. G5.89-0.39 revisited. *A&A*, 346:243–259.

Felli, M., Massi, M., Staude, H. J., Reddmann, T., Eiroa, C., Hefele, H., Neckel, T., and Panagia, N. (1984). High spatial resolution observations of S 106 from lambda = 0.6 micron to lambda = 1.3 CM - A wind model for the bipolar nebula. *A&A*, 135:261–280.

Fischer, O., Henning, T., and Yorke, H. W. (1994). Simulation of polarization maps. 1: Protostellar envelopes. *A&A*, 284:187–209.

Fischer, O., Henning, T., and Yorke, H. W. (1996). Simulation of polarization maps. II. The circumstellar environment of pre-main sequence objects. *A&A*, 308:863–885.

Franco, J., Kurtz, S. E., García-Segura, G., and Hofner, P. (2000). The Evolution of HII Regions. *Ap&SS*, 272:169–179.

Garay, G., Gomez, Y., Lizano, S., and Brown, R. L. (1998a). VLA Observations of Carbon Radio Recombination Lines toward the H II Region Complex S88B. *ApJ*, 501:699.

Garay, G. and Lizano, S. (1999). Massive Stars: Their Environment and Formation. *PASP*, 111:1049–1087.

Garay, G., Lizano, S., Gomez, Y., and Brown, R. L. (1998b). VLA Observations of Hydrogen and Helium Recombination Lines from Partially and Fully Ionized Gas in S88B. *ApJ*, 501:710.

Garay, G., Rodriguez, L. F., Moran, J. M., and Churchwell, E. (1993). VLA Observations of Strong IRAS Point Sources Associated with Compact H II Regions. *ApJ*, 418:368.

Gehrz, R. D., Grasdalen, G. L., Castelaz, M., Gullixson, C., Mozurkewich, D., and Hackwell, J. A. (1982). ,Anatomy of a region of star formation - Infrared images of S106 /AFGL 2584/. *ApJ*, 254:550–561.

Gomez, Y., Rodriguez, L. F., Garay, G., and Moran, J. M. (1991). The dense molecular envelope around the compact H II region G5.89 - 0.39 (W28 A2). *ApJ*, 377:519–525.

Gordon, S., Koribalski, B., Houghton, S., and Jones, K. (2000). A guide to TAURUS-2 Fabry-Perot data reduction. *MNRAS*, 315:248–262.

Hanson, M. M., Conti, P. S., and Rieke, M. J. (1996). A Spectral Atlas of Hot, Luminous Stars at 2 Microns. *ApJS*, 107:281.

Hanson, M. M., Luhman, K. L., and Rieke, G. H. (2002a). A Near-Infrared Survey of Radio-selected Ultracompact H II Regions. *ApJS*, 138:35–61.

Hanson, M. M., Luhman, K. L., and Rieke, G. H. (2002b). A Near-Infrared Survey of Radio-selected Ultracompact H II Regions. *ApJS*, 138:35–61.

Hartung, M. E. (2003). *Commissioning of the Adaptive Optics System NAOS-CONICA for the VLT*. PhD thesis.

Harvey, P. M. and Forveille, T. (1988). A remarkable molecular outflow in W28. *A&A*, 197:L19–L21.

Harvey, P. M., Lester, D. F., Colome, C., Smith, B., Monin, J., and Vauglin, I. (1994). G5.89-0.39: A compact H II region with a very dense circumstellar dust torus. *ApJ*, 433:187–198.

Hecht, E. and Zajac, A. (1974). *Optics*. Addison-Wesley Series in Physics, Reading, Mass.: Addison-Wesley, 1974.

Henning, T., Feldt, M., and Stecklum, B. (2002). High-Resolution Studies of Massive Star-Forming Regions. In *ASP Conf. Ser. 267: Hot Star Workshop III: The Earliest Phases of Massive Star Birth*, page 153.

Hoare, M. G., Drew, J. E., Muxlow, T. B., and Davis, R. J. (1994). Mapping the radio emission from massive young stellar objects. *ApJ*, 421:L51–L54.

Hoare, M. G. and Muxlow, T. B. (1996). MERLIN Observations of Luminous Young Stellar Objects. In *ASP Conf. Ser. 93: Radio Emission from the Stars and the Sun*, page 47.

Hodapp, K.-W. (1984). Infrared polarization of sources with bipolar mass outflow. *A&A*, 141:255–262.

Hofner, P. and Churchwell, E. (1996). A survey of water maser emission toward ultracompact HII regions. *A&AS*, 120:283–299.

Jiménez-Vicente, J., Battaner, E., Rozas, M., Castañeda, H., and Porcel, C. (1999). Fabry-Perot observations of the ionized gas in NGC 3938. *A&A*, 342:417–425.

Kaper, L., Bik, A., Hanson, M. M., and Comerón, F. (2002a). The Infancy of Massive Stars: Looking into the Cradle. In *ASP Conf. Ser. 267: Hot Star Workshop III: The Earliest Phases of Massive Star Birth*, page 95.

Kaper, L., Bik, A., Hanson, M. M., and Comerón, F. (2002b). VLT/ISAAC Spectroscopy of Young Massive Stars Embedded in Ultra-Compact H ii Regions. In *The Origins of Stars and Planets: The VLT View. Proceedings of the ESO Workshop held in Garching, Germany, 24-27 April 2001, p. 291.*, page 291.

Kasper, M. E., Looze, D. P., Hippler, S., Feldt, M., Weiss, R., Glindemann, A., and Davies, R. I. (2000). Practical approach to modal basis selection and wavefront estimation. In *Proc. SPIE Vol. 4007, p. 592-599, Adaptive Optical Systems Technology, Peter L. Wizinowich; Ed.*, pages 592–599.

Kim, K. and Koo, B. (1996). VLA Radio Continuum Observations of the Extended Envelopes Surrounding 16 UC HII Regions. *Journal of the Korean Astronomical Society, v. 29 Supplement,, p.S177*, 29:177.

Kim, S., Martin, P. G., and Hendry, P. D. (1994). The size distribution of interstellar dust particles as determined from extinction. *ApJ*, 422:164–175.

Koo, B., Kim, K., Lee, H., Yun, M., and Ho, P. T. P. (1996). The H II Region Complex G5.48-0.24: Radio Continuum, H i, and CO Observations. *ApJ*, 456:662.

Kruegel, E. (2003). *The physics of interstellar dust*. The physics of interstellar dust, by Endrik Kruegel. IoP Series in astronomy and astrophysics, ISBN 0750308613. Bristol, UK: The Institute of Physics, 2003.

Kudritzki, R.-P., Hummer, D. G., Pauldrach, A. W. A., Puls, J., Najarro, F., and Imhoff, J. (1992). Radiation-driven winds of hot luminous stars. X - The determination of stellar masses, radii and distances from terminal velocities and mass-loss rates. *A&A*, 257:655–662.

Kumar, M. S. N., Fernandes, A. J. L., Hunter, T. R., Davis, C. J., and Kurtz, S. (2003). A massive disk/envelope in shocked H_2 emission around an UCHII region. *A&A*, 412:175–184.

Kurtz, S., Churchwell, E., Wood, D. O. S., and Myers, P. (1994). Ultracompact HII Regions: A Molecular Point of View. *Bulletin of the American Astronomical Society*, 26:907.

Kurtz, S. and Franco, J. (2002). Ultracompact H II Regions. In *Revista Mexicana de Astronomia y Astrofisica Conference Series*, pages 16–21.

Kurtz, S. E., Watson, A. M., Hofner, P., and Otte, B. (1999). Ultracompact H II Regions with Extended Radio-Continuum Emission. *ApJ*, 514:232–248.

Lacasse, M. G., Boyle, D., Pipher, J. L., Sharpless, S., and Levreault, R. (1981). Polarimetric observations of S 106. *A&A*, 104:57–64.

Lada, C. J. (1991). The Formation of Low Mass Stars: Observations. In *NATO ASIC Proc. 342: The Physics of Star Formation and Early Stellar Evolution*, page 329.

Larson, R. B. (1982). Mass spectra of young stars. *MNRAS*, 200:159–174.

Lenzen, R., Bizenberger, P., Salm, N., and Storz, C. (1998). Omega Cass: a new multimode NIR-imager/spectrometer for the Calar Alto Observatory. In *Proc. SPIE Vol. 3354, p. 493-499, Infrared Astronomical Instrumentation, Albert M. Fowler; Ed.*, pages 493–499.

Lucas, P. W. and Roche, P. F. (1997). Butterfly star in Taurus: structures of young stellar objects. *MNRAS*, 286:895–919.

Lucas, R., Encrenaz, P. J., Le Squeren, A. M., and Kazes, I. (1978). Molecular observations of Sharpless 106. *A&A*, 66:155–160.

Lumsden, S. L., Puxley, P. J., Hoare, M. G., Moore, T. J. T., and Ridge, N. A. (2003). Helium and hydrogen line ratios and the stellar content of compact HII regions. *MNRAS*, 340:799–812.

Martín-Hernández, N. L., Bik, A., Kaper, L., Tielens, A. G. G. M., and Hanson, M. M. (2003). A VLT spectroscopic study of the ultracompact H II region G29.96-0.02. *A&A*, 405:175–188.

Martín-Hernández, N. L., Peeters, E., Morisset, C., Tielens, A. G. G. M., Cox, P., Roelfsema, P. R., Baluteau, J.-P., Schaerer, D., Mathis, J. S., Damour, F., Churchwell, E., and Kessler, M. F. (2002). ISO spectroscopy of compact H II regions in the Galaxy. II. Ionization and elemental abundances. *A&A*, 381:606–627.

Mezger, P. G. and Henderson, A. P. (1967). Galactic H II Regions. I. Observations of Their Continuum Radiation at the Frequency 5 GHz. *ApJ*, 147:471.

Miralles, M. P., Rodriguez, L. F., and Scalise, E. (1994). Radio continuum, ammonia, and water maser observations of bright, unassociated IRAS point sources. *ApJS*, 92:173–188.

Naghizadeh-Khouei, J. and Clarke, D. (1993). On the statistical behaviour of the position angle of linear polarization. *A&A*, 274:968.

Okamoto, Y. K., Kataza, H., Yamashita, T., Miyata, T., and Onaka, T. (2001). High-Resolution Mid-Infrared Imaging and Spectroscopic Observations of a Massive Star Forming Region W51 IRS 2. *ApJ*, 553:254–266.

Okamoto, Y. K., Kataza, H., Yamashita, T., Miyata, T., Sako, S., Honda, M., Onaka, T., and Fujiyoshi, T. (2003a). [NEII] Line Velocity Structure of Ultracompact HII Regions. In *IAU Symposium*.

Okamoto, Y. K., Kataza, H., Yamashita, T., Miyata, T., Sako, S., Takubo, S., Honda, M., and Onaka, T. (2003b). K3-50A: An Ultracompact H II Region Ionized by a Massive Stellar Cluster. *ApJ*, 584:368–384.

Oliva, E. and Moorwood, A. F. M. (1986). Infrared objects near H2O masers in regions of active star formation. IV - Molecular hydrogen observations. *A&A*, 164:104–115.

Osterbrock, D. E. (1989). *Astrophysics of gaseous nebulae and active galactic nuclei.* Research supported by the University of California, John Simon Guggenheim Memorial Foundation, University of Minnesota, et al. Mill Valley, CA, University Science Books, 1989, 422 p.

Pendleton, Y. J., Tielens, A. G. G. M., and Werner, M. W. (1990). Studies of dust grain properties in infrared reflection nebulae. *ApJ*, 349:107–119.

Persson, S. E., Campbell, B., and McGregor, P. J. (1988). High spatial and spectral resolution observations of the optical counterparts of GL 490 and S106/IRS 3. *ApJ*, 326:339–355.

Pipher, J. L., Sharpless, S., Kerridge, S. J., Krassner, J., Schurmann, S., Merrill, K. M., Savedoff, M. P., and Soifer, B. T. (1976). Optical, infrared and radio studies of compact H II regions. I - The complex in S 106. *A&A*, 51:255–262.

Pratap, P., Megeath, S. T., and Bergin, E. A. (1999). High-Angular Resolution Millimeter-Wave and Near-Infrared Imaging of the Ultracompact H II Region G29.96-0.02. *ApJ*, 517:799–818.

Richer, J. S., Padman, R., Ward-Thompson, D., Hills, R. E., and Harris, A. I. (1993). The molecular environment of s106 ir. *MNRAS*, 262:839–854.

Rodríguez-Rico, C. A., Rodríguez, L. F., and Gómez, Y. (2002). Radio Continuum and H92 α Recombination Line Observations of G34.26+0.15 and G5.89-0.39. *Revista Mexicana de Astronomia y Astrofisica*, 38:3–11.

Shu, F., Najita, J., Galli, D., Ostriker, E., and Lizano, S. (1993). The collapse of clouds and the formation and evolution of stars and disks. In *Protostars and Planets III*, pages 3–42937.

Shu, F. H., Adams, F. C., and Lizano, S. (1987). Star formation in molecular clouds - Observation and theory. *ARA&A*, 25:23–81.

Sibille, F., Bergeat, J., Lunel, M., and Kandel, R. (1975). Infrared observations of Sharpless 2-106, a possible location for star formation. *A&A*, 40:441–446.

Simmons, J. F. L. and Stewart, B. G. (1985). Point and interval estimation of the true unbiased degree of linear polarization in the presence of low signal-to-noise ratios. *A&A*, 142:100–106.

Solf, J. and Carsenty, U. (1982). The kinematical structure of the bipolar nebula S106. *A&A*, 113:142–149.

Sollins, P. K., Hunter, T. R., Battat, J., Beuther, H., Ho, P. T. P., Lim, J., Liu, S. Y., Ohashi, N., Sridharan, T. K., Su, Y. N., Zhang, Q., and Zhao, J. H. (2004). Mapping the Outflow from G5.89-0.39 in SiO(5-4). *American Astronomical Society Meeting*, 204.

Spitzer, L. (1978). *Physical processes in the interstellar medium.* New York Wiley-Interscience, 1978. 333 p.

Stecklum, B., Henning, T., Feldt, M., Hayward, T. L., Hoare, M. G., Hofner, P., and Richter, S. (1998). The ultracompact H II region G5.97-1.17 - an evaporating circumstellar disk in M8. *AJ*, 115:767.

Stutzki, J., Ungerechts, H., and Winnewisser, G. (1982). NH3 and H2O in the S106 molecular cloud. *A&A*, 111:201–208.

Takahashi, H., Matsuhara, H., Watarai, H., and Matsumoto, T. (2000). [NE II] 12.8 Micron Images of Four Galactic Ultracompact H II Regions: Ionized Neon Abundance as a Tracer of the Ionizing Stars. *ApJ*, 541:779–790.

Tamura, M., Gatley, I., Joyce, R. R., Ueno, M., Suto, H., and Sekiguchi, M. (1991). Infrared polarization images of star-forming regions. I - The ubiquity of bipolar structure. *ApJ*, 378:611–627.

Turner, B. E., Balick, B., Cudaback, D. D., Heiles, C., and Boyle, R. J. (1974). Fine structure in H II regions. II. *ApJ*, 194:279–291.

Wardle, J. F. C. and Kronberg, P. P. (1974). The linear polarization of quasi-stellar radio sources at 3.71 and 11.1 centimeters. *ApJ*, 194:249–255.

Watson, A. M. and Hanson, M. M. (1997). Near-Infrared Spectroscopy of G29.96-0.02: The First Spectral Classification of the Ionizing Star of an Ultracompact H II Region. *ApJ*, 490:L165+.

Weintraub, D. A. and Kastner, J. (1993). The exciting young stellar object for the molecular outflow at the core of L1287. *ApJ*, 411:767–772.

Weintraub, D. A., Kastner, J. H., Griffith, L. L., and Campins, H. (1993). Near-infrared, polarimetric imaging of the bipolar lobes of GSS 30 - Protostellar infall and/or outflow? *AJ*, 105:271–283.

Weintraub, D. A., Sandell, G., Huard, T. L., Kastner, J. H., van den Ancker, M. E., and Waters, R. (1999). Submillimeter Imaging of T Tauri's Circumbinary Disk and the Discovery of a Protostar in Hind's Nebula. *ApJ*, 517:819–828.

Whitney, B. A. and Hartmann, L. (1992). Model scattering envelopes of young stellar objects. I - Method and application to circumstellar disks. *ApJ*, 395:529–539.

Whittet, D. C. B., Martin, P. G., Hough, J. H., Rouse, M. F., Bailey, J. A., and Axon, D. J. (1992). Systematic variations in the wavelength dependence of interstellar linear polarization. *ApJ*, 386:562–577.

Wolfire, M. G. and Cassinelli, J. P. (1987). Conditions for the formation of massive stars. *ApJ*, 319:850–867.

Wood, D. O. S. and Churchwell, E. (1989). The morphologies and physical properties of ultracompact H II regions. *ApJS*, 69:831–895.

Yamashita, T., Sato, S., Nagata, T., Suzuki, H., Hough, J. H., McLean, I. S., Garden, R., and Gatley, I. (1987). Polarimetric mapping of a new infrared reflection nebula GGD 27 IRS. *A&A*, 177:258–264.

Yao, Y., Ishii, M., Nagata, T., Nakaya, H., and Sato, S. (2000). Unveiling Deeply Embedded Sources by Near-Infrared Polarimetric Imaging. *ApJ*, 542:392–399.

Yorke, H. W. W. (2003). The Formation of Massive Stars via Accretion. In *IAU Symposium*.

Yu, K., Billawala, Y., Smith, M. D., Bally, J., and Butner, H. M. (2000). A Multiwavelength Study of Outflows in OMC-2/3. *AJ*, 120:1974–2006.

Zijlstra, A. A., Pottasch, S. R., Engels, D., Roelfsema, P. R., Hekkert, P. T., and Umana, G. (1990). Mapping the Outflow of OH:5.89-0.39. *MNRAS*, 246:217.

Zoonematkermani, S., Helfand, D. J., Becker, R. H., White, R. L., and Perley, R. A. (1990). A catalog of small-diameter radio sources in the Galactic plane. *ApJS*, 74:181–224.